MORPHOLOGY AND DYNAMICS OF SPIRAL GALAXIES

by
ANGELOS MISIRIOTIS

THESIS
Submitted in partial fulfillment of the requirements for the degree
of Doctorate in Physics in the Department of Physics
of the University of Crete

August 2001, Heraklion, Crete

Acknowledgements

During the years of my thesis, I had the luck and the pleasure to meet and collaborate with many interesting people. The interaction with them, both on scientific and social subjects is considerable, and I owe them my best acknowledgments.

The greatest thank is owed to Professor Nick Kylafis, University of Crete, Department of Physics, who gave me the opportunity to take active part in the world of science. I would like to thank Nick Kylafis for being an excellent supervisor, for his contribution with unique advises, always available to help me with my concerns. I also want to thank Professor John Papamastorakis and Professor Despina Hatzidimitriou for taking the responsibility of being in the committee for my thesis.

I consider myself very fortunate for having the opportunity to meet Dr. Manolis Xilouris who has been a tutor, a colleague, also a good friend. I thank him for spending his precious time while he was working on his thesis to answer my stupid and trivial questions.

I would like to thank Professor Richard Tuffs and Dr. Cristina Popescu for the excellent collaboration we had and for the warm hospitality and financial support they offered me at the Max Planck Institut für Kernphysik during my visits in Heidelberg, as well as for their tolerance for my numerous mistaken calculations.

I have gained a lot from my stay in the Marseille Observatory while working with Professor Lia Athanssoula who has been a paradigm of a dedicated scientist for me. I thank her for the opportunity she gave me to work with her and for bearing with all my nagging about the difficulties of living in France. I would also like to thank Mr. Jean-Charles Lambert from the Marseille Observatory for being the best system administrator of all times.

I would like to thank Dr. Simon Bianchi with whom cooperation was both pleasant and creative, and although we have never met in person I hope that one day we will meet.

Finally and most importantly I would like to thank my sister, Mrs. Christina Misirioti for her continuous moral support and friendship, and this thesis is dedicated to her.

Angelos Misiriotis

Contents

1 Introduction **6**
- 1.1 About galaxies . . . 6
- 1.2 Dust in galaxies . . . 6
  - 1.2.1 Dust grain models . . . 7
  - 1.2.2 Opacity of spiral galaxies . . . 8
  - 1.2.3 Dust heating and emission in spiral galaxies . . . 10
- 1.3 Dynamics of galaxies . . . 11
  - 1.3.1 The force calculation . . . 12
  - 1.3.2 The initial conditions . . . 12
- 1.4 Morphology of barred galaxies . . . 13
- 1.5 Plan of the thesis . . . 13

2 Is the exponential distribution a good approximation of dusty galactic disks? **18**
- 2.1 Introduction . . . 18
- 2.2 Method . . . 19
  - 2.2.1 Artificial spiral galaxies . . . 19
  - 2.2.2 The fitting procedure . . . 24
- 2.3 Results . . . 25
- 2.4 Summary . . . 27

3 The influence of clumping on surface brightness fits of edge-on spiral galaxies **31**
- 3.1 Introduction . . . 31
- 3.2 Our Method . . . 32
- 3.3 Results of the fits . . . 34
  - 3.3.1 Testing of the codes and the effects of scattering . . . 34
  - 3.3.2 The effect of clumping . . . 35
- 3.4 Summary . . . 36
- 3.5 Appendix. Models with exponentially distributed clumps . . . 40

4 Modelling the spectral energy distribution of galaxies. I. Radiation fields and grain heating in the edge-on spiral NGC891 **42**
- 4.1 Introduction . . . 42
- 4.2 The model . . . 45

4.2.1 The properties of the dust grains . . . 45
4.2.2 Derivation of the diffuse optical and UV radiation field. . . . 46
4.2.3 Calculation of the IR spectrum from grains embedded in the diffuse optical and UV radiation field . . . 52
4.3 Results for the "standard model" . . . 53
4.4 Results for the "standard model" supplemented by localised sources . . . 54
4.5 The missing FIR/sub-mm component of our "standard model" . . . 56
4.5.1 The effect of altering the geometry of the large-scale distribution of stars and dust . . . 56
4.5.2 Extraplanar dust? . . . 56
4.5.3 The case of hidden dust in clumps . . . 57
4.5.4 A two-dust-disk model . . . 58
4.6 The radial profiles . . . 60
4.7 Discussion: the contribution of different stellar populations in heating the dust in NGC891 . . . 61
4.8 Summary and Conclusions . . . 63

5 Modeling the spectral energy distribution of galaxies. II. Disk opacity and star formation in 5 edge-on spirals 70
5.1 Introduction . . . 70
5.2 Model calculations for the five galaxies . . . 73
5.3 Results for the "standard model" . . . 75
5.4 Application of the "two-dust-disk model" to NGC 5907 . . . 76
5.5 Discussion . . . 79
5.6 Summary . . . 82

6 Morphology, photometry and kinematics of N-body bars. I Three models with different halo central contrations 87
6.1 Introduction . . . 87
6.2 Simulations . . . 89
6.3 Two types of N-body bars . . . 92
6.4 The axial ratio and shape of the isodensities in the bar region. Face-on view 95
6.5 Density profiles along the major and minor axes of bars seen face-on . . . 99
6.6 Density profiles of bars seen edge-on . . . 100
6.7 Fourier components of the face-on density distribution . . . 101
6.8 Length of the bar . . . 102
6.9 Quantifying the peanut shape . . . 105
6.10 Rotation . . . 109
6.11 Velocity dispersions of a thin strip of particles taken along the bar major axis . . . 112
6.12 The bulge . . . 113
6.13 Summary and discussion . . . 114
6.14 . . . 118
6.15 . . . 119

7 Summary **120**
7.1 Main results 120
7.1.1 Galaxy models for radiative rransfer 120
7.1.2 Spectral energy distribution of spiral galaxies 120
7.1.3 N-Body simulations of barred galaxies 121
7.2 Future prospects 121
7.2.1 Suggestions for future studies on SED of galaxies 121
7.2.2 Suggestions for future studies on N-body simulations of barred galaxies 121

Chapter 1

Introduction

1.1 About galaxies

Galaxies constitute the building blocks of the universe. There are roughly 10^{11} galaxies in the known universe of all sizes and shapes, ranging from giant ellipticals to dwarf galaxies and from almost perfectly luminous spheres to irregular ensembles of stars rich of gas and dust. Spiral galaxies are the most spectacular kind, their spiral arms inspiring an almost divine charm to all intelligent creatures that wonder about the universe.

Admiration often drives thirst for knowledge and therefore, since the discovery of their existence, galaxies have been the subject of countless studies. This thesis is an insignificant part of an effort, whose final, ambitious goal is nothing less than understanding the universe itself.

Fortunately Nature has been generous in providing a huge sample of galaxies. Classification is always the first step of understanding the properties of a large number of objects. The first classification scheme was introduced by Hubble (1926), before we even realized the true nature of galaxies, and it was based on the general shape of a galaxy, the shape of its spiral arms (if any), the size of its bulge and the existence of a bar. Hubble's classification, although quite modified since its original introduction, is still the prevailing one in modern astronomy.

Since the discovery of the nature of galaxies, our understanding on them has vastly improved. Many basic problems such as the opacity of spiral galaxies, the spiral structure, the origin of bars, the origin of elliptical galaxies and star formation processes have found their solution (though we can be sure that Nature still has many surprises to keep us interested). On the other hand, there are several fundamental unsolved problems that stubbornly resist our efforts, the nature of dark matter probably being the most notorious of them.

1.2 Dust in galaxies

A large part of my thesis is related to the dust found in spiral galaxies. Roughly 0.01% of the galactic mass is dust. While this is a very small percentage of the total galactic mass, the importance of dust in the interstellar medium is large. First of all, the existence of

intelligent life, as we know it, depends largely on dust and though our importance may not be larger than that of the dust we come from, the fact itself is amusing. But the importance of dust in modern astronomy lies mostly on the following facts.

1. Dust plays an important role in star formation, one of the most important processes in the evolution of galaxies, mainly by acting as a cooling agent that allows the condensation of hydrogen clouds to protostars.

2. Dust radiates at wavelengths at which the interstellar medium is almost transparent. With the new generation of far infrared (FIR) instruments, we can probe parts of galaxies that are visually well hidden.

3. Dust absorbs starlight, especially at shorter wavelengths thus obscuring the distribution of stars. Understanding galactic internal extinction is an indispensable step in deriving the intrinsic luminosity of stellar populations and refining our knowledge of the morphology and kinematics of galaxies as well as the evolution of stellar populations.

4. The opacity of spiral galaxies due to dust is of fundamental importance in studies concerning the observations of the distant universe, because if galaxies are opaque then the distant universe is invisible to us.

1.2.1 Dust grain models

Dust grains are believed to be of two kinds: amorphous silicate and carboneous material. They populate the interstellar medium in almost equal amounts and they span a large range of sizes, from molecules consisting of tens of atoms up to particles as large as 0.3μm. The optical properties of dust grains depend both on their size and their composition and the determination of these properties is of fundamental importance in any attempt to understand the role of dust in astronomy.

Before the Infrared Astronomical Satellite (IRAS), dust was solely known by its extinction effects on the light of nearby stars. The extinction properties of dust in the optical bands can be attributed to what is called "large grains", i.e. grains whose size is comparable to the light's wavelength. Several studies have established that these large grains are almost certainly graphites and silicates.

Mathis (1977) established a standard model for the properties of dust based on the interstellar extinction over the wavelength range from 0.1 to 1 micron. Hong & Greenberg (1978) addressed the problem of the size distribution studying the cooling of dust in shock-heated gas. Draine & Lee (1984) calculated theoretically the optical properties of a mixture of large grains of silicates and graphite and found a very good agreement with the observationally determined extinction law. Mathis & Whiffen (1989) expanded these studies to take into account more complicated structures of dust grains. Kim et al. (1994) studied the effect of different size distributions of dust grains.

Under the light of the FIR data obtained by IRAS, it became evident that while large grains of silicates and graphite are quite adequate to explain the extinction curve, several spectral emission features from dust in the region from 1 to 10 microns could not be

explained by the "large grain" model. Current models incorporate Polycyclic Aromatic Hydrocarbon (PAH) molecules to account for this part of the emission spectrum.

Desert et al. (1990) proposed an empirical dust model made of big grains, very small grains, and PAHs and studied the emission of the grains in various interstellar environments. Siebenmorgen & Kruegel (1992) studied the extinction curve and the infrared (IR) spectra of two reflection nebulae, a planetary nebula and an HII region and argued for a three-component model consisting of large silicate and carbon grains, small graphite particles and PAHs. Dwek et al. (1997) used data from the DIRBE instrument of the COBE satellite to obtain a complete wavelength coverage of the dust emission at wavelengths shorter than 60 μm and presented a model including PAHs to fit the data. Li & Greenberg (1997) addressed simultaneously the interstellar extinction and polarization due to dust and included PAH molecules in their model to account or the Far Ultraviolet extinction.

Further complications concerning the emission spectrum of dust rise from transiently heated grains. These are so small grains that the absorption of a single photon can change their temperature significantly enabling them to emit at shorter wavelengths than if they were in thermal equilibrium. This effect is also known as "stochastic heating" and becomes more important when the radiation field that heats the dust is dominated by ultraviolet (UV) photons. Gail & Sedlmayr (1975) developed a method of computing the emission spectrum of such grains. Draine & Anderson (1985) included stochastic heating to study the emission spectra of HI clouds as well as dark clouds. Dwek & Arendt (1992) studied the same effect on dust grains interacting with a hot plasma.

Recent studies (Draine & Li 2001; Li & Draine 2001) attempt to develop a sophisticated, quantitative model for the unified explanation of absorption and emission properties of interstellar dust.

1.2.2 Opacity of spiral galaxies

The amount of internal extinction in spiral galaxies has been a subject of debate for a long time. The first approach to this problem involved statistical studies of many galaxies. The surface brightness of galaxies was found to be independent of inclination and therefore the conclusion was that spiral galaxies are optically thick. Valentjin (1990) studied a sample of 26,000 galaxies and argued that only the outer layer of stars is observable. Choloniewski (1991) introduced several new estimators of inclination dependence and argued about biases in other estimators in the literature. He found that galactic brightnesses are strongly depended on inclination while galactic diameters are not and argued that galaxies are opaque. Cunow (1992) studied a sample of 15,000 faint spiral galaxies and obtained a face-on central optical depth of the order of 7. Giovanelli et al. (1994) analyzed the photometric properties of a sample of Sbc-Sc galaxies and found spiral disks to have central optical depths less than 5 in the I band. Valentjin (1994) presented a refined study focused in the blue band and concluded again that galaxies are in general opaque.

On the other hand, several studies suggested exactly the opposite, namely that spiral galaxies are mostly transparent, save maybe the innermost parts of their disks. Huizinga & van Albada (1992) used data from the surface photometry of Sc galaxies and presented

results that these galaxies are transparent throughout most of their disk except their central region. Byun et al. (1993) studied a sample of 1,355 spiral galaxies and compared them with radiative transfer models concluding that the overall opacity of spiral galaxies appears to be rather moderate at most. Davies et al. (1993) suggested that selection biases can explain the contradictory results of statistical studies. Further support for the low opacity came from studies of overlapping pairs of galaxies suggesting that galaxies exhibit moderate optical depths of the order of one in the optical band (Keel 1983, Andredakis & van der Kruit 1992; White & Keel 1992; Conselice et al. 1995; Domingue et al. 1999; White et al. 2000; Domingue et al. 2000). Observations in combination with models on individual galaxies reached similar conclusions (Bosma et al. 1992; Emsellem 1995) supporting the case for low opacity.

An important step towards understanding the effect of dust on the internal extinction was achieved by the development of a technique applicable to nearby edge-on galaxies. This technique, which was introduced by Kylafis & Bahcall (1987) and subsequently used in many studies, consists of fitting a radiative transfer model image of the galaxy on observations at different wavelengths. The result of this technique is the exact determination of the spatial distribution of the intrinsic stellar population, the spatial distribution of the dust and the extinction coefficient at different wavelengths. Since the determination of the dust extinction coefficient can be done independently for many wavelengths, the comparison of the results with the known extinction law gives us confidence for the reliability of the model. The agreement of the derived extinction curve with the extinction curve found observationally indicates that the method is indeed accurate. Xilouris et. al (1997) conducted a detailed study of the edge-on spiral UGC 2048 and suggested that if it were to be seen face-on it would be completely transparent. This result was verified for other galaxies. Xilouris et al. (1998) applied the method to NGC 891 using observations of 5 optical and NIR bands (B,V,I,J,K) and found that the central face-on optical depth in the V band is of the order of 1. Kuchinski et al. (1998) compared a sample of 15 highly inclined spiral galaxies with radiative transfer models and concluded that the central face-on optical depth in the V band is between 0.5 and 2. Xilouris et al. (1999) studied 5 more edge-on spiral galaxies and derived an average face-on optical depth in the V band equal to 0.5. These studies conclude that galaxies are optically thin, their central face-on optical depth being around unity in the optical bands.

While it is now established that the central face-on optical depth of spiral galaxies is of the order of unity, there are some issues to be clarified. In the studies mentioned above, the assumed model of spiral galaxies is axisymmetric and the dust is smoothly distributed in an exponential disk. Real galaxies on the other hand exhibit prominent spiral structures and/or bars that are far from axisymmetric. Furthermore, the dust in real galaxies is not smoothly distributed but it is (at least partly) distributed in clumps. In this thesis I will quantify the error made by the axisymmetric simplification as well as the error due to the assumption that the dust is smoothly distributed. It will be shown that neglecting the spiral structure when modeling spiral galaxies does not introduce a significant error in the parameters used to describe a spiral galaxy. On the other hand neglecting the effect of clumpiness can lead to an underestimation of the dust mass of the order of 40%.

1.2.3 Dust heating and emission in spiral galaxies

Dust absorbs starlight very efficiently. The absorbed energy is reprocessed to FIR radiation and the exact shape of the emission spectrum depends on both the input radiation field and the dust composition. A complete description of a spiral galaxy in terms of optical processes should be able to reproduce the appearance of the galaxy at all the available wavelengths.

Until IRAS, little was know about dust emission. Yet, even when the vast number of observations from IRAS became available the amount of dust was still a subject of debate. IRAS was able to observe at 60 and 100 microns and thus the observations were limited to dust whose temperature is around 30 K. With the data from IRAS as well as from IRAM, SCUBA and ISO covering a wavelength range from tens of microns to a millimeter the complete Spectral Energy Distribution (SED) of galaxies was available and it became clear what was already assumed. Namely that 90% of the dust mass is cold, its temperature being around 10 K and therefore the dust masses calculated from the IRAS fluxes were underestimated by a factor of about 10.

With the availability of the complete emission spectrum of galactic dust, the application of energy balance methods have appeared. These methods rely on the fact that whatever energy is absorbed by the dust, has to be reemitted in the FIR. Energy balance methods constrain in a simple way the amount of dust in a galaxy. In the simplest form of these methods the shape of the spectrum is not considered. Xu & Buat (1995) used UV, optical and FIR observations for a sample of 135 spiral galaxies and applied a simplified radiative transfer model to conclude that the mean B-band face-on optical depth of the galaxies analyzed is equal to 0.5. Buat & Xu (1996) expanded their study to investigate the correlation between star formation and dust extinction and found that the extinction for Sa to Scd galaxies at 2000 Å is around 0.9 magnitude. Energy balance methods applied on starburst galaxies have helped in establishing a correlation between star formation and FIR luminosity. Rowan-Robinson & Crawford (1989) modeled the fluxes of the four IRAS bands in a number of galaxies using a cool-disk component, a warm-starburst component and a Seyfert component. Rowan-Robinson & Efstathiou (1993) focused on starburst galaxies and showed that the optical depth of such objects in the V band is of the order of 40 and therefore almost all their intrinsic luminosity is reprocessed to FIR. Krugel & Siebenmorgen (1994) modeled the dusty hot spots in the starburst galaxy M82 using a radiative transfer code and a sophisticated dust model including PAHs. Gordon et al. (1997) investigated the nature of dust in 30 starburst galaxies using a SED model to discover a trend in dust properties with star-formation intensity. Efstathiou et al. (2000) presented a sophisticated radiative transfer model taking into account the evolution of star-forming giant molecular clouds and indicated that FIR surveys constitute a very good indicator for starbursts.

It is the case that active galaxies emit most of their intrinsic starlight in the UV region due to the high star-formation rate (SFR). Star-forming regions are rich in dust and therefore almost completely opaque, resulting in a total transformation of UV to FIR, rendering the last a quite reliable tracer for the SFR.

In normal spiral galaxies however the situation is much more complicated. First of all, a large part of the dust heating is attributed to the old stellar population. Furthermore,

the relatively small optical thickness of spiral galaxies increases the importance of the relative spatial distribution of dust and stars. The transformation efficiency of optical and UV starlight to FIR depends on many factors and a direct interpretation of FIR to SFR becomes problematic. To compound, the dust temperature in normal spirals is lower than in starbursts and the FIR emission spectrum peaks at longer wavelengths than the IRAS bands. Only recently, observations from SCUBA (e.g. Alton et al. 1998; Israel et al. 1999; Dunne 2000; Bianchi et el. 2000) and ISO (e.g. Haas et al. 1998; Stickel et al. 2000) have revealed the actual shape of the emission spectrum in normal spirals and made it possible to constrain SED models. Silva et al. (1998) studied a sample of normal and starburst galaxies using a spherically symmetric model consisting of diffuse dust as well as dusty star forming regions. Devrient et al. (1999) developed a model for the SED of galaxies from far-UV to radio wavelengths. They argued that their model can be applied on a wide variety of galactic objects. Bianchi et al. (2000) presented simulations of FIR emission using a Monte Carlo radiative transfer code and a simple model for the dust emission and applied it to the face-on spiral galaxy NGC 6946 arguing that the dust amount implies a face-on optical depth of the order of 5.

In this thesis I present a method for the modeling of the SED of spiral galaxies. I have applied it to five edge-on spirals for which the dust and the stellar content are already known from the studies of Xilouris et al. (1997; 1998; 1999). The fact that the galaxies of this study are edge-on and their dust lane is prominently visible, allows a very accurate determination of their dust content. On the other hand, the very same orientation hides all information about star formation which takes place in the galactic plane. Through this study, the models for these galaxies will be refined and new information about the star formation rate and the origin of the dust heating will be presented. Evidence is presented that in the studies by Xilouris et al. (1997; 1998; 1999) a percentage of the dust mass has passed undetected.

1.3 Dynamics of galaxies

The ultimate goal of the investigation of the morphology of galaxies is the understanding of their birth and evolution. While morphological studies provide the ground for evolution theories, the final confirmation of such theories relies on a "working model". We are still far away from such a model. Numerical simulations (also known as N-body simulations) will be the base for such models. Through numerical simulations, several riddles of the morphology of galaxies have been solved. A part of this thesis deals with some of the still unsolved riddles.

A whole book would be hardly enough for a complete introduction on the subject of galactic dynamics. Here I will present only some representative highlights, which I found important while working on N-body simulations, the most straight-forward approach in understanding the dynamical processes of spiral galaxies.

N-body simulations consist of solving the equations of motion for a large number of particles given a set of initial conditions and provide a direct way to test ideas concerning the origin and evolution of the morphological characteristics of galaxies. While the concept of N-body simulations is very simple, they exhibit two difficulties. One of them is of

technical nature and the other of physical nature. Both are explained below.

1.3.1 The force calculation

The technical difficulty of N-body simulations is the calculation of the accelerations of the particles. The acceleration of each particle depends on its relative position to all the other particles. The time spent for this calculation is proportional to the square of the number of particles involved in the calculation.

Fortunately, Barnes & Hut (1986) introduced a method called "Tree Code" that eliminates this problem at the cost of algorithmic complexity and reduced accuracy. The basic idea behind the Tree Code lies in dividing the particles in groups according to their relative position and then approximate these groups by their center of mass when the desired position for calculating the force field lies far away from the group. This approach allows the use of many more particles for the same amount of computation time.

A different approach, introduced by Sugimoto et al. (1990), involves the construction of specialized hardware dedicated to the force calculation. A special computer card is attached to the front-end computer and while the front-end computer takes care of the integration of the equations of motion, the special computer card calculates the forces much faster than it would be possible in the front-end computer.

The combination of the two methods, i.e. a Tree Code that uses special hardware to calculate the forces between particles, was introduced by Fukushige (1991) and has proved so far to be one of the most powerful configurations to address the technical difficulties of N-body simulations.

Since then, both hardware and software have improved very rapidly leading to systems that can calculate the force of 4 million particles within a few seconds (Ebisuzaki et al. 1993; Okumura et al. 1993; Athanassoula et al. 1998; Kawai et al. 2000). The N-body simulations presented in this thesis, consist of 1 million particles and their equations of motion are followed for 57600 timesteps, roughly equivalent to 10^{10} years.

1.3.2 The initial conditions

The second difficulty concerning N-body simulations is of physical nature and consists of the simple fact that we do not know the initial conditions describing the early stages of a spiral galaxy. For this work we will assume that the initial state of a galaxy can be described by the superposition of three components (Hernquist 1993).

- A disk-like distribution of particles with near-circular orbits representing the stars that have been born by the collapsed gaseous material.
- A dense spherical distribution of particles in the center of the galaxy representing the bulge.
- An extended spherical distribution of particles representing the halo of the galaxy.

Observations of galaxies can provide some hints for the distributions of the disk and the bulge, but in the case of the halo all the information is indirect and comes from the

gravitational effect of the dark haloes on the luminous matter of the galactic disks. The contribution of the dark mater to the gravitational field in the inner parts of the galaxy is still a subject of debate.

1.4 Morphology of barred galaxies

Half of the spiral galaxies are barred, i.e., they exhibit an elongated concentration of mass in their inner part. Many bars when seen edge-on exhibit a peanut or boxy shape caused by the shape of the orbits in the bar potential. A bar can be created spontaneously (though this is not the only way) from an axisymmetric disk and it is the result of what is called (not surprisingly) bar instability. The bar instability has been studied analytically in relation to the amplification of the density waves that cause the spiral structure (Toomre 1977), as well as numerically with the use of N-body simulations (Sellwood 1981, Athanassoula & Sellwood 1986). Barred galaxies have been studied from the observational point of view, aiming at determining the morphological properties, and from the theoretical point of view, aiming at understanding the bar formation processes. In this thesis I present a study of theoretical (numerical) barred galaxies from the observational point of view. Several morphological characteristics of different N-body simulations of galaxies will be quantified with the hope that this analysis will be useful for future observations and will provide a common basis for the comparison of real and simulated barred galaxies.

It is shown that while in a model with a high central halo concentration the bar formation takes longer, when the bar is eventually formed, it is much more massive, elongated and peanut-like than in a model where the halo is not centrally concentrated. The kinematic properties of the particles are also studied.

1.5 Plan of the thesis

In the first chapter, I investigate the effect of the spiral structure on the edge-on appearance of spiral galaxies. The validity of the axisymmetric model is examined and I confirm that it is quite adequate for the description of spiral galaxies.

In the second chapter the effect of dust clumpiness on the edge-on appearance of spiral galaxies is quantified. When a given amount of dust is distributed in clumps the galactic opacity is decreased as compared to a smooth distribution. I quantify the amount of dust mass that passes undetected because it is hidden in clumps and found it to be no more than 40% of the total amount of dust of a spiral galaxy.

In the third chapter, I introduce a sophisticated model for the description of dust absorption and emission in spiral galaxies. The model is applied successfully to the edge-on spiral NGC 891 explaining both the volume integrated SED and the radial profiles available from observations.

In the forth chapter the SED model is applied to four other edge-on galaxies. The derived SFR is compared with that available in the literature for face-on galaxies and excellent agreement is demonstrated. A case is made for large amounts of "hidden dust" that may not contribute to the galaxian opacity in the visual bands.

In the fifth chapter the morphology of barred galaxies is studied using N-body simulations of barred galaxies. In this chapter an attempt to establish a link between the morphological characteristics of N-body models and real barred galaxies is presented.

Bibliography

Alton P. B., Bianchi S., Rand R. J., Xilouris E. M., Davies J. I., Trewhella M., 1998, ApJ, 507, L125

Andredakis Y. C., van der Kruit P. C., 1992, A&A, 265, 396

Athanassoula L., Bosma A., Lambert J-C., Makino J., 1998, MNRAS, 293, 369

Athanassoula L., Sellwood J. A., 1986, MNRAS, 221, 213

Barnes J., Hut P., 1986, Nat, 324, 446

Bianchi S., Davies J. I., Alton P. B., Gerin M., Casoli F., 2000, A&A, 353, L13

Bianchi S., Davies J. I., Alton P. B., 2000 A&A, 359, 65

Bosma A., Byun Y., Freeman K. C., Athanassoula E., 1992, Apj, 400, L21

Buat V., Xu C., 1996, A&A, 306, 61

Byun Y. I., Freeman K. C., Mathewson D. S., 1993, AAS 182, 17

Choloniewwski J., 1991, MNRAS, 250, 486

Conselice C. J., Keel W. C., White R. E. III, 1995, AAS, 187, 4806

Cunow B., 1992, MNRAS, 251, 251

Davies J. I., Phillips S., Boyce P. J., Disney M. J., 1993, MNRAS, 260, 491

Desert F.-X., Boulanger F., Puget J. L., 1990, A&A, 237, 215

Devriendt J. E. G., Guiderdoni B., Sadat R., 1999, A&A, 350, 381

Domingue D. L., Keel, W. C., White R. E. III, 2000, ApJ, 545, 171

Domingue D. L., Keel, W. C., Ryder S. T., White R. E. III, 1999, AJ, 118, 1542

Draine B. T., Anderson N., 1985, ApJ, 292, 494

Draine B. T., 1981, ApJ, 245, 880

Draine B. T., Lee H. M., 1984, ApJ, 285, 89

Drain B., Li A., 2001, ApJ 554,778

Dunne L., Eales S., Edmunds M., Ivison R., Alexander P., Clements D. L., 2000, MNRAS, 315, 115

Dwek E., Arendt R. G., Fixsen, D. J., et al., 1997 ,ApJ, 475 ,565

Dwek E., Arendt R. G., 1992, ARA&A 30,11

Ebisuzaki T., Fukushige T., Funato Y., et al., 1993, AAS, 182, 1305

Efstathiou A., Rowan-Robinson M., Siebenmorgen R., 2000, MNRAS, 313, 734

Emsellem E., 1995, A&A, 303, 673

Fukushige T., Ito T., Makino J., Ebisuzaki T., Sugimoto D., Umemura M., 1991, PASJ, 43, 841

Gail H.-P., Sedlmayr E., 1975, A&A, 43, 17

Giovanelli R., Haynes M. P., Salzer J. J., et al., 1994, AJ, 107, 2036

Gordon K. D., Calzetti D., Witt A. N., 1997, ApJ, 487, 625

Haas M., Lemke D., Stickel M., et al., 1998, A&A, 338, L33

Hernquist L., 1993, ApJS, 86, 389

Hong S. S., Greenberg J. M., 1978, A&A, 70, 695

Huizinga J. E., van Albada T. S., 1992, MNRAS, 254, 677

Hubble E., 1926, ApJ, 64, 321

Israel F. P., van der Werf P. P., Tilanus R. P. J., 1999, A&A, 344, L83

Kawai A., Fukushige T., Makino J., Taiji M., 2000, PASJ, 52, 659

Keel W. C., 1983, AJ, 88, 1579

Krugel E., Siebenmorgen R., 1994, A&A, 282, 407

Kuchinski L. E., Terndrup D. M., Gordon K. D., Witt A.N., 1998, AJ, 115, 1438

Kylafis N. D., Bahcall J. N., 1987, ApJ, 317, 637

Kim S., Martin P. G., Hendry P. D., 1994, ApJ, 422, 164

Li A., Greenberg J. M., 1997, A&A, 323, 566

Li A., Drain B., 2001, ApJ, 551, 807

Mathis J., Rumpl W., Nordsieck K. H., 1977 ApJ, 217, 425

Mathis J., 1990, Ann. Rev. Astr. Astrophys., 28,37

Mathis J., Whiffen G., 1989 ApJ 341, 808

Okumura S. K., Makino J., Ebisuzaki T., et al. 1993, PASJ, 45, 329

Silva L., Granato G. L., Bressan A., Danese L., 1998, ApJ, 509, 103

Stickel M., Lemke D., Klaas U., et al., 2000, A&A, 359, 865

Rowan-Robinson M., Crawford J., 1989, MNRAS, 238, 523

Rowan-Robinson M., Efstathiou A., 1993, MNRAS, 263, 675

Sellwood, J. A., 1981, A&A, 99, 362

Siebenmorgen R., Kruegel E., 1992, A&A, 259, 614

Sugimoto D., Chikada Y., Makino J. Ito T., Ebisuzaki T., Umemura M., 1990, Nat, 345, 33

Toomre A., 1977, ARA&A,15,437

Valentijn E. A., 1990, Nat, 346, 153

Valentijn E. A., 1994, MNRAS, 266, 614

White R. E., Keel W. C., 1992, Nat, 359, 129

White R. E. III, Keel W. C., Conselice C, J., 2000, ApJ, 542, 761

Xilouris E. M., Kylafis N. D., Papamastorakis J., Paleologou E. V., Haerendel G., 1997, A&A, 325, 135

Xilouris E. M., Alton P. B., Davies J. I., Kylafis N. D., Papamastorakis J., Trewhella, M., 1998, A&A, 331, 894

Xilouris E. M.,Byun Y. I., Kylafis N. D., Paleologou E. V., Papamastorakis J., 1999, A&A, 344, 868

Xu C., Buat V, 1995, A&A, 293, L65

Chapter 2

Is the exponential distribution a good approximation of dusty galactic disks?

We investigate how significant the spiral structure is on calculations concerning radiative transfer in dusty spiral galaxies seen edge-on. The widely adopted exponential disk model (i.e. both the stars and the dust are distributed exponentially in the radial direction and also perpendicular to the plane of the disk) is now subject to a detailed comparison with a realistic model that includes spiral structure for the stars and the dust in the disk. In particular, model images of galaxies with logarithmic spiral arms are constructed, such that the azimuthally averaged disk is exponential in radius and in height, as the observations suggest. Then, pure exponential disk models (i.e. with no spiral structure) are used to fit the edge-on appearance of the model images. As a result, the parameters derived after the fit are compared to the real values used to create the spiral-structured images. It turns out that the plain exponential disk model is able to give a very good description of the galactic disk with its parameters varying only by a few percent from their true values.

2.1 Introduction

Modeling the dust and stellar content of spiral galaxies is a very crucial procedure needed for the correct interpretation of the observations. The amount of interstellar dust embedded inside spiral galaxies, the way that dust is distributed within spiral galaxies and also the extinction effects of the dust to the starlight are some of the questions that can be answered by performing radiative transfer modeling of individual spiral galaxies.

One very important thing that needs consideration when doing such analysis is the right choice of the stellar and dust distributions. In particular, the galactic disk is a quite complex system, where stars and dust are mixed together usually in a spiral formation. For this reason, one has to use realistic distributions able to reproduce quite accurately the observations. On the other hand, simple mathematical expressions for these distributions are chosen in order to keep the free parameters to the minimum.

For the distribution of the starlight in the disk of spiral galaxies, the exponential function is very widely in use. This simple mathematical expression is able to describe the distribution of stars in both directions, radially and perpendicular to the disk. Decomposition techniques used by different authors in order to separate the bulge and the disk component strongly support this argument. For galaxies seen face-on (and at moderate inclination angles), radial profile fitting (e.g. Freeman 1970), fitting to azimuthally averaged profiles (e.g. Boroson 1981), as well as ellipse fitting techniques to 2D images (e.g. de Jong 1995) show that the exponential in the radial distance R is a good representation of galactic disks with only small deviations mainly due to the spiral structure of the galaxy (see Serna 1997). Other works like those of Shaw & Gilmore (1989) and de Grijs (1997) dealing with modeling of edge-on galaxies support the idea that exponential functions are good representations also for the z (vertical to the disk) direction.

Performing radiative transfer modeling of edge-on galaxies, Xilouris et al. (1997, 1998, 1999) found that exponential functions for the luminosity density of the stars in the disk as well as for the extinction coefficient give an excellent description of the observations. The advantage of modeling galaxies in the edge-on configuration is that the integration of light along the line of sight is able to cancel out most of the structure of the galaxies (i.e. spiral structure) and therfore allows for simple functions such as exponentials to give good representation of the observations. Thus, although in the face-on configuration a large variation between arm and interarm regions might be present for both the stars and the dust (White & Keel 1992, Corradi et al. 1996, Beckman et al. 1996, Gonzalez et al. 1998), in the edge-on case an average description of the galaxy characteristics can be obtained quite accurately. We are going to investigate the validity of this argument by comparing the exponential distributions with more realistic distributions which include spiral structure.

In Sect. 2 we describe the method that we use to address this problem and in Sect. 3 we present the results of our calculations. Finally, in Sect. 4 we summarize our work.

2.2 Method

The method that we follow in this work consists of two basic steps. In the first step, model galaxies with realistic spiral structure are constructed. After a visual inspection of the face-on appearance of these models to see the spiral pattern, we create their edge-on images which are now treated as real observations. In the second step we fit these "observations" with a galaxy model where now the galactic disk is described by the widely used plain exponential model. In this way, a comparison between the parameters derived from the fitting procedure and those used to produce the artificial "observations" can be made and thus a quantitative answer about the validity of the plain exponential model as an approximation to galactic disks can be given.

2.2.1 Artificial spiral galaxies

We adopt a simple, yet realistic, distribution of stars and dust in the artificial galaxy. A simple expression is needed in order to keep the number of free parameters as small

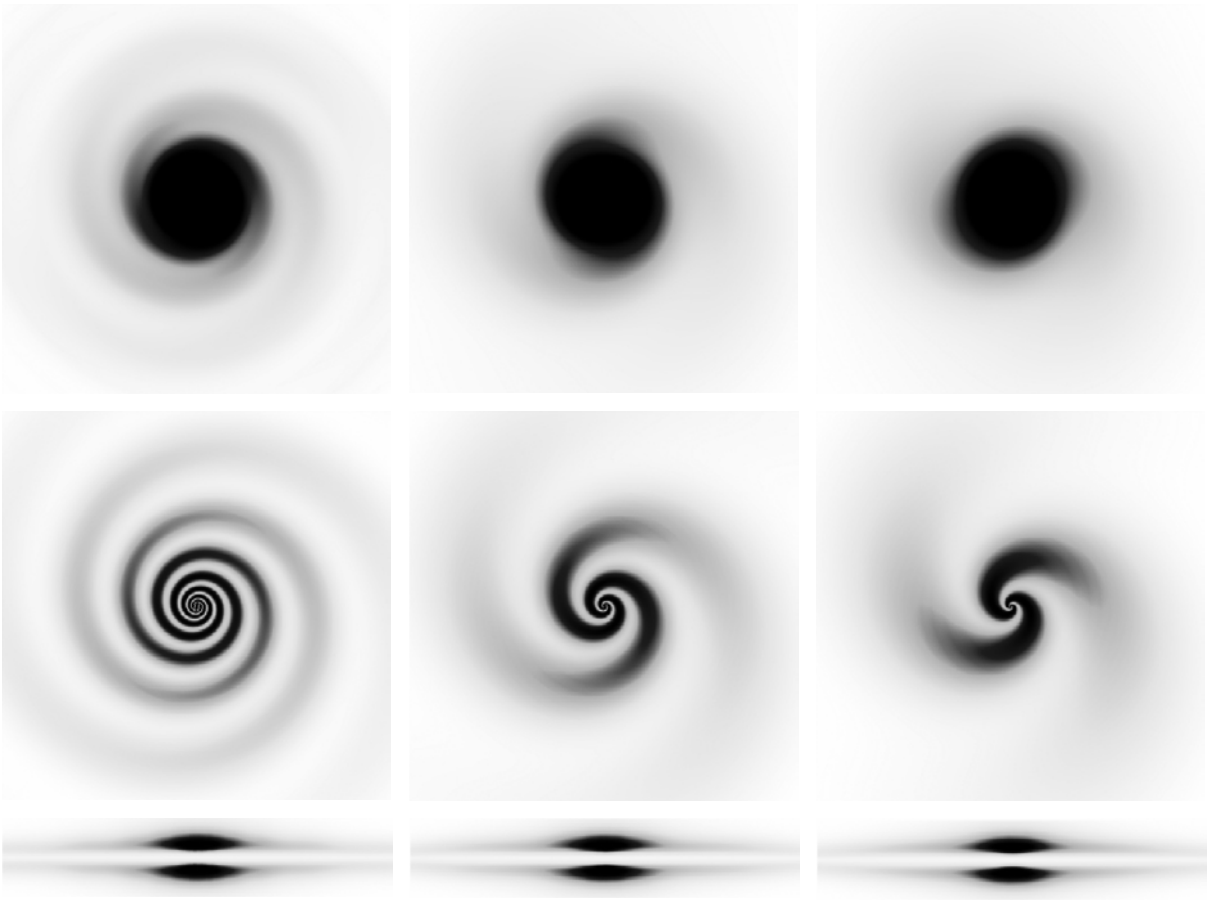

Figure 2.1: Face-on surface brightness of model galaxies (top panel) with different values of the pitch angle ($10°, 20°$ and $30°$ from left to right). The distribution of the face-on optical depth for these galaxies is shown in the middle, while their edge-on appearance (looking from $\phi = 0°$) is shown in the bottom panel.

as possible and thus have a better control on the problem. A realistic spiral structure is that of logarithmic spiral arms (Binney & Merrifield 1998). Thus, a simple but realistic artificial spiral galaxy is constructed by imposing the logarithmic spiral arms as a perturbation on an exponential disk. In this way, the azimuthally averaged face-on profile of the artificial galaxy has an exponential radial distribution.

For the stellar emissivity we use the formula

$$\begin{aligned} L(R,z) = L_s \exp\left(-\frac{R}{h_s} - \frac{|z|}{z_s}\right) \\ \times \left\{1 + w_s \sin\left[\frac{m}{\tan(p)}\log(R) - m\phi\right]\right\} \\ + L_b \exp(-7.67B^{1/4})B^{-7/8} \ . \end{aligned} \tag{2.1}$$

In this expression the first part describes an exponential disk, the second part gives the spiral perturbation and the third part describes the bulge, which in projection is the well-known $R^{1/4}$-law (Christensen 1990). Here R, z and ϕ are the cylindrical coordinates, L_s

Table 2.1: Parameters used to describe a typical spiral galaxy.

Parameter	Units	B band
I_s	mag/arcsec^2	20.0
z_s	kpc	0.4
h_s	kpc	5.0
I_b	mag/arcsec^2	12.0
R_e	kpc	1.5
b/a	–	0.5
τ_λ^e	–	27
z_d	kpc	0.2
h_d	kpc	6.3
w_d	–	0.4
w_s	–	0.3
m	–	2
p	degrees	$10, 20, 30$

is the stellar emissivity per unit volume at the center of the disk and h_s and z_s are the scalelength and scaleheight respectively of the stars in the disk.

The amplitude of the spiral perturbation is described by the parameter w_s. When $w_s = 0$ the plain exponential disk is obtained, while the spiral perturbation becomes higher with larger values of w_s. Another parameter that defines the shape of the spiral arms is the pitch angle p. Small values of p mean that the spiral arms are tightly wound, while larger values produce a looser spiral structure. The integer m gives the number of the spiral arms.

For the bulge, L_b is the stellar emissivity per unit volume at the center, while B is defined by

$$B = \frac{\sqrt{R^2 + z^2(a/b)^2}}{R_e}, \tag{2.2}$$

with R_e being the effective radius of the bulge and a and b being the semi-major and semi-minor axis respectively of the bulge.

For the dust distribution we use a similar formula as that adopted for the stellar distribution in the disk, namely

$$\kappa(R,z) = \kappa_\lambda \exp\left(-\frac{R}{h_d} - \frac{|z|}{z_d}\right)$$
$$\times \left\{1 + w_d \sin\left[\frac{m}{\tan(p)}\log(R) - m\phi\right]\right\}, \tag{2.3}$$

where κ_λ is the extinction coefficient at wavelength λ at the center of the disk and h_d and z_d are the scalelength and scaleheight respectively of the dust. Here w_d gives the amplitude of the spiral perturbation of the dust. Note that the angle ϕ here need not be the same as that in Eq. (1). The stellar arm and the dust arm may have a phase difference between them.

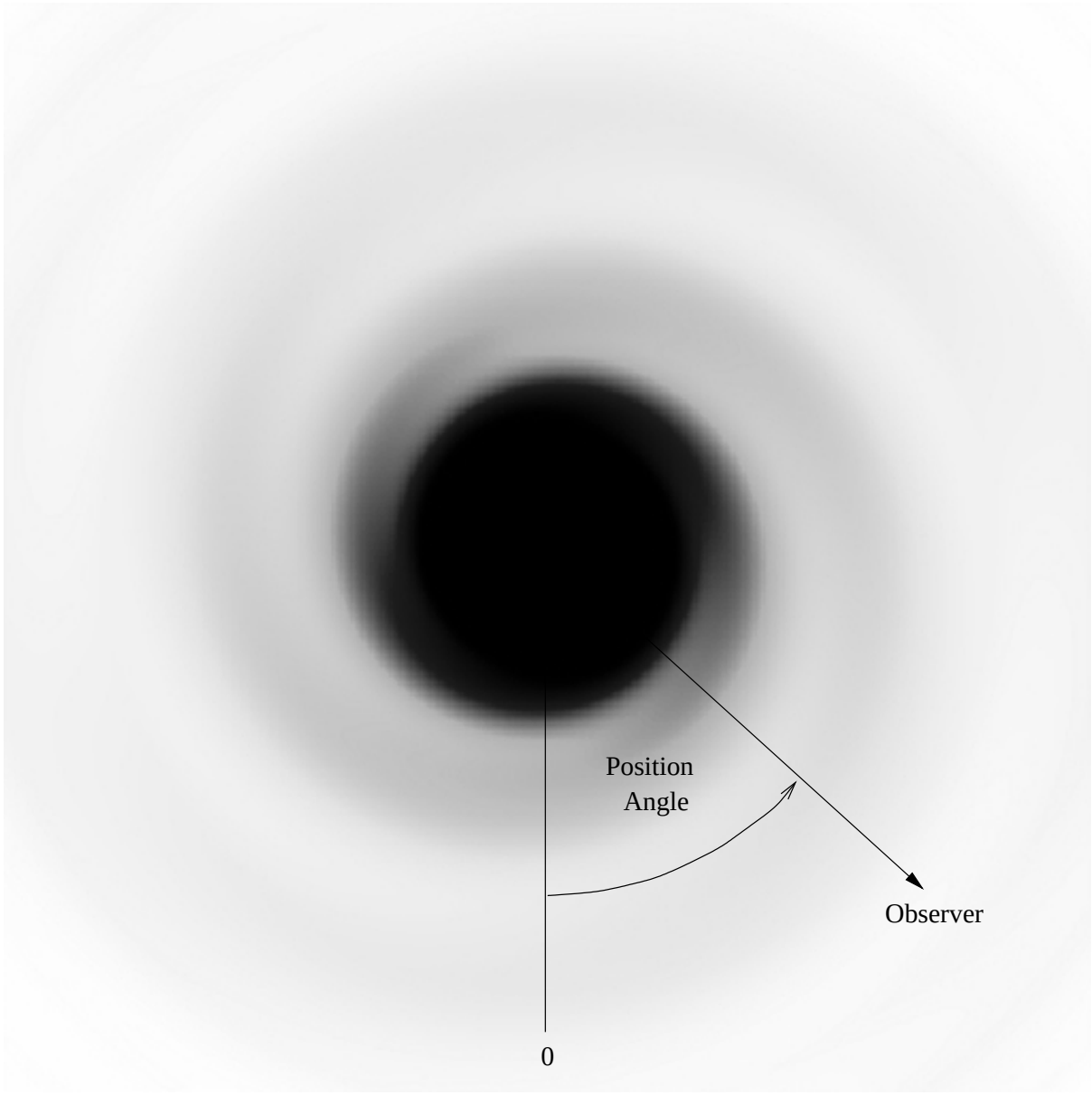

Figure 2.2: Schematic representation of the position angle. The value of 0° is as shown in the figure, while the position angle increases when the line of sight moves counterclockwise.

For the parameters describing the exponential disk of the stars and the dust as well as the bulge characteristics we use the mean values derived from the B-band modeling of seven spiral galaxies presented in Xilouris et al. (1999).

Since the most dominant spiral structure in galaxies is that of the two spiral arms (Kennicutt 1981; Considere & Athanassoula 1988; Puerari & Dottori 1992) we only consider models where $m = 2$. Galaxies with strong one-arm structure do exist, but they constitute a minority (Rudnick & Rix 1998).

For the parameter w_d we take the value of 0.4. With this value the optical depth calculated in the arm region is roughly twice as much as in the inter-arm region. This is

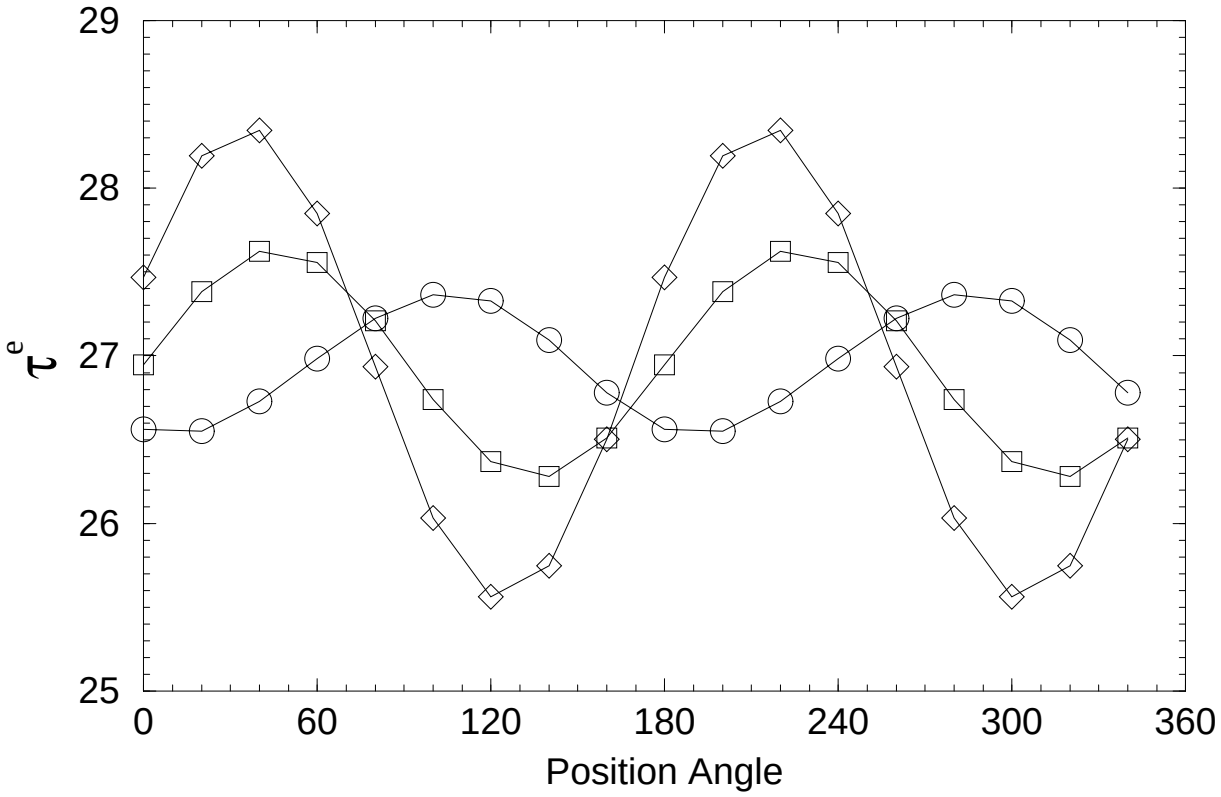

Figure 2.3: The central edge-on optical depth of the model spiral galaxy as a function of position angle. Circles, squares and diamonds refer to three different models with pitch angle 10°, 20° and 30° respectively.

in good agreement with studies of overlapping galaxies (e.g. White & Keel 1992).

For w_s we use the value of 0.3 resulting (with the extinction effects included) in a spiral arm amplitude of $\sim 0.1 - 0.2$ mag, which is a typical amplitude seen in radial profiles of face-on spiral galaxies and reproduces the desired strength for the spiral arms (Rix & Zaritsky 1995).

For the pitch angle p we consider the cases of $10°, 20°$ and $30°$, which give a wide variety of spiral patterns from tightly wound to loosely wound. All the parameters mentioned above are summarized in Table 1.

The radiative transfer is done in the way described by Kylafis & Bahcall (1987; see also Xilouris et al. 1997). As described in detail in these references, the radiative transfer code is capable of dealing with both absorption and scattering of light by the interstellar dust and also of allowing for various distributions for the stars and the dust.

Using the model described above and the parameters given in Table 1 we produce the images shown in Fig. 1. The top three panels of this figure show the face-on surface brightness distribution of such a galaxy for the three values of the pitch angle ($10°, 20°$ and $30°$) from left to right. The spiral structure is evident in these images with the spiral arms being more tightly wound for $p = 10°$ and looser when $p = 30°$.

In the middle three panels of Fig. 1 we show the distribution of the optical depth

when the galaxy is seen face-on for the three different values of the pitch angle mentioned above. In these pictures one can follow the spiral pattern all the way to the center of the galaxy since the bulge is assumed to contain no dust.

Finally, in the last three panels of Fig. 1 one can see the corresponding edge-on appearance of the galaxies shown face-on in the top three panels.

One thing that is very obvious from Fig. 1 (top and middle panels) is that the galaxy is no more axisymmetric as it is the case in the plain exponential disk model. The spiral structure that is now embedded in the model as a perturbation in the disk has broken this symmetry. Thus, in order to do a full analysis of the problem we have to examine the galaxy from different azimuthal views (position angles). To do so we have created nine edge-on model galaxies (for each of the three different pitch angles considered here), covering the range from 0° to 160° with a step of 20° for the position angle. For the definition of the position angle, see Fig. 2. Since the galaxy has exactly the same appearance in the interval from 180° to 360°, we only consider the range of position angles mentioned above.

To demonstrate this asymmetry more quantitatively we have computed the central edge-on optical depth (τ^e) for all these nine model galaxies. Unlike the plain exponential disk model where τ^e can be calculated analytically ($\tau^e = 2\kappa_\lambda h_d$), here we have to perform numerical integration of Eq. (3) along the line of sight that passes through the center. The value of τ^e is shown in Fig. 3 as a function of the position angle. In order to have the full coverage in position angle (from 0° to 360°), the values calculated in the interval (0° - 180°) were repeated in the interval (180° - 360°). In this figure, the three models constructed with pitch angles $10^\circ, 20^\circ$ and 30° are denoted with circles, squares and diamonds respectively. In all three cases, a variation of the optical depth with position angle is evident. The largest variation is found for the case where the pitch angle is 30° and it is $\sim 5\%$. It is obvious that all the values are around the true value of 27, used to construct the galaxy (see Table 1).

2.2.2 The fitting procedure

The edge-on images created as described earlier are now treated as "observations" and with a fitting procedure we seek for the values of the parameters of the plain exponential disk that gives the best possible representation of the "observations". The fitting algorithm is a modification of the Levenberg-Marquardt routine taken from the Minipack library. The whole procedure is described in detail in Xilouris et al. (1997).

Preliminary tests have shown that the derived values of the parameters describing the bulge are essentially identical to the real values used to construct the model images. In order to simplify the fitting process and since we are only interested in the disk, the bulge parameters were kept constant during the fit. Six parameters are now free to vary. These are the scalelength and scaleheight of the stellar disk with its central surface brightness (h_s, z_s and I_s respectively) as well as the scalelength and scaleheight of the dust and the central edge-on optical depth (h_d, z_d and τ^e respectively).

2.3 Results

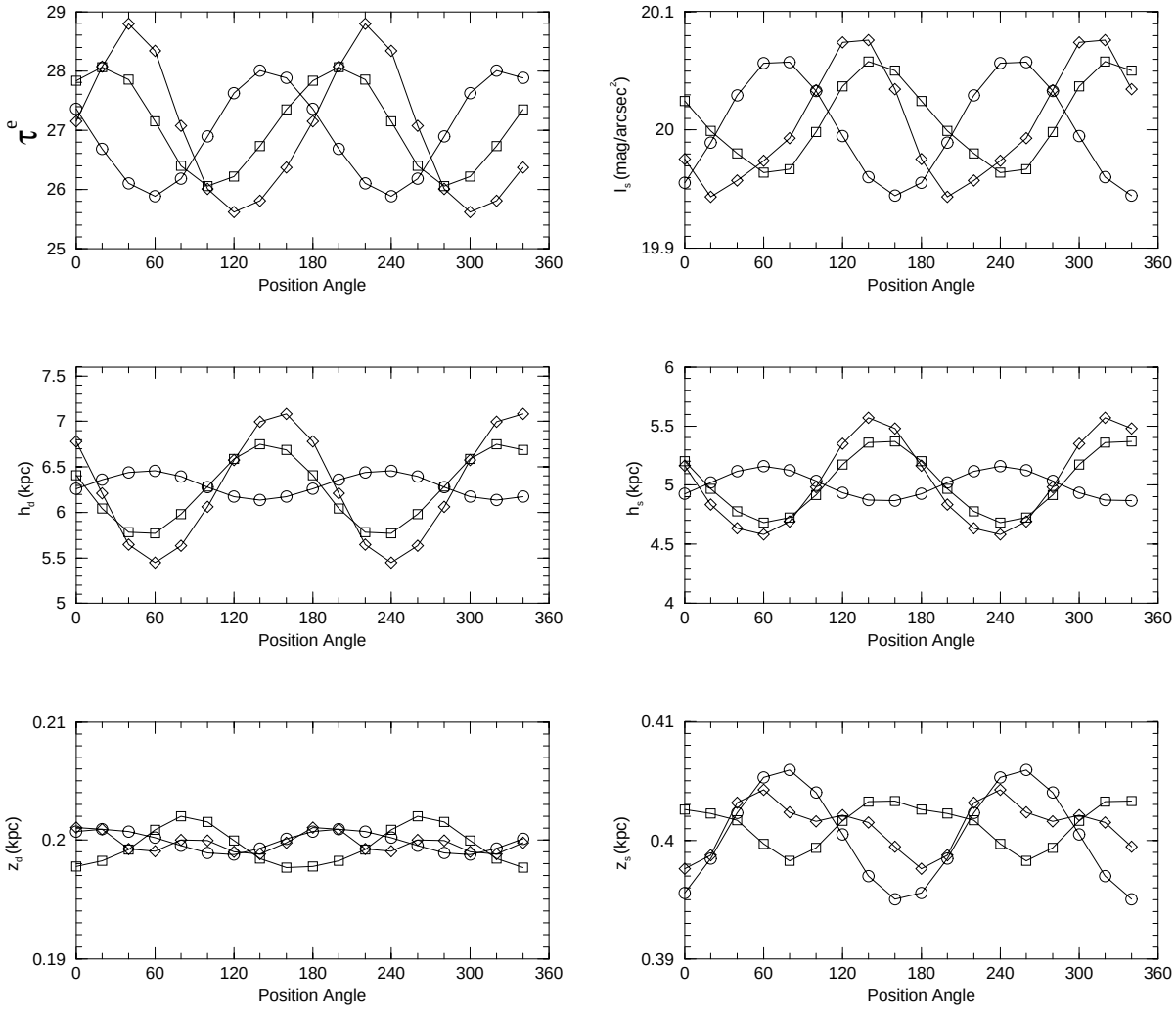

Figure 2.4: Disk parameters deduced by fitting the exponential model to the images of our artificial galaxy for several position angles around the galaxy. In all these sets of images the dust is in phase with the stars. Circles, squares and diamonds refer to three different models with pitch angle 10°, 20° and 30° respectively. The top left graph shows the variation of the deduced optical depth. The top right graph shows the variation of the inferred central intensity of the disk. The middle left graph shows the variation of the derived dust scalelength, while the middle right graph shows that of the stellar scalelength. Finally, the bottom left graph shows the variation of the scaleheight of the dust and the bottom right graph the variation of the scaleheight of the stars.

Figure 4 shows six graphs. The top left graph gives the variation of the deduced edge-on optical depth of the galaxy as we observe it from different angles. From this graph one can see that the variation of the deduced optical depth from different points of view is no more than 6% different than the mean value of the optical depth. Furthermore, a comparison with Fig. 3, which shows the real value of the optical depth, reveals that

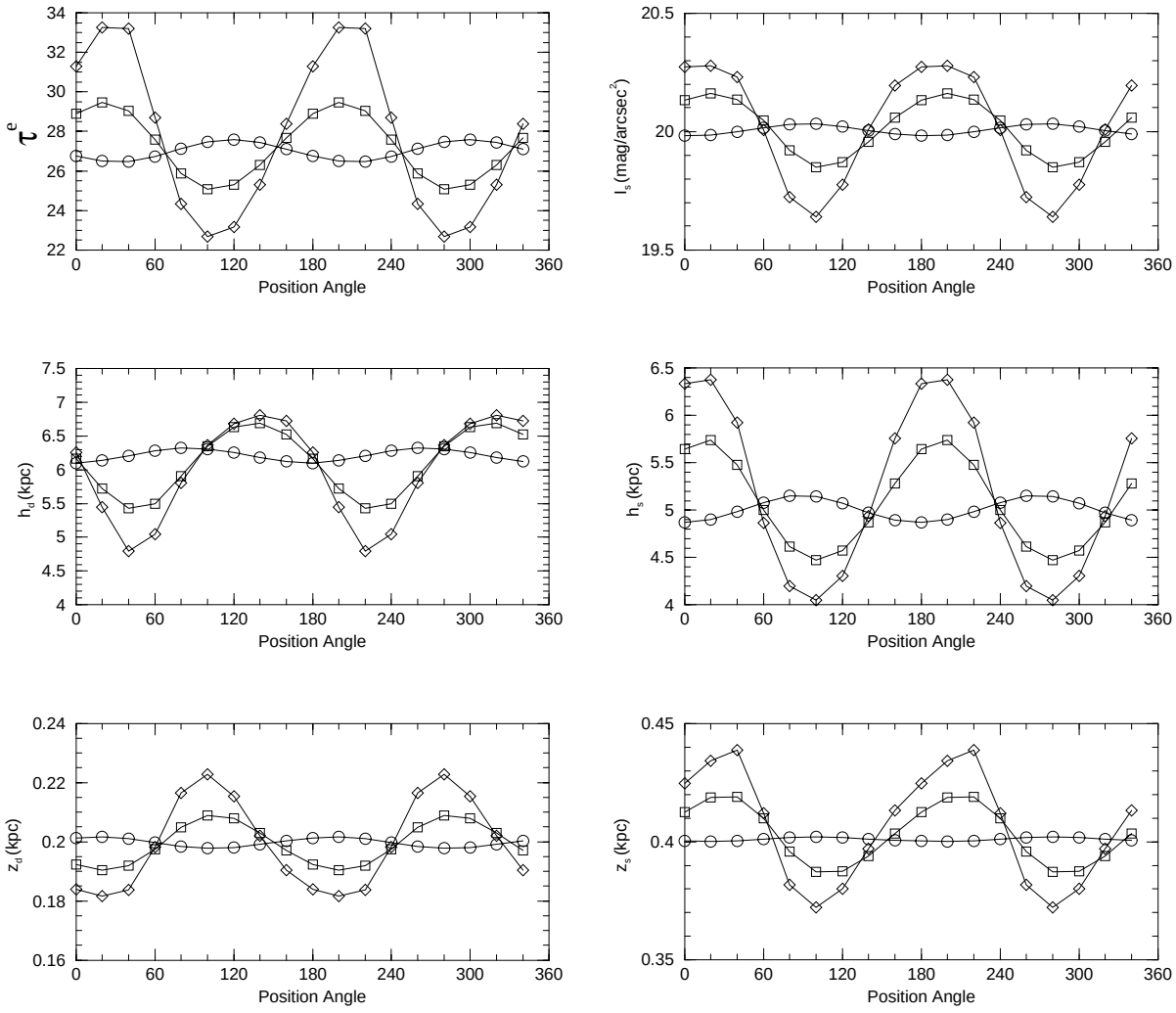

Figure 2.5: The same as in Fig. 4, but the stellar arms are leading the dust arms by 30°.

there is no systematic error in the derived value. The deviations are equally distributed around $\tau^e = 27$, which is what we would have without the spiral structure. The variation is of the same order of magnitude regardless of the pitch angle. The top right graph in Fig. 4 presents the deduced central luminosity of the disk. This graph shows that the variation of the inferred central luminosity of the stellar disk is very small and it is weakly dependent on the pitch angle. In the middle left graph of Fig. 4 the derived scalelength of the dust is presented. The variation of the derived value is about 5% for the 10-degree pitch angle and goes up to 17% for the 30-degree pitch angle. The increase of the variation with increasing pitch angle is expected, because for large pitch angles the spiral arms are loosely wound, thus causing the galaxy to be less axisymmetric. As a result, from some points of view the dust seems to be more concentrated to the center of the galaxy and from other points of view more extended.

In the middle right graph of Fig. 4, that shows the scalelength of the stars, it is evident that the same effect occurs for the stars as well. Certain points of view give the impression of a more centrally condensed disk, while others of an extended disk. The fact

that we have taken the stellar and the dust spiral structure to be in phase (i.e. the dust spiral arms are neither trailing nor leading the stellar spiral arms) causes the deduced scalelengths of the dust and the stars to also vary in phase. The case of a phase difference is examined below.

The bottom left and bottom right graphs of Fig. 4 show the variation of the scaleheight of the dust and the stars respectively. The variation of both scaleheights is negligible. This is an attribute of the formula we used for our artificial galaxy. Since the spiral variation we added to the exponential disks is not a function of z it is expected that in the z direction our artificial galaxy behaves exactly as the exponential model.

There are indications (van der Kruit & Searle 1981;Wainscoat et al. 1989) that the dust arms are not located exactly on the stellar arms. Thus, we re-created the edge-on images, but this time the stellar spiral arms were set to lead the dust arms by 30 degrees. We then fitted the new images with the exponential model and the deduced parameters are shown in Fig. 5. As in Fig.4, the top left graph of Fig. 5 shows the optical depth as a function of position angle. A comparison of this graph with the corresponding graph in Fig. 4 reveals that the variation of the values derived from the new set of images is significantly larger. The origin of this effect is the fact that the dust is either in front of the stars (for some position angles) or behind the stars (for other position angles). A strong dependence on the pitch angle is also evident. Note, however, that the mean of all the derived values is unaffected. The same effect can be seen on the top right graph of Fig. 5, where the derived central luminosity of the disk is plotted. The variation of the central luminosity is again larger than in the previous case, but the mean value is equal to the true one.

In the middle left graph of Fig. 5 we show the scalelength of the dust as a function of the position angle. The variation of the derived dust scalelength can differ as much as 25% for a galaxy with pitch angle equal to 30 degrees. But again the mean value for all position angles is identical to the one we used to create the images. In the middle right graph one can see that the scalelength of the stars also varies as much as 30%,but the mean of all the derived values is the correct one.

The left and right bottom graphs show the variation of the scaleheights of the dust and the stars, which is about 10% for the worst case of a 30-degree pitch angle and is practically zero for a galaxy with more tight arms.

The most important conclusion of all the graphs is that the derived values of all quantities tend to distribute equally around the real value we used to create the artificial images.

2.4 Summary

In our attempt to investigate how significant the spiral structure is when doing radiative transfer modeling of spiral galaxies seen edge-on, we constructed a model galaxy with very prominent spiral arms in the disk. This quite realistic image of the galaxy is now treated as observation and the widely adopted exponential model for the galactic disk is now fitted to the data.

This analysis shows that the plain exponential disk model is a very accurate description

for galactic disks seen edge-on with only small deviations of its parameters from the real ones (typically a few percent). Furthermore, the variation from the real parameters would be averaged out if we could see the same galaxy from several point of views. This is of course impossible for an individual galaxy, but suggests that if the exponential model is used for a statistical study of many edge-on galaxies no systematic error is introduced. Thus, we conclude that the exponential model is a very good approximation of the galactic disks.

Bibliography

Binney J., Merrifield M., 1998, Galactic Astronomy, Princeton University Press, New Jersey

Boroson T., 1981, ApJS, 46, 177

Beckman J.E., Peletier R.F., Knapen J.H., Corradi R.L.M.,Gentet L.J., 1996, ApJ, 467 175

Christensen H. J., 1990, MNRAS, 246, 535

Considere S., Athanassoula E., 1988, A&AS., 76, 365

Corradi R.L.M., Beckman J.E., Simonneau E., 1996 MNRAS, 282, 1005

de Grijs R., 1997, A&AS 190, 1303

de Jong R.S., 1995, Ph.D. thesis, Groningen University

Freeman K. C., 1970, ApJ, 160, 811

Gonzalez R.A., Allen R.J., Dirsch B., Ferguson H.C., Calzetti D., Panagia N., 1998, ApJ, 506 152

Kennicutt R. C. Jr., 1981, AJ, 86, 1847

Kylafis N. D., Bahcall J.N., 1987, ApJ, 317, 637

Puerari I., Dottori H. A., 1992, A&AS., 93, 469

Rix H-W., Zaritsky D., 1995, ApJ, 447, 82

Rudnick G., Rix H-W., 1998, AJ, 116,1163

Serna A., 1997, A&A, 318, 741

Shaw M.A., Gilmore G., 1989, MNRAS, 237, 903

van der Kruit P. C., Searle L., 1981, A&A, 95, 116

Wainscoat R.J., Freeman K. C., Hyland A. R., 1989, ApJ, 337, 163

White R.E., Keel W.C., 1992, Nat, 359, 129

Xilouris E. M., Kylafis N. D., Papamastorakis J., Paleologou E. V., Haerendel G. 1997, A&A, 325, 135

Xilouris E. M., Alton P. B., Davies J. I., et al., 1998, A&A, 331, 894

Xilouris E. M.,Byun Y.I., Kylafis N. D., Paleologou E. V., Papamastorakis J., 1999, A&A, 344, 868

Chapter 3

The influence of clumping on surface brightness fits of edge-on spiral galaxies

We have used a Monte Carlo radiative transfer code to produce edge-on images of dusty galactic disks, allowing a fraction of the dust to be distributed in clumps. Synthetic images have been constructed for different amounts of dust, distributions of clumps and fractions of dust in clumps. We have also considered models with stellar emission embedded in the clumps. The synthetic images have been fitted with models made with smooth distributions of dust and the parameters describing these smooth distributions were determined. Comparing the parameters thus determined with the input parameters of the synthetic images, we have found that neglecting clumping generally results in underestimating the amount of dust in a galaxy, but never more than 40%.

3.1 Introduction

Optical extinction by interstellar grains complicates the study of the stellar and dust content of a spiral galaxy. For moderate to high optical depths, information on the intrinsic properties of each of these components is entangled in the observed surface brightness distribution of the galaxy. The usual way of deriving these properties is by comparing the observations with radiative transfer calculations in a dusty galactic model. A certain degree of complexity is needed in the description of the geometric distributions of a galactic model. Radiative transfer models with simple geometries have been proven to provide equivocal results (Disney et al. 1989). Furthermore, scattering must be taken into account, given the high albedo observed for Galactic dust (Gordon et al. 1997).

A radiative transfer code using the Monte Carlo (MC) technique can, in principle, accommodate any stellar and dust distribution and provide an accurate calculation of the surface brightness for a given model (Witt et al. 1992; Bianchi et al. 1996; de Jong 1996). However, the MC method is time consuming and thus can not be easily included in fitting procedures. For such procedures an approximate treatment of the radiative transfer is more appropriate.

The first approach of such a procedure was introduced by Kylafis & Bahcall (1987, hereafter KB), where vertical profiles of a model galaxy were fitted to observations of NGC 891. In KB's work, scattering is calculated up to the first order and an approximation is introduced for the higher order contributions while the distribution of the dust is assumed to be smooth and exponential along the radial and vertical directions. A similar approximation for the treatment of scattering is adopted by Silva et al. (1998). Other works prefer an exact solution for scattering within simple geometries (Bruzual et al. 1988; Corradi et al. 1996; Xu & Buat 1995). Using the KB method, the radiative transfer equation can be solved for a wide variety of geometries (Byun et al. 1994). Xilouris et al. (1997;1998) improved the original idea of KB and implemented a technique to fit the surface brightness distribution of edge-on spirals. In edge-on galaxies, the effects of extinction are maximized and it is possible to separate the stellar and dust components. The method has been successfully applied to a sample of seven edge-on galaxies (Xilouris et al. 1999) concluding that late-type spiral galaxies have a moderate opacity, with a mean face-on optical depth in the B-band $\tau_{\rm B} \approx 0.8$. As in most of the models used for the description of spiral galaxies, Xilouris et al. (1999) adopt smooth exponential distributions to describe the stellar and dust disks.

Real galaxies exhibit a wide variety of inhomogeneities, like spiral arms, bars, clumps. While it is possible to include these structures in the solution, when fitting an observed image it is desirable to deal with the simplest possible description, in order to limit the number of model parameters. Complex models can then be used to test the reliability of the description obtained with the simple models. This is done, for example, in Misiriotis et al. (2000) where synthetic images of model galaxies with a spiral structure are fitted with a smooth exponential model. They find that plain exponential distributions provide a good description of the galactic disks. The derivation of the stellar and dust parameters is only slightly affected by the spiral pattern.

In this paper we perform a similar exercise to study the influence of dust clumping. In most cases, a clumpy medium exhibits higher transparency than a smooth one of the same dust mass. Therefore, the comparison of real images with smooth models may result in an underestimation of the dust content in a galaxy. Here we use the MC method presented by Bianchi et al. (1999, herafter BFDA) to create model images of clumpy galactic models. The MC images will be fitted with the KB model as in Misiriotis et al. (2000) aiming at determining the efficiency of clumping in hiding the dust when a galaxy is seen edge-on.

Sect. 3.2 describes the method adopted for the comparison and the MC models we have used to produce the synthetic images. A model with exponentially distributed clumps developed for this work is presented in the Appendix. The results are presented in Sect. 3.3 and a summary is given in Sect. 3.4.

3.2 Our Method

Following the procedure described by Misiriotis et al. (2000), we fit images made with the KB method to the MC images of a clumpy model galaxy. Both the MC and the KB models presented here are computed for the V-band. The Henyey & Greenstein (1941) phase function is used with the scattering parameters in the V band albedo $\omega = 0.6$ and

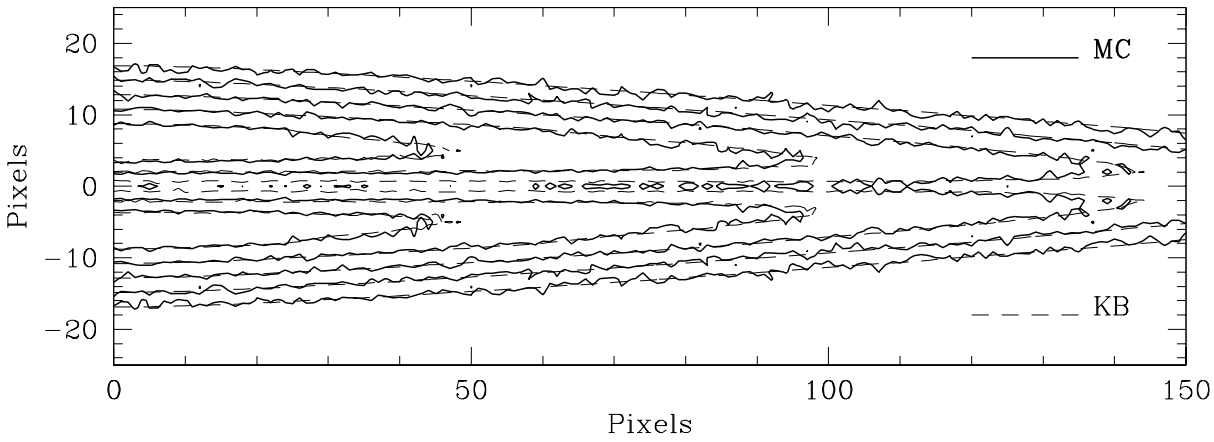

Figure 3.1: Contour plot of a synthetic edge-on image from a Monte Carlo smooth model with $\tau_{\rm V}$=1. Overplotted are isophotes from a Kylafis & Bahcall (1987) type model.

asymmetry $g = 0.6$ (Gordon et al. 1997).

The parameters defining the smooth models are the central face-on surface brightness $I_\star$, the radial scalelength $\alpha_\star$ and the vertical scalelength $\beta_\star$ of the stellar disk, the V-band central face-on optical depth $\tau_{\rm V}$, the radial scalelength α_d and the vertical scalelength β_d of the dust disk. The total intrinsic luminosity $L_\star$ is equal to $4\pi I_\star \alpha_\star^2$ while the dust mass M_d is propotional to $\tau_{\rm V}\alpha_d^2$. The results from the fits are compared to the input parameters of the MC images and are analyzed as a function of the fraction of dust locked into clumps $f_{\rm c}$. Additionally, we study the importance of scattering in the fitted models.

The disk parameters adopted for the MC models are those used in BFDA. For the stellar disk, we have adopted a ratio between radial and vertical scalelengths $\alpha_\star/\beta_\star$ = 11.5. The smooth dust disk has the same radial scalelength as the stellar one and a vertical scalelength $\beta_{\rm d} = 0.4\beta_\star$. In both the simulation and the fitting procedure the dust distribution has been truncated at 4.6 radial scalelengths along the radial direction and at 4 vertical scalelengths along the vertical direction.

In the clumpy images, $\tau_{\rm V}$ defines the total mass of dust in the model, i.e. for the same $\tau_{\rm V}$ the clumpy and the smooth models have the same dust mass. In partially clumpy models, a fraction $f_{\rm c}$ of the total dust mass is distributed in clumps, while the remaining is distributed in a smooth disk of central face-on optical depth $\tau_{\rm V}(1 - f_{\rm c})$. The number of the clumps N_c is determined as described in BFDA.

To cover the full range of $\tau_{\rm V}$ and $f_{\rm c}$ we considered the following optical depths : $\tau_{\rm V}$=0.5, 1, 2 and 5. For each optical depth we produced images with $f_{\rm c}$= 0 (smooth case), 0.25, 0.5, 0.75 and 1.0, resulting in a set of 20 images. Several different sets can be produced depending on how we distribute the dust clumps. We have decided to produce 3 sets.

In the set named "molecular", the dust clumps follow the same distribution as the molecular gas in the Galaxy and their characteristics are based on the Giant Molecular Clouds. Details on these models can be found in BFDA. In this set, the $f_{\rm c}$=1 case is not considered because it would mean that all the dust is distributed in a molecular ring and an exponential model is not reccommended to reproduce such a distribution.

A second set of models named "exponential" was produced with the dust clumps

following the same exponential distribution as the smooth dust disk while the stars were smoothly distributed. The exponential models are described in detail in the Appendix.

In the third set of models named "embedded" the clumps are distributed exponentially, while a fraction of starlight $f_{\rm emb}$=0.5 was embedded in the dust clumps. For the case of $f_{\rm c}$=0, there can be no $f_{\rm emb}$=0.5 because when there are no clumps there is nowhere to embed the embedded starlight.

The MC images of the clumpy model galaxies were constructed to be as similar as possible to observations. The images cover 151 pixels along the major axis from the galactic center to the border of the image, while the radial scalelength of the stellar and the dust disk is equal to 50 pixels. For each image, photons are gathered in a finite inclination band (Bianch et al. 1996) which was chosen to be 1°. The number of photons for the MC simulations was chosen so that a realistic signal to noise ratio was achieved.

The fitting was performed as in Misiriotis et al. (2000), by minimizing the sum of the squares of the differences between the MC and the KB images. In Fig. 3.1 we present a contour plot of an edge-on image from a MC smooth model ($f_{\rm c}$=0) together with the isophotes of the same model image, produced using the KB method. The coincidence of the MC and KB model images demonstrates the consistency of the two methods.

3.3 Results of the fits

3.3.1 Testing of the codes and the effects of scattering

Since the two radiative transfer methods (BFDA and KB) used in this work have been developed independently and with different algorithms, we checked for their consistency in several ways. We first produced images without scattering and without clumps using the MC method and fitted them with the KB method. The fits were able to retrieve all the parameters with a scatter smaller than 4%.

We then analyzed the smooth models ($f_{\rm c}=0$) described in the previous section. Two fits were produced for each MC image. In the first, the fitting model is computed without scattering, while in the second scattering is taken into account. This way we can quantify both the importance of scattering in fits of edge-on galaxies and the approximation of KB in their treatment of scattering.

In Fig. 3.2 we show the parameters I_0 and $\tau_{\rm V}$ whose behavior changes the most when passing from an absorption-only fit to a fit including scattering. It is well-known that scattering reduces the effective absorption of a dusty medium, thus resulting in an increased surface brightness. When scattering is not included (dotted lines in Fig. 3.2), the fitting procedure compensates for this by reducing the optical depth of the dust disk and by increasing the central surface brightness of the stellar disk. The underestimate of the dust content is the dominant effect, because the stellar luminosity is significantly constrained by the parts of the galaxy that lie outside of the dust lane, where the absorption is negligible. Absorption-only fits result in an underestimate of the face-on optical depth ranging from 10% for $\tau_{\rm V}$=0.5 to 25% for $\tau_{\rm V}$=5. As for the central face-on surface brightness ($I_\star$), the maximum discrepancy is an overestimation by 10% for $\tau_{\rm V}$=0.5

When scattering is included, the fitted parameters are very close to the input values (solid lines in Fig. 3.2). The $\tau_{\rm V}$ plot confirms the validity of the approximation for

scattering introduced by Kylafis & Bahcall (1987), at least for low-to-moderate optical depths. Even for τ_V=5, the derived optical depth is only 15% larger than the input value. All the other parameters derived from fits with scattering were found to vary within less than 4% of the input values.

3.3.2 The effect of clumping

The quality of the fits is poorer when synthetic images from clumpy models are analyzed. The sum of the squares of the differences between input data and fitted models increases by about an order of magnitude. Furthermore, in many cases it was possible to find a few equally acceptable fits, corresponding to local minima. While some parameters of KB models may change from minimum to minimum, we found that the derived dust mass and intrinsic luminosity are nearly the same.

In Fig. 3.3 we have plotted the derived normalized dust mass and intrinsic luminosity, as functions of f_c and of τ_V, for the "molecular" models, (BFDA; top row); for the "exponential" models (middle row) and for the "embedded" models (bottom row).

The derived dust masses, normalized to the input values, are shown in the left column of Fig. 3.3. The trend of the dust mass with f_c does not depend on the type of clumping or on the optical depth of the model, the amount of detected dust decreases with increasing f_c. For the two sets of models without embedded stellar emission ("molecular" and "exponential"), the dust mass is underestimated by less than 10% for f_c=0.25 to about 20-30% for f_c=0.75. For the "exponential" set for f_c=1, the underestimate reaches values of 40%. For the "embedded" models the fitting procedure recovers the input dust quite well. All the dust is detected for f_c=0.25 and only 20% is missed for f_c=0.75.

The results of the fitting procedure for the intrinsic, dust-free, luminosity $L_\star$ are shown in the right column of Fig. 3.3, again normalized to the input value. As for the dust mass, the trends with f_c for different models are very similar and do not depend sensitively on the value of τ_V. The fitting model overestimates the luminosity with increasing f_c. For f_c=0.75 and $f_{emb} = 0$, the derived luminosity is about 20% larger than the input value.

The overestimate of the luminosity drives the fitting procedure to increase the dust mass in order to obscure the additional starlight. If the luminosity was not overestimated then even less dust would be needed to fit the synthetic images. A simple major-axis analysis, i.e. a comparison of the radial profiles along the dust lane suggests that the smooth model detects only half of the dust mass (BFDA) and leads to the conclusion that clumping causes an underestimate of the face-on optical depth.

This is not the case for the fits shown here. The fitting procedure tries to interpret the reduced extinction caused by clumping by decreasing the dust radial scalelength α_d and keeping the optical depth high (actually, to a value similar to the input one), rather than decreasing τ_V and keeping α_d fixed. The reason for this may be that the surface brightness in models with clumping departs from that of a smooth exponential disk, when *all* the image, and not only a single profile, is fitted. Given the general trend of the retrieved data, it does not seem probable that we have systematically hit local minima of the fit.

We have shown that the trend of dust mass underestimation is nearly independent of the optical depth of the model. This may suggest that the same percentage of dust is missed when fitting a galaxy at different wavelengths. Therefore, clumping should not

affect the determination of the extinction law from fits of a galaxy in different bands.

As long as the dust properties do not vary significantly with wavelength, as in the optical range, it is possible to interpret the absence of a trend with τ_V as an absence of a trend with λ.

3.4 Summary

We have used a Monte Carlo code for the radiative transfer in a clumpy galactic model to produce synthetic edge-on images of spiral galaxies. The images have then been analyzed using the fitting procedure of Xilouris et al. (1997; 1998; 1999), that uses the method of Kylafis & Bahcall (1987) to compute the radiative transfer in smooth galactic models. We first checked for the consistency of the two independent codes, by analyzing smooth MC images. It was possible to retrieve the parameters of the MC models within 4% of their original value and we confirmed the importance of scattering in the radiative transfer simulations. The dust mass is significantly underestimated when scattering is not included in the fitting routine.

We have then studied the influence of clumping on the derivation of the parameters, when a synthetic image of a clumpy galactic model is analyzed through a simpler (and more controllable) smooth model. As expected, using a smooth model leads to an underestimation of the dust content of the galaxy. For the distribution of clumps adopted in this paper, about 20-30% of the dust mass is missed by the fitting, the value depending more on the fraction of dust located in clumps rather than on the details of the clumps distribution or the total dust mass of the model. In addition, clumping alters the surface brightness distribution with respect to that of a smooth exponential model, thus making the fit more difficult. This may explain the overestimation of the intrinsic luminosity in models with clumping.

Recent analyses of dust emission at $\lambda > 100\mu$m suggest that the amount of dust in spiral galaxies is larger than what derived from fits of edge-on surface brightness profiles (Bianchi et al., 2000; Popescu et al., 2000; Misiriotis et al., 2001). While clumping has been imputed to as a possible cause for this discrepancy, the small underestimation produced by the clumpy distributions presented here is not able to explain the magnitude of the effect.

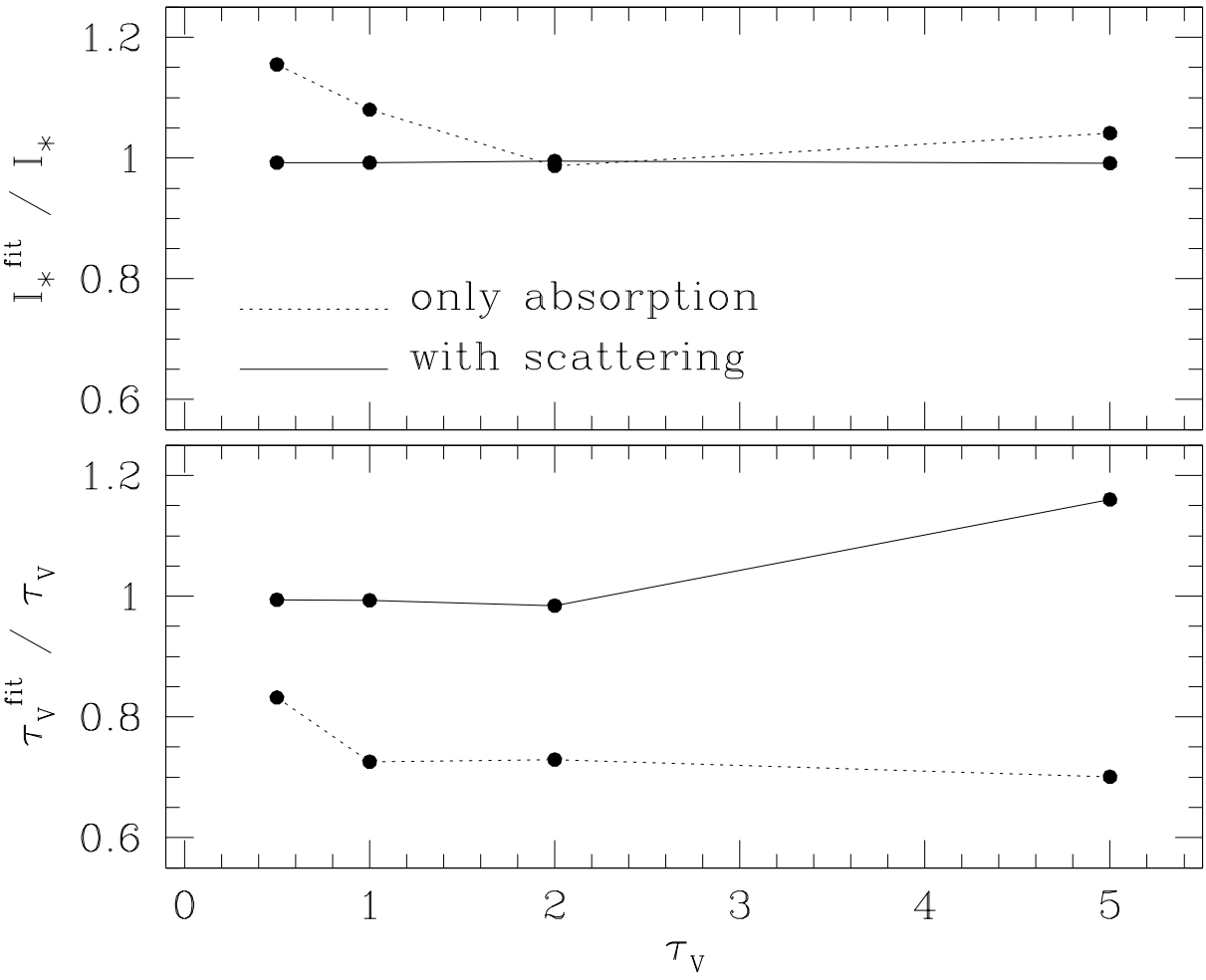

Figure 3.2: The derived $I_\star$ and τ_V normalized to the input values as functions of the optical depth of the model. Results for fits with and without scattering are shown.

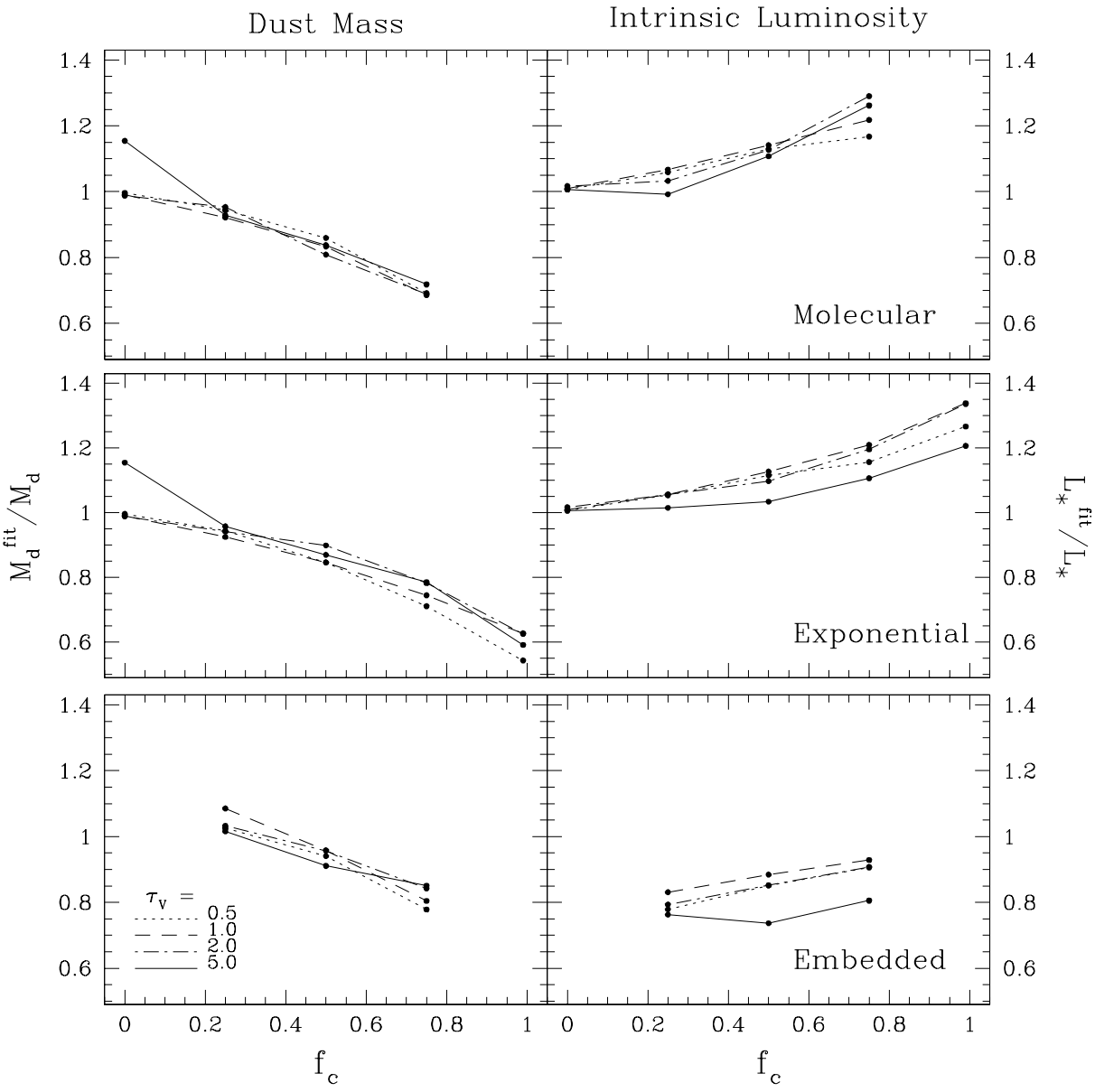

Figure 3.3: Normalized dust mass (left column) and normalized intrinsic luminosity (right column) derived by fitting the Monte Carlo simulations of Section 3.2, as functions of the fraction f_c of dust locked up in clumps. The values have been normalized to the input dust mass and intrinsic luminosity. Results are presented for models with optical depths τ_V= 0.5 (dotted lines), 1 (dashed), 2 (dot-dashed) and 5 (solid). The plots in the top row show the results for the clumpy model of BFDA with fraction of embedded stellar emission f_{emb}=0; the middle row refers to the models with clumps distributed exponentially and f_{emb}=0; the bottom row to exponentially distributed clumps, but with f_{emb}=0.5. Results for the smooth models ($f_c = 0$) are plotted in both the top and middle row .

Bibliography

Bianchi S., Ferrara A., Davies J. I., Alton P. B., 2000, MNRAS, 311, 601

Bianchi S., Davies J. I., Alton P. B., 2000, A&A, 359, 65

Bianchi S., Ferrara A., Giovanardi C., 1996, ApJ, 465, 127

Bruzual A. G., Magris G., Calvet N., 1988, ApJ, 333, 673

Byun Y. I., Freeman K. C., Kylafis N. D., 1994, ApJ, 432, 114

Corradi R. L. M., Beckman J. E., Simonneau E., 1996, MNRAS, 282, 1005

de Jong R., 1996, A&A, 313, 377

Disney M., Davies J., Phillipps S., 1989, MNRAS, 239, 939

Gordon K. D., Calzetti D., Witt A. N., 1997, ApJ, 487, 625

Henyey L. G., Greenstein J. L., 1941, ApJ, 93, 70

Kylafis N. D., Bahcall J. N., 1987, ApJ, 317, 637

Misiriotis A., Kylafis N. D., Papamastorakis J., Xilouris E. M., 2000, A&A, 353, 117

Misiriotis A., Popescu C. C., Tuffs R. J., Kylafis N. D., 2001, A&A, 372, 775

Popescu C. C., Misiriotis A., Kylafis N. D., Tuffs R. J., Fischera J., 2000, A&A, 362, 138

Silva L., Granato G. L., Bressan A., Danese L., 1998, ApJ, 509, 103

Witt A. N., Thronson H. A. Jr., Capuano J. M. Jr., 1992, ApJ, 393, 611

Xilouris E. M., Byun Y. I1., Kylafis N. D. Paleologou E. V., Papamastorakis J., 1999, A&A, 344, 868

Xilouris E. M., Alton P. B., Davies J. I., Kylafis N. D., Papamastorakis J., Trewhella M., 1998, A&A, 331, 894

Xilouris E. M., Kylafis N. D., Papamastorakis J., Paleologou E. V., Haerendel G., 1997, A&A, 325, 135

Xu C., Buat V., 1995, A&A, 293, L65

Young J. S., Scoville N. Z., 1991, ARA&A, 29, 581

3.5 Appendix. Models with exponentially distributed clumps

In BFDA it was assumed that all the material associated with the molecular phase in a spiral galaxy is in Giant Molecular Clouds. Radiative transfer models were produced assuming that dust clumps are distributed as the molecular gas in the Galaxy, i.e. in a ring-like structure. However, most of luminous, face-on, late-type galaxies, and a good fraction of early-type spirals, show a radial exponential distribution for the H_2 column density (Young & Scoville, 1991). For the sake of completeness, we briefly present here a set of models with an exponential distribution for the dust clumps. The clumps distribution has the same scalelengths as the smooth dust disk. All the other parameters are the same as in BFDA.

The effects of clumping in these models are not very different from those obtained adopting the Galactic H_2 distribution. Exponentially distributed clumps make the models less transparent, but only slightly. For example, in the τ_V=2 model with fraction of gas in clumps f_c=0.75, 15% of the radiation is absorbed, while in BFDA it was 12%. We recall that in a smooth model 19% of the radiation is absorbed. For models with embedded stellar emission, the difference is even smaller, because of the increased contribution of the absorption within each clump. The number of clumps and their opacity are independent of the assumed clump distribution and are the same as in BFDA.

As in BFDA, the largest differences between homogeneous and clumpy simulations are for the edge-on profiles. In Fig. 3.4 we show the edge-on major-axis profiles for the BFDA models and for the models with exponential clumping, for τ_V=2, f_c=0.25,0.5,0.75 and f_{emb}=0. The profile for a smooth τ_V=2 disk is shown as a reference. Because of the exponential distribution, the profiles of the new clumpy models are similar to those for smooth exponential disks, independently of f_c and f_{emb}. Instead, BFDA models show the effects of the ring-like clumping distribution, even when f_{emb}=0.

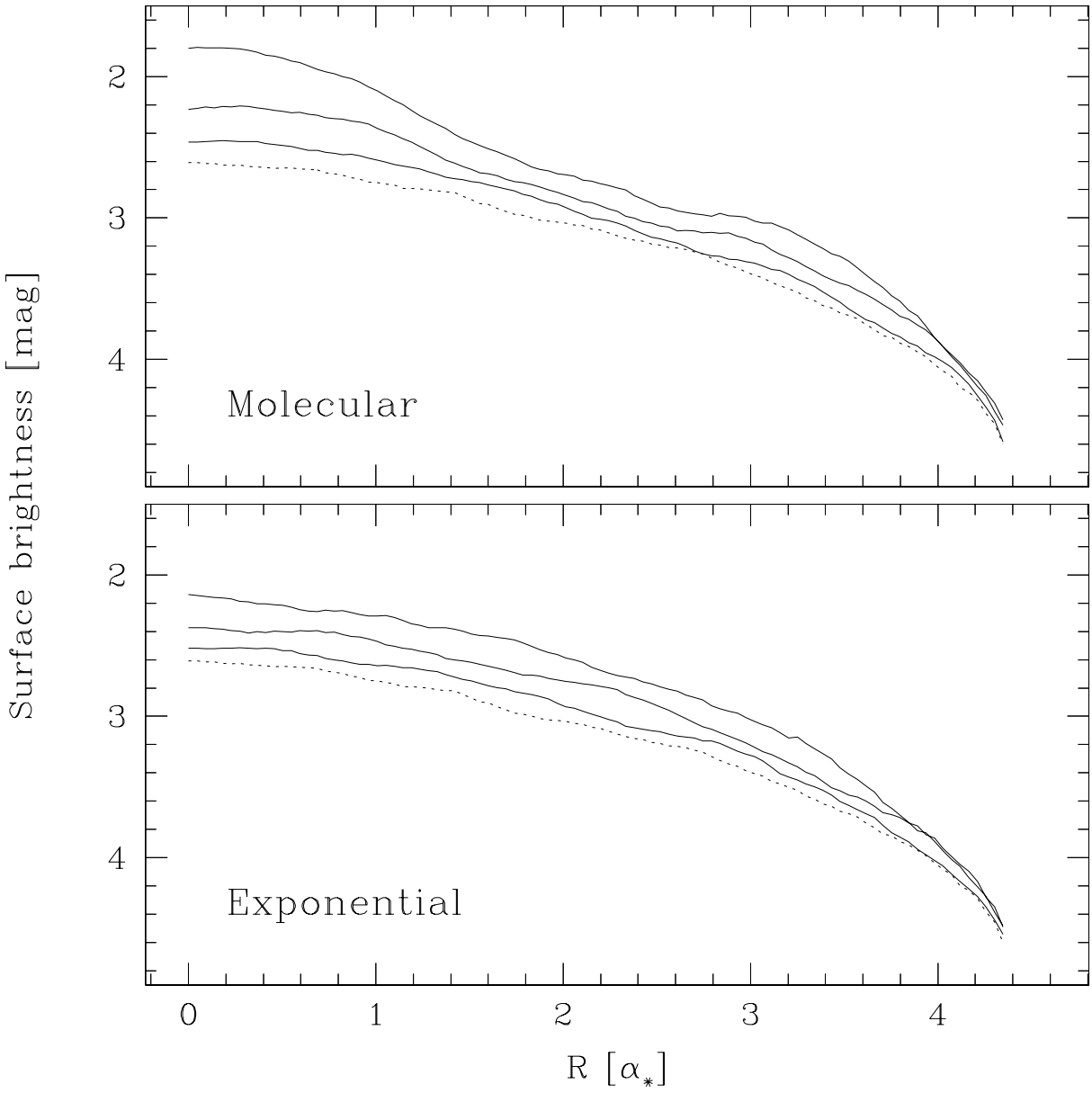

Figure 3.4: Major-axis edge-on profiles for τ_V=2 models with molecular (top panel) and exponential (bottom panel) clumping, for f_c=0.25,0.5 and 0.75 (from bottom to top, solid lines). As a reference, we also show the profile for a τ_V=2 smooth model (dotted lines).

Chapter 4

Modelling the spectral energy distribution of galaxies. I. Radiation fields and grain heating in the edge-on spiral NGC891

We describe a new tool for the analysis of the UV to the sub-millimeter (sub-mm) spectral energy distribution (SED) of spiral galaxies. We use a consistent treatment of grain heating and emission, solve the radiation transfer problem for a finite disk and bulge, and self-consistently calculate the stochastic heating of grains placed in the resulting radiation field.

We use this tool to analyse the well-studied nearby edge-on spiral galaxy NGC891. First we investigate whether the old stellar population in NGC891, along with a reasonable assumption about the young stellar population, can account for the heating of the dust and the observed far-infrared and sub-mm emission. The dust distribution is taken from the model of Xilouris et al. (1999), who used only optical and near-infrared observations to determine it. We have found that such a simple model cannot reproduce the SED of NGC891, especially in the sub-mm range. It underestimates by a factor of 2-4 the observed sub-mm flux.

A number of possible explanations exist for the missing sub-mm flux. We investigate a few of them and demonstrate that one can reproduce the observed SED in the far-infrared and the sub-mm quite well, as well as the observed radial profile at 850 μm.

For the models calculated we give the relative proportion of the dust radiation powered by the old and young stellar populations as a function of FIR/sub-mm wavelength. In all models we find that the dust is predominantly heated by the young stellar population.

4.1 Introduction

Dust grains can be considered as test particles for the intrinsic radiation field in galaxies. Observations of their emission in the infrared (IR), combined with optical and ultraviolet (UV) observations of the light from stars, attenuated by the grains, should, in principle,

strongly constrain the intrinsic distribution of stellar luminosity and dust in galaxies. This would address the fundamental question of optical thickness in galactic disks and allow evaluation of optical and IR observational data in terms of physical (e.g., star formation history) rather than empirical (e.g., colours) parameters. Ultimately, such analysis techniques will be necessary to interpret the evolution of the UV - far-infrared (FIR)/sub-millimeter (sub-mm) spectral energy distribution (SED) of galaxies and the IR background radiation over cosmological timescales.

However, even for galaxies in the local universe, technical difficulties are considerable from both theoretical and observational stand points. From the theoretical point of view, it is necessary to solve the radiation transfer problem for a finite disk, and self consistently calculate the stochastic heating of grains placed in the resulting radiation field using realistic grain models. To that must be added the problem that disks are fundamentally inhomogeneous on different scales. From the observational point of view, it is only now becoming possible to obtain resolved images covering the mid-IR to sub-mm spectral range for nearby galaxies.

Because of these difficulties, the origin of the FIR emission in local universe spiral galaxies is still a subject of debate. Based on models of dust heating in various environments (e.g., Mezger et al. 1982; Cox et al. 1986), and from comparison of IRAS data with optical properties of galaxies, several studies concluded that a substantial fraction of the FIR emission from galaxies could be due to dust heated by the diffuse interstellar radiation field (ISRF), the remaining part being due to localised sources around OB stars in star-forming regions (e.g., de Jong et al. 1984; Walterbos & Schwering 1987). Some later papers, however, suggested that the correlation between Hα and FIR emission implies that OB stars by themselves can account for all the dust heating, so that there is no need for an additional contribution to heating by the ISRF (e.g., Devereux & Young 1990). By contrast, there have been a series of papers (e.g., Xu et al. 1994) which concluded that the non-ionising UV accounts for most of the energy absorbed by dust. They showed that the FIR/radio correlation can be separated into a warm-FIR/thermal-radio correlation which is due to massive ionising stars ($> 20\,\mathrm{M}_\odot$), and a cool-FIR/nonthermal-radio correlation, principally due to intermediate mass stars ($5 - 20\,\mathrm{M}_\odot$) - the supernova progenitors. A heating component from the old stellar population was also needed to account for the non-linearity of the correlation, but this accounts only for about a third of the heating.

In this paper we describe a new method for the analysis of the radiation energy budget in edge-on spiral galaxies, as part of an effort to develop a theoretical tool for the interpretation of the SED in spiral galaxies. The method presented here is based on some knowledge of the primary radiation field (i.e., from stars) in spiral galaxies and the dust distribution in them. For edge-on spirals, it has been demonstrated (Xilouris et al. 1997; 1998; 1999) that it is possible to determine the distribution of older stars and associated dust from analysis of optical and near-infrared (NIR) images. Thus, the diffuse radiation field in the galaxy from these optical bands can be computed quite accurately. The diffuse radiation field in the UV is generally not so well constrained by the UV data alone, due to the larger optical depth of disks in the UV. This younger stellar component is parameterised in terms of a recent star-formation rate (SFR) and it can be observationally constrained in the case that a direct, optically thin indicator, such as radio free-free emission, is available. Solving the radiation transfer problem within the disk and bulge,

and calculating the heating of grains we can determine the diffuse FIR/sub-mm emission. Potentially, further contributions arising from emission from localised sources need to be added to the diffuse component. Then, because the dust is optically thin in the FIR, the predicted emission can be compared with observations.

We apply the above method to the well-known edge-on spiral galaxy NGC891, for which we assume a distance of 9.5 Mpc (van der Kruit & Searle 1981). This is one of the most extensively observed edge-on galaxies in the nearby universe, which makes it ideal for a verification of our modelling technique. The analysis of a sample of 6 more edge-on galaxies is in progress (Misiriotis et al. 2000a). Modelling edge-on spiral galaxies has several advantages, mainly when investigating them in the optical band. One advantage is that, in this view of a galaxy, one can easily separate the three main components of the galaxy (i.e., the stellar disk, the dust and the bulge). Another advantage is that the dust is very prominently seen in the dust lane, and thus its scalelength and scaleheight can be better constrained. A third advantage is that many details of a galaxy that are evident when the galaxy is seen face-on (e.g., spiral arms), are smeared out to a large degree when the galaxy is seen edge-on (Misiriotis et al. 2000b). Thus, a simple model with relatively few parameters can be used for the distribution of stars and dust in the galaxy. However, the third advantage comes with disadvantages, especially when trying to model the galaxy in all wavelength ranges, including UV and FIR/sub-mm. Thus, in edge-on galaxies it is very difficult to see localised sources (i.e., HII regions), in which the radiation can be locally absorbed and thus not contribute to the diffuse radiation field. Also, if the galaxy has a thin (young) stellar/dust disk, highly obscured by the dust lane in the plane of the galaxy, then this disk cannot be inferred from observations in the optical/NIR spectral range. In passing we mention that throughout this paper we will use the terms "thin/thick disks" to describe their scaleheights, and not their optical thickness.

The goal of this paper is to find the simplest phenomenological description of NGC891 that can adequately account for the observed optical to sub-mm SED. In particular we investigate what fraction of the FIR is accounted for by the Xilouris et al. (1999) model, namely by a disk of dust, heated by a diffuse, smooth, optically emitting, old stellar disk and bulge, supplemented by a diffuse, smooth, UV emitting disk of newly-formed stars. We refer to this model as the "standard model". We will show that this model fails to reproduce the observed SED of the galaxy at FIR/sub-mm wavelengths. We investigate then different possibilities to explain the origin of the missing FIR/sub-mm flux.

Recently there have been several works modelling the SED of galaxies from the UV to the sub-mm (Silva et al. 1998, Devriendt et al. 1999). Their method consists of using models for photometric and/or spectrophotometric and chemical evolution of galaxies in order to fit the observed SED. For example Silva et al. (1998) used a chemical evolution code to follow the SFR, the gas fraction, and the metallicity of the galaxies. In their approach the parameters describing the star formation history as well as the geometrical parameters of the intrinsic distribution of stars and dust are left as fitting parameters. While this approach was very successful in fitting the SED of different types of galaxies, it implies the use of many free parameters. Furthermore, a more detailed description of the geometry of the galaxy is indispensable for an accurate determination of the dust content in individual cases.

This paper is organised as follows: In Sect. 2 we describe our "standard model" for the diffuse dust and radiation field, including the optical properties of the dust grains, and the derivation of the diffuse radiation field powered by the old and the young stellar populations. In Sect. 3 we give the results of our calculations, in terms of integrated SED for the "standard model" and in Sect. 4 we supplement our model with the contribution of localised sources. Since the "standard model" fails to reproduce the observed SED, we discuss in Sect. 5 the origin of the FIR emission, considering four possibilities to produce the missing IR component. From these, the two dust disk model, together with the clumpy scenario constitute the simplest solutions we have been able to identify to describe the origin of the missing infrared component. In Sect. 6 we give our results in terms of radial profiles and in Sect. 7 we discuss the contribution of radiation at different wavelengths in heating the dust. In Sect. 8 we summarise our results and give our conclusions.

4.2 The model

4.2.1 The properties of the dust grains

We consider only the spectral range $\lambda \geq 40\,\mu$m as our dust model does not include Polycyclic Aromatic Hydrocarbon (PAH) molecules, which are important for $\lambda \leq 15\,\mu$m and may even contribute at $\lambda = 25\,\mu$m, a point that is still very uncertain. For example, Désert et al. (1990) proposed a dust model in which 48% of the IR emission at $25\,\mu$m (for dust in the solar neighbourhood) is emitted by the PAH molecules as continuum emission. Draine and Anderson (1985) proposed that the IR emission at $25\,\mu$m and shorter wavelengths can be explained by enhancing the number of small grains. Our restriction to the spectral range $\lambda \geq 60\,\mu$m allows us to avoid the uncertainties introduced by a different dust component (PAHs or modified grain size distribution).

In characterising the dust properties we thus considered spherical "astronomical grains" for two component materials - graphite and silicate - of the Mathis et al. (1977; hereafter MRN) interstellar grain model. MRN have proposed that the observed interstellar extinction of star-light may be produced by a mixture of graphite and silicate particles with a simple power-law distribution of sizes

$$dN_i = N_i(a)\,da = N_i\,a^{-k}\,da \tag{4.1}$$

where dN_i is the number of grains of type i with radii in the interval $[a, a+da]$, and $k = 3.5$. We consider the lower and the upper cutoffs to the size distribution to be respectively $a_{\rm min} = 10$ Å and $a_{\rm max} = 0.25\,\mu$m. The graphite and silicate abundances were taken from Draine & Lee (1984, hereafter DL), and are only slightly different from those found by MRN; DL proposed a mixture of 53% silicates ($N_{\rm Si}$) and 47% graphites ($N_{\rm Graphite}$), which were chosen to fit the extinction curve in our Galaxy, and which we also adopted for NGC891.

The absorption efficiencies $Q_{\rm abs}(\lambda, a)$, the scattering efficiencies $Q_{\rm scat}(\lambda, a)$ and the scattering phase function $g(\lambda, a)$ were taken from Laor & Draine (1993). The absorption

coefficient $\kappa_{\rm abs}$, the scattering coefficient $\kappa_{\rm scat}$ as well as the averaged anisotropy parameter of the Henyey-Greenstein scattering phase function g can then be derived by integrating $Q_{\rm abs}(\lambda, a)$, $Q_{\rm scat}(\lambda, a)$, and $g(\lambda, a)$, respectively, over the size distribution

$$\kappa_{\rm abs}(\lambda) \sim \int_{a_{\rm min}}^{a_{\rm max}} \sum_i N_{\rm i}\, a^{-{\rm k}} da\, \pi\, a^2\, Q_{\rm abs}(\lambda, a) \tag{4.2}$$

$$\kappa_{\rm scat}(\lambda) \sim \int_{a_{\rm min}}^{a_{\rm max}} \sum_i N_{\rm i}\, a^{-{\rm k}} da\, \pi\, a^2\, Q_{\rm scat}(\lambda, a) \tag{4.3}$$

$$g(\lambda) = \frac{\int_{a_{\rm min}}^{a_{\rm max}} \sum_i N_{\rm i}\, a^{-{\rm k}} da\, \pi\, a^2\, g(\lambda, a) Q_{\rm scat}(\lambda, a)}{\int_{a_{\rm min}}^{a_{\rm max}} \sum_i N_i\, a^{-k} da\, \pi\, a^2\, Q_{\rm scat}(\lambda, a)} \tag{4.4}$$

with the extinction coefficient $\kappa_{\rm ext} = \kappa_{\rm abs} + \kappa_{\rm scat}$.

As the $60 - 100\,\mu$m data are expected to contain a significant amount of emission from small grains not in equilibrium with the radiation field, it is necessary to model the stochastic emission from the dust. For this calculation we adopted the heat capacities of silicate grains from Guhathakurta & Draine (1989), which were derived as a fit to experimental results for SiO_2 and obsidian at temperatures $10 < T < 300\,$K (Leger et al. 1985), with a simple extrapolation for $T > 300\,$K. For graphite grains the heat capacities were taken from Dwek (1986).

4.2.2 Derivation of the diffuse optical and UV radiation field.

Our first step is to estimate the diffuse radiation field at any point in the galaxy. The most straightforward way to do this is to solve the radiative transfer equation (RTE) for a given distribution of emitters and absorbers of radiation. In this section we will consider the distribution of emitters and absorbers as derived from optical wavelengths by Xilouris et al. (1998,1999), while at the UV wavelengths we will fix the parameters describing the geometry of the emitters and use population synthesis models to parameterise the amplitude of the UV radiation.

Radiation transfer

In this subsection we will describe our solution of the RTE. Our method is based on that of Kylafis & Bahcall (1987). This method will be briefly described here for the sake of completeness. Let us introduce the RTE (Mihalas 1978) for a time independent radiation field along a line of sight, at a fixed wavelength

$$\frac{dI(s,\hat{n})}{ds} = -\kappa_{ext}\, I(s,\hat{n}) + \eta_0(s,\hat{n}) + \eta_s(s,\hat{n}) \tag{4.5}$$

where $I(s,\hat{n})$ is the specific intensity of the radiation field at a point s on the line of sight (defined by $\hat{n}$), κ_{ext} is the extinction coefficient for the wavelength considered, ds is an infinitesimal length element along the line of sight, η_0 is the emissivity along the line of

sight due to primary sources (stars) and η_s is the emissivity due to scattering into the line of sight. For coherent scattering, η_s is given by

$$\eta_s(s,\hat{n}) = \omega\,\kappa_{ext}\int I(s,\hat{n}')\,p(\hat{n},\hat{n}')\,\frac{d\Omega'}{4\pi} \tag{4.6}$$

where $p(\hat{n},\hat{n}')$ is the Henyey-Greenstein phase function (Henyey & Greenstein 1941), parameterised by the anisotropy parameter g, and ω is the scattering albedo for the wavelength considered, defined as $\omega \equiv \kappa_{scat}/\kappa_{ext}$. Let $I = I_0 + I_1 + ... + I_n + ...$, where I_0 is the intensity of photons that come directly from the primary sources, I_1 the intensity of photons that have been scattered once after leaving the primary sources and I_n the intensity of photons that have suffered n scatterings. The intensities I_n satisfy the following equations (Henyey 1937)

$$\frac{dI_n(s,\hat{n})}{ds} = -\kappa_{ext}\,I_n(s,\hat{n}) + \eta_n(s,\hat{n}) \tag{4.7}$$

where $\eta_n(s,\hat{n})$ is the emissivity due to photons scattered n times, and is given by

$$\eta_n(s,\hat{n}) = \omega\kappa_{ext}\int I_{n-1}(s,\hat{n}')\,p(\hat{n},\hat{n}')\,\frac{d\Omega'}{4\pi} \tag{4.8}$$

Eq. (7) can be solved for as high order of n as allowed by the given hardware and/or software. In our method, we calculate I_0 and I_1 and approximate the higher orders according to Kylafis & Bahcall (1987). Therefore, the solutions are given by

$$I_{0,1}(s,\hat{n}) = \int_0^s ds'\,\eta_{0,1}(s',\hat{n})\exp[-\tau(s,s')] \tag{4.9}$$

while for $n > 1$,

$$I_{n+1} = I_n\frac{I_1}{I_0} \tag{4.10}$$

where $\tau(s,s')$ is the optical depth between s and s'. Given the intensity of the radiation field at a point, the energy density can be calculated by (Mihalas 1978)

$$u(x,y,z) = c^{-1}\int I(x,y,z,\hat{n})\,d\Omega \tag{4.11}$$

Optical radiation field and dust distribution

The determination of the intrinsic stellar content of a galaxy is often difficult because of the uncertainty introduced by dust obscuration. However, in the case of edge-on galaxies, dust obscuration can be used to our benefit to determine the spatial distribution of dust. In an edge-on galaxy, dust becomes visible as a very prominent dust lane along the major axis of the galaxy. The effects of the dust are strong enough to allow the existence of a fairly constrained model for the distribution of old stars and associated dust (Xilouris et al. 1997; 1998;1999; Kuchinski et al. 1998; Ohta & Kodaira 1995). This does not include, however, any stellar population with a scaleheight small enough to be effectively completely hidden by the dust. Such a stellar population will be discussed in Sect. 2.2.3.

NGC891 was modeled (Xilouris et al. 1998,1999) by fitting an artificial image produced by radiative transfer on observations in an attempt to conclude on the dust morphology. In this section we will adopt the latest model for NGC891 (Xilouris et al. 1999). In this model, the emissivity is described by an exponential disk and a de Vaucouleurs bulge, while the dust resides in a pure exponential disk. The parameters describing the stars and the dust are determined in 5 wavebands (B, V, I, J, K).

For the stellar emissivity the following formula is used

$$\eta_0(R,z) = L_s \exp\left(-\frac{R}{h_s} - \frac{|z|}{z_s}\right) + L_b \exp(-7.67\, B^{1/4})\, B^{-7/8} \tag{4.12}$$

In this expression the first part describes an exponential disk, and the second part describes the bulge, which in projection is the well-known $R^{1/4}$-law (Christensen 1990). Here R and z are the cylindrical coordinates, L_s is the stellar emissivity per unit volume per steradian at the center of the disk and h_s and z_s are the scalelength and scaleheight respectively of the stars in the disk. For the bulge, L_b is a normalisation constant, while B is defined by

$$B = \frac{\sqrt{R^2 + z^2\,(a/b)^2}}{R_e} \tag{4.13}$$

with R_e being the effective radius of the bulge and a and b being the semi-major and semi-minor axis respectively of the bulge. In this paper we will refer to the exponential disk described above as to the old stellar disk, in order to differentiate it from the young stellar disk emitting in UV (Sect. 2.2.3).

For the dust distribution a similar expression as that adopted for the stellar distribution in the disk is used, namely

$$\kappa_{ext}(\lambda,R,z) = \kappa_{ext}(\lambda,0,0)\, \exp\left(-\frac{R}{h_d} - \frac{|z|}{z_d}\right) \tag{4.14}$$

where $\kappa_{ext}(\lambda,0,0)$ is the extinction coefficient at the center of the disk for the wavelength considered, and h_d and z_d are the scalelength and scaleheight respectively of the dust. The central optical depth of the model galaxy seen face-on is

$$\tau^f(\lambda) = 2\,\kappa_{ext}(\lambda,0,0)\, z_d \tag{4.15}$$

The parameters determined for NGC891 are presented in Table 1. The total amount of dust derived from this model is $M_{dust} = 5.6 \times 10^7\,\mathrm{M}_\odot$ (Xilouris et al. (1999).

The extinction coefficients $\kappa_{ext}(\lambda,0,0)$ were derived as fitting parameters (Xilouris et al. 1999), separately for each of the five wavebands used for modelling the galaxy. They were then used to calculate the absorption of the optical light by dust, via the radiation transfer procedure. Since in calculating the emission of the dust we used the absorption efficiencies (Q_{abs}) taken from Laor & Draine (1993), as presented in Sect. 2.1, we compare in Fig. 1 the extinction coefficients derived from the fitting routine with the theoretical ones derived from the extinction efficiencies (Eqs. [2] and [3]). The result of such a

Table 4.1: Parameters of NGC891 derived by Xilouris et al. (1999).

Param.	B	V	I	J	K
L_s $[\frac{erg}{secpc^3ster} \times 10^{27}]$	2.66	3.53	3.44	6.21	1.41
z_s [kpc]	0.43	0.42	0.38	0.43	0.34
h_s [kpc]	5.67	5.48	4.93	3.86	3.87
L_b $[\frac{erg}{secpc^3ster} \times 10^{30}]$	12.0	7.4	2.23	4.99	1.71
R_e [kpc]	1.12	1.51	1.97	0.87	0.86
b/a –	0.60	0.54	0.54	0.71	0.76
τ^f –	0.87	0.79	0.58	0.23	0.10
z_d [kpc]	0.27	0.27	0.27	0.27	0.27
h_d [kpc]	7.97	7.97	7.97	7.97	7.97

comparison shows that indeed the extinction derived from observations (square symbols) is very close to the theoretical one used to calculate the IR emission (solid line). This ensures that the treatment of the absorption and of the emission is consistent. In Fig. 1 we also give the wavelength dependence of the absorption and scattering coefficients, plotted with dashed and dotted lines, respectively.

UV radiation field

The UV radiation field cannot be derived directly from observations. For edge-on galaxies it is extremely difficult to infer something about the young stellar disk, which, due to it's small scaleheight, is presumably highly obscured by line-of sight dust. Any young stellar population whose scaleheight is smaller than the scaleheight of the diffuse dust will be totally unprobed by UV, optical and NIR data on an edge-on galaxy. Thus for an edge-on galaxy mid to far-IR emission would be the primary observational signature for any young massive star population having a scaleheight of 100 pc or less. This stellar population would (we assume luminosity is dominated by stars) produce almost all the non-ionising and ionising UV from the galactic disk.

We thus consider the UV radiation field as a parameter and we parameterise the UV luminosity in terms of a recent SFR, based on the population synthesis models of Mateu & Bruzual (2000). We consider $Z = Z_\odot$, a Salpeter IMF, $M_{up} = 100\,M_\odot$ and $\tau = 5$ Gyr. This gives, for example, SFR $= 8.55 \times 10^{-28}\,L_{UV}$ [erg/s/Hz] for $\lambda = 912$ Å, SFR $= 3.74 \times 10^{-43}\,L_{UV}$ [erg/s] for the integrated ionising UV shortwards of 912 Å, SFR $= 1.18 \times 10^{-28}\,L_{UV}$ [erg/s/Hz] at $\lambda = 1500$ Å, etc. The diffuse UV radiation derived from the calibration above was confined in a thin disk, with a scaleheight $z = 90$ pc (close to that of the Milky Way, Mihalas & Binney 1981) and the same scalelength as the blue disk.

The UV luminosity could, in principle, also be indirectly inferred from different indicators of the SFR, like the free-free emission or Hα emission. There are however large uncertainties in deriving these quantities, especially in the case of NGC891. The first indicator, the radio free-free emission, has the advantage of being optically thin. Niklas et al. (1997) found that the total radio emission of NGC891 is dominated by synchrotron emission, while the free-free emission constitutes a thermal fraction of just 0.05 at an observing

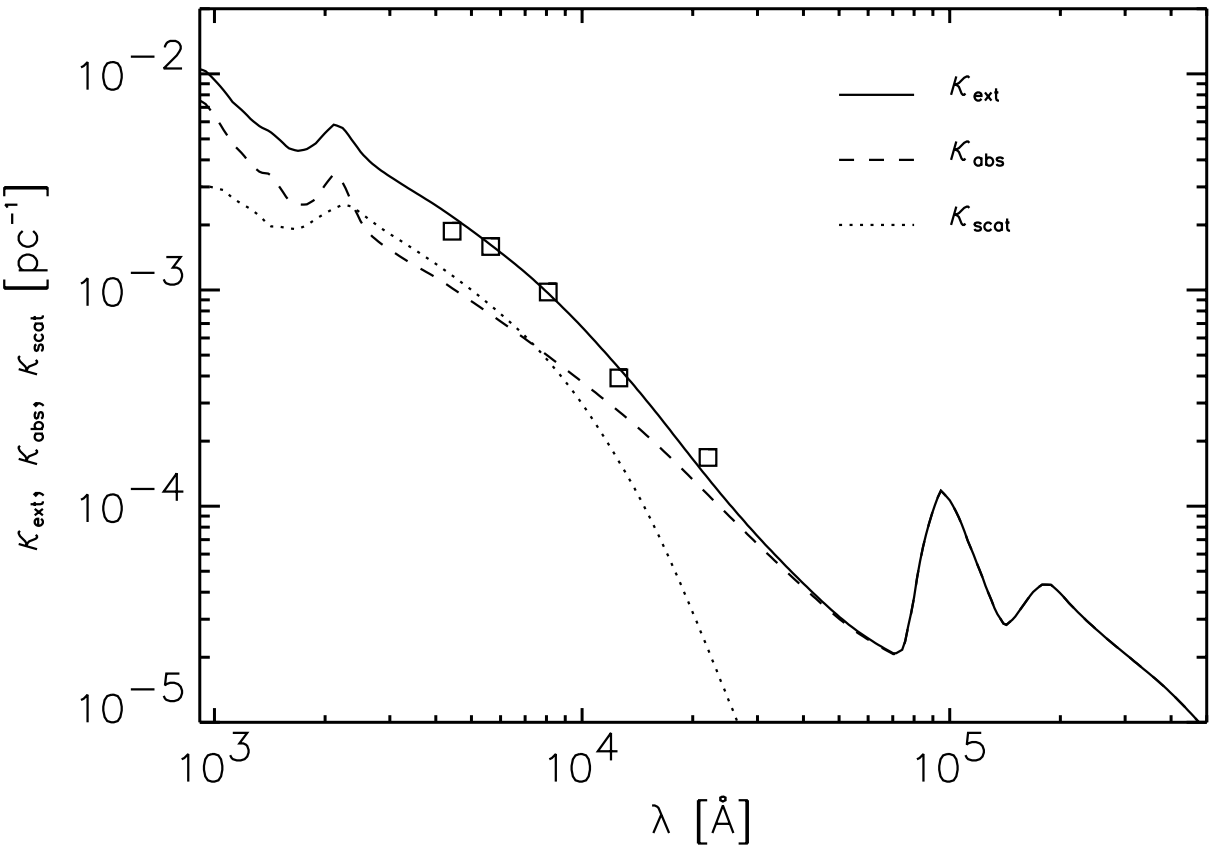

Figure 4.1: The wavelength dependence of the extinction (solid line), absorption (dashed line) and scattering (dotted line) coefficients derived from the extinction, absorption and scattering efficiencies taken from Laor & Draine (1993). The symbols represent the extinction coefficients derived as fitting parameters by Xilouris et al. (1999).

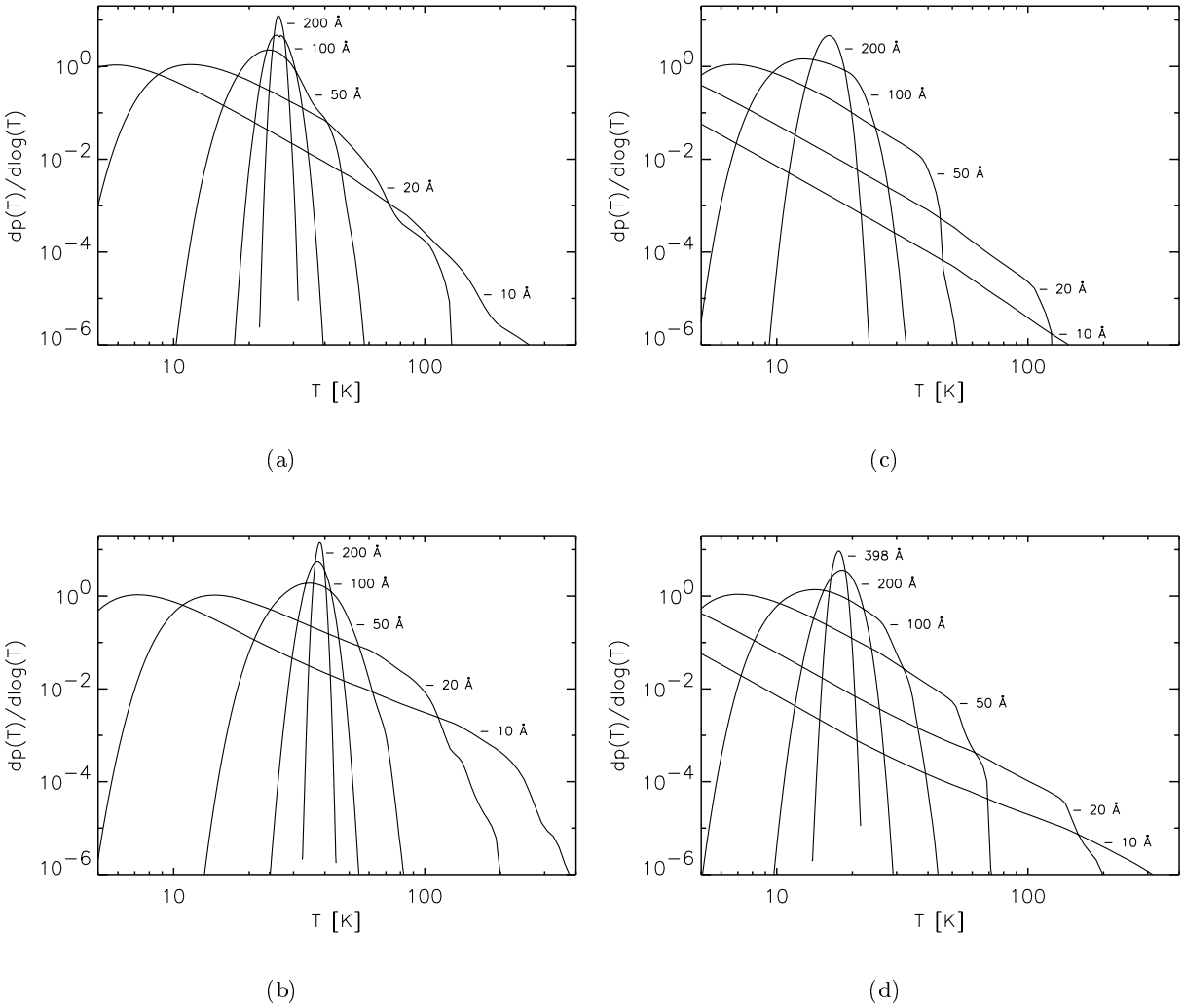

Figure 4.2: Examples of temperature distribution for dust grain sizes (10 Å, 20 Å, 50 Å, ...) embedded in the diffuse radiation field, for a solution with the UV radiation field in the diffuse component corresponding to a SFR $= 3\,\mathrm{M}_\odot$/yr: a) silicate grains in the center of the galaxy ($R = 0\,\mathrm{kpc}$, $z = 0\,\mathrm{kpc}$); b) graphite grains in the center of the galaxy; c) silicate grains at the edge of the galactic disk ($R = 15\,\mathrm{kpc}$, $z = 0\,\mathrm{kpc}$); d) graphite grains at the edge of the galactic disk.

frequency of 10 GHz. However, the radio morphology of NGC891 is rather complicated, with more morphological components having different spectral indices. Allen et al. (1978) suggested the existence of two components for the radio continuum emission: a highly flattened thin disk component coinciding with the equatorial plane of the galaxy and a thick disk or halo component (see also Hummel et al. 1991). If this is the case, then the free-free emission estimated from a spectral decomposition of the integrated fluxes of the galaxy (as done by Niklas et al. 1997) could have been seriously underestimated. We conclude that the free-free emission does not constitute an accurate constraint of our model.

The second indicator of the SFR is the Hα emission. It is known that correcting Hα data for internal extinction is a very uncertain step, since the extinction contains a large-scale component plus extinction due to localised sources, which are difficult to account for in edge-on disks. Hoopes et al. (1999) found that in NGC891, $83-86\%$ of the observed Hα emission is in the diffuse component associated with the halo of the galaxy. This would imply that most of the emission from the disk is highly obscured, making unreliable any derivation of the SFR in the disk.

4.2.3 Calculation of the IR spectrum from grains embedded in the diffuse optical and UV radiation field

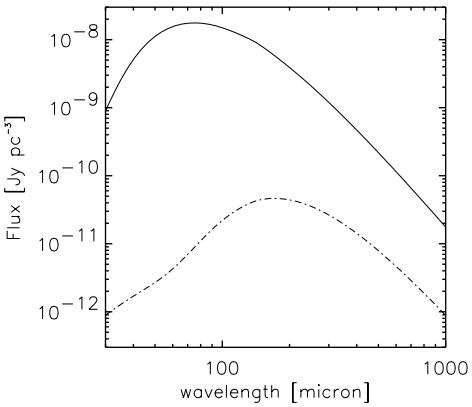

Figure 4.3: The infrared spectrum from dust embedded in the diffuse radiation field, for a solution with the UV radiation field in the diffuse component corresponding to a SFR $= 3\,\mathrm{M}_\odot/\mathrm{yr}$. The figure illustrates the infrared spectrum obtained for two extreme locations in the galaxy: in the center of the galaxy ($R = 0\,\mathrm{kpc}$, $z = 0\,\mathrm{kpc}$) - plotted with solid line and at the edge of the galactic disk ($R = 15\,\mathrm{kpc}$, $z = 0\,\mathrm{kpc}$) - plotted with dashed-dotted line.

The dust heating due to photons from the diffuse interstellar radiation field was calculated following the method of Guhathakurta & Draine (1989). This method derives the temperature distribution $P(a, T)$ of various grain radii a as a function of dust temperature T. Due to stochastic heating, small grains undergo significant fluctuations from the equilibrium temperature, while larger grains have narrower probability functions, eventually approaching delta functions. We calculated the temperature distribution at any point

in the galaxy, based on the energy density of the radiation field derived in the previous subsections. The spectral shape of the UV-NIR energy density and its magnitude will obviously determine the shape of the temperature distributions. The grain sizes used in the calculations were chosen between $a_{min} = 10\,\text{Å}$ and $a_{max} = 0.25\,\mu\text{m}$, for a step $\Delta\log a = 0.05$. In Fig. 2 we give the temperature distribution as $\mathrm{d}p/\mathrm{dlog}T$ for some silicate (Fig. 2a,c) and graphite (Fig. 2b,d) grain sizes embedded in the diffuse radiation field, for a solution with the UV radiation field in the diffuse component corresponding to a SFR $= 3\,\mathrm{M}_\odot/\mathrm{yr}$. Fig. 2 also illustrates the dependence of the grain temperature on the position in the disk. We give two examples, for two extreme positions in the plane of the disk: in the center of the disk (Fig. 2a,b) and at the edge of the disk (Fig. 2c,d). At the edge of the disk the probability distribution converges towards lower equilibrium temperatures, as expected due to the decrease in the intensity of the radiation field. We also note the relatively large difference in the equilibrium temperature between $\sim 30\,\mathrm{K}$ for the central region and $\sim 15\,\mathrm{K}$ for the outer disk. This is interesting in the context of the results of Alton et al. (1998) who fitted the SED of NGC891 with 15 and 30 K grey-body components. We discuss this further in Sect. 7, in terms of the geometry and opacity of the disk. We also note that in passing from the centre to the outer regions, progressively bigger grains exhibit stochastic heating, as expected due to the lower energy density of the radiation field. For the same location in the disk, graphite grains undergo larger fluctuations than the silicate grains.

Given the temperature probability function $P(a,T)$, the IR flux is given by

$$\begin{aligned} F_\nu &= \frac{1}{d^2}\int_{a_{\min}}^{a_{\max}} N(a)\,\mathrm{d}a\,\pi\,a^2\,Q_{\mathrm{abs}}(\nu,a) \\ &\quad \times \int_0^\infty B_\nu(T)\,P(a,T)\,\mathrm{d}T \end{aligned} \tag{4.16}$$

where B_ν is the Planck function, $N(a)$ is the grain size distribution given by Eq. (1), and d is the distance to the galaxy.

The IR emission was calculated in each point of the galaxy and then the total emission was obtained by integrating the emission over the galaxy. In Fig. 3 we give two examples of IR spectra for two extreme locations in the plane of the galactic disk, namely in the center of the galaxy ($R = 0\,\mathrm{kpc}$, $z = 0\,\mathrm{kpc}$) and at the edge of the disk ($R = 15\,\mathrm{kpc}$, $z = 0\,\mathrm{kpc}$). At the edge of the disk the infrared emission is colder, as expected due to the decrease in the dust temperature, though the increased importance of stochastic heating in the outer regions tends to flatten the SED on the Wien side.

4.3 Results for the "standard model"

The FIR emission for our "standard model" was calculated for a grid of SFR, and the different solutions were compared with the observations. To extract the FIR luminosity of the galactic dust we integrated the SED of NGC891 between 40 and 1000 μm, with the data taken from Alton et al. (1998). The SED was parameterised by Alton et al. (1998) by a fitting two-temperature greybody curve (with a wavelength dependence of

grain emissivity in the FIR $\beta = 2$) to the observed fluxes from IRAS and SCUBA at 60, 100, 450 and 850 μm. This yielded best-fit "temperatures" of 30 and 15 K to the observed spectrum, and an integrated luminosity between 40 and 1000 μm of 5.81×10^{36} W. This output luminosity can be accommodated in our "standard model" with a solution for a SFR = 7.5 $M_\odot$/yr. The predicted FIR SED from the model is given in Fig. 4a, together with the UV-optical-NIR intrinsic emitted stellar radiation (as would have been observed in the absence of dust). The IRAS and SCUBA data (diamonds) from Alton et al. (1998) are also given for comparison. The inferred SFR is an upper limit, since we assumed that all the non-ionising UV escapes into the diffuse component. Indeed, in the absence of local absorption, all the lines of sight from each source would contribute primary photons to the diffuse interstellar radiation field. In practice, some fraction of the lines of sight - call this fraction F - from each source will be opaque to local absorption, giving rise to discrete IR sources embedded in a diffuse IR emitting disk. Our solution was thus calculated under the extreme assumption that $F = 0$ for the non-ionising UV and $F = 1$ for the ionising UV. While requiring a solution with a large SFR, the predicted SED is slightly warmer than the observed SED at 100 μm. However, the main difficulty of the model is that it underestimates by a factor of 2 to 4 the observed sub-mm fluxes.

4.4 Results for the "standard model" supplemented by localised sources

A more realistic solution is to consider that some fraction F of the non-ionising UV is locally absorbed in star-forming complexes (e.g., HII regions). Such a solution requires two free parameters (F and SFR) and can be accommodated with a lower SFR, due to the higher probability of absorption of the non-ionising UV photons. To include the contribution of HII regions we used a template SED of such forming complexes. We utilised the galactic UC HII region G45.12+0.13, with FIR observations at 60 and 100 μm from the IRAS Point Source Catalog and 1300 μm measurements from Chini et al. (1986). We fitted the observed data with a greybody curve (with a wavelength dependence of grain emissivity in the FIR $\beta = 2$) and used it as a template SED for the compact source component for our modelling. We do not attempt here to include in this template potential cold emission components that might be expected from "parent" molecular clouds in juxstaposition to their "offspring" HII regions.

The best solution was obtained for a SFR = 3.5 $M_\odot$/yr and $F = 0.28$. The predicted FIR SED is given in Fig. 4b, again together with the UV-optical-NIR intrinsic stellar radiation. In Fig. 4b we also give the contribution of the diffuse component (dashed line) and of the HII component (dotted line) to the the total predicted FIR SED (solid line). The integrated emitted luminosity predicted by the model is $L = 4.79 \times 10^{36}$ W, which accounts for 82% of the total observed emitted FIR luminosity. Of this, the diffuse component contributes 46% of the total observed dust luminosity and the localised sources 36%. However, the main difficulty of the model is again that the solution fails to reproduce the observations longwards of 100 μm.

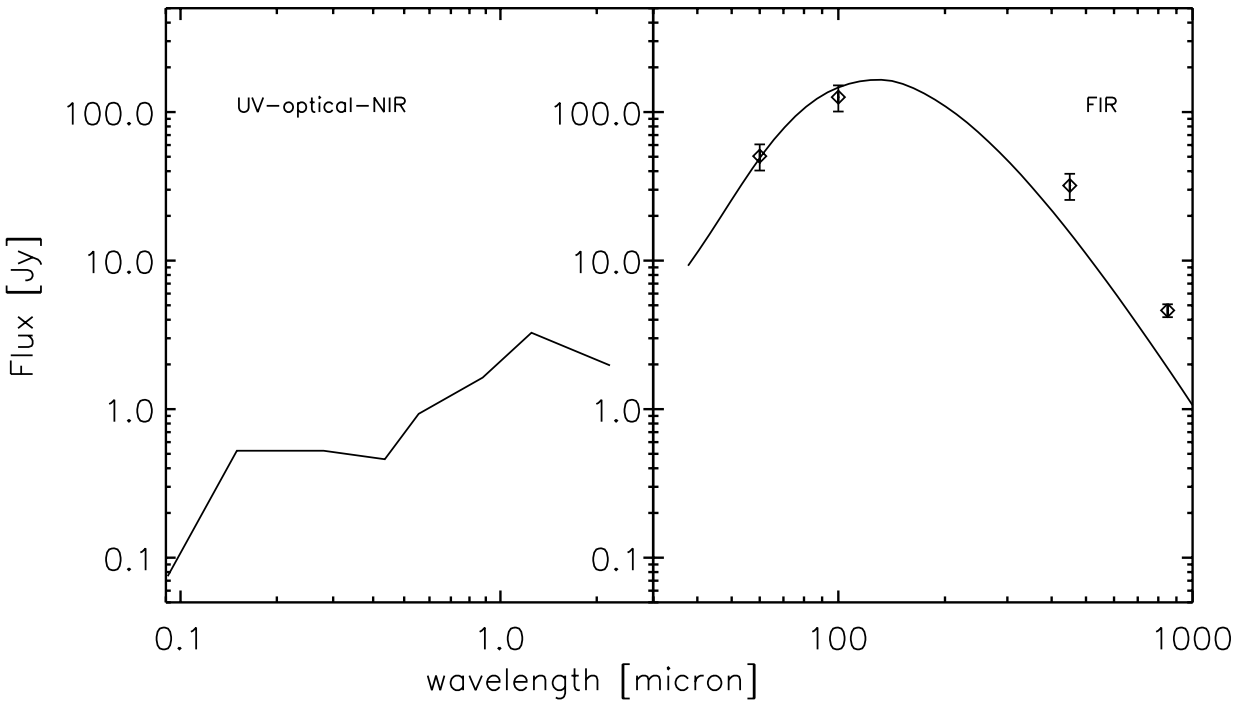

(a)

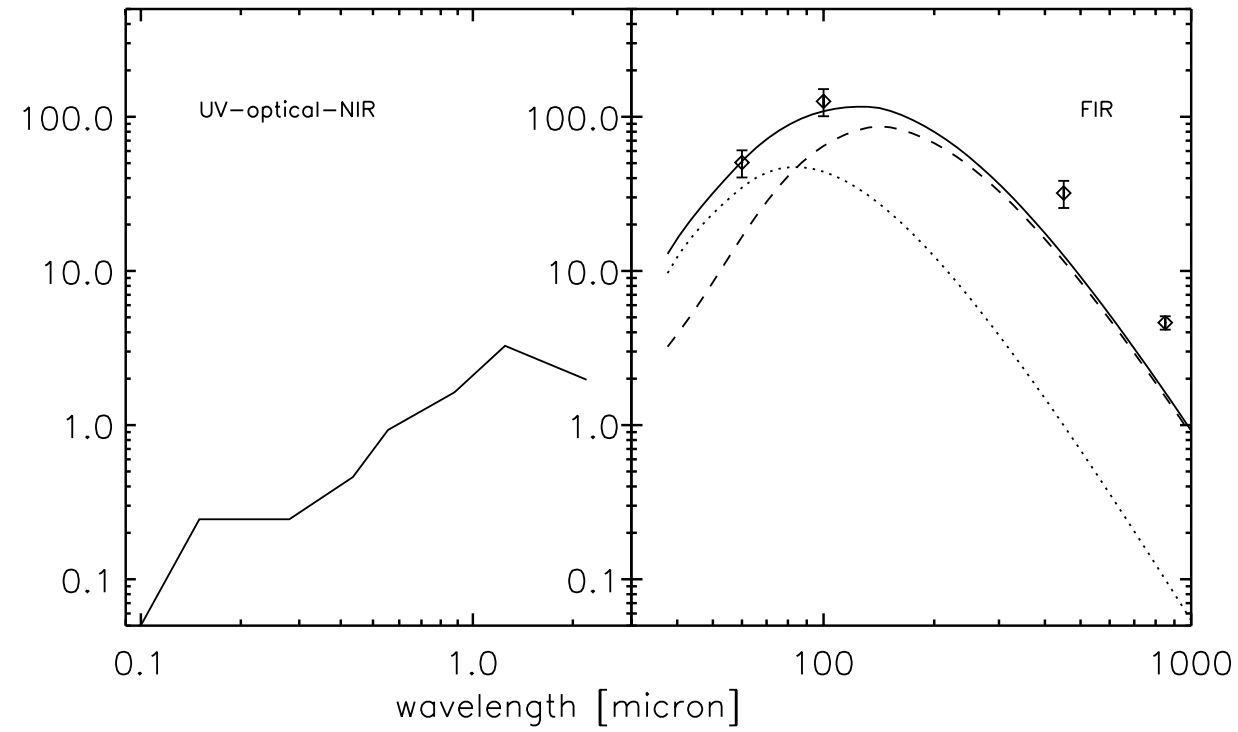

(b)

Figure 4.4: a) The SED from our "standard model", for a current SFR = $7.5\,M_\odot$/yr. The UV-optical-NIR SED plotted in the left hand panel represents the intrinsic emitted stellar radiation (as would have been observed in the absence of dust) while the FIR-sub-mm curve plotted in the right hand panel is the predicted SED for the re-radiated dust emission. The SFR has been adjusted such that the predicted FIR model luminosity equals the observed one. The observed FIR fluxes from Alton et al. (1998) are given as diamonds. b) The SED from our "standard model" supplemented by localised sources,

4.5 The missing FIR/sub-mm component of our "standard model"

We have shown that our "standard model" fails to reproduce the observed SED of NGC891 in the sub-mm spectral range. The more realistic case, where the contribution from HII regions is added to the diffuse component, is also not able to predict the observed FIR/sub-mm SED. However, this may be, to some extent, because we did not include a cold dust emission component that might be expected to arise from associated parent molecular clouds.

Below we consider four more ways that might account for this discrepancy. Firstly, we discuss the effect of altering the geometry of the large-scale distribution of stars and dust. Alternatively, we consider extraplanar emission. Thirdly, the predicted apparent sub-mm/optical ratio could be increased by including more grains in the disk, but distributed in clumps, so as not to effect the optical extinction properties of the diffuse disk. Lastly, a more radical solution is presented, namely a model with two dust-disk components, which is a moderately optically thick solution.

4.5.1 The effect of altering the geometry of the large-scale distribution of stars and dust

The diffuse IR emission predicted by our model was derived for an exponential disk of stars and dust, adopted from Xilouris et al. (1999). Galactic disks are however known to be quite complex systems, where the large-scale distribution of stars and dust presents inhomogeneities in the form of spiral structures. Adding logarithmic spiral arms as a perturbation on the exponential disks for stars and dust would alter the solutions of the radiative transfer, and thus of the calculated diffuse IR emission. However, Misiriotis et al. (2000b) showed that plain exponential disk models give a very accurate description for galactic disks seen edge-on, with only small deviations in parameter values from the real ones (typically a few percent). Thus, we conclude that the geometry adopted here cannot be responsible to account for the discrepancy between our model predictions and the observations.

4.5.2 Extraplanar dust?

Observations of external galaxies have revealed extensive thickened layers of ionised gas traced by its Hα emission in several edge-on spiral galaxies (e.g., Rand et al. 1990, 1992; Dettmar 1990; Pildis et al. 1994; Rand 1996, Ferguson et al. 1996; Hoopes et al. 1999). Amongst the most spectacular examples of extraplanar diffuse ionising gas (DIG) is that seen in NGC891. The recent observations of Hoopes et al. (1999) showed that the DIG layer in NGC891 extends out to at least 5 kpc from the plane, and possibly as far as 7 kpc, and has the brightest and largest DIG layer known.

In addition to detecting the high z DIG studied in earlier work, Howk & Savage (2000) also detected individual dust-bearing clouds observable to heights $z \sim 2\,\mathrm{kpc}$ from the midplane. Moreover, they detected the presence of HII regions at large distances from

the midplane (0.6-2 kpc), which suggests that on-going star formation may be present in some of the dense, high-z clouds.

In principle both the dust-bearing clouds ($z \sim 2$ kpc) seen in absorption as well as the dust that may be associated with the DIG ($z \sim 5$ kpc) could contribute to the FIR/sub-mm emission of the galaxy. The possibility of the extraplanar dust clouds emitting in the sub-mm was recently investigated by Alton et al. (2000b). From the upper limits in the total amount of extraplanar dust these authors found that less than 5% of galactic dust exists outside the galactic disk, if the dust grains are not colder than 17 K, or 9%, if the dust temperature is 10 K. This small percentage cannot account for our discrepancy between the model and the observations.

We also consider it unlikely that any diffuse dust component associated with the DIG ($z \sim 5$ kpc) could provide a substantial fraction of the sub-mm emission. In that case, if the extraplanar emission were powered by the absorption of disk photons, the optical depth of the DIG would have to be comparable to that of the disk, which would be a very extreme scenario, probably also in conflict with the constraints on submillimeter extraplanar emission.

4.5.3 The case of hidden dust in clumps

One possible explanation to account for the missing dust component could be that Xilouris et al. (1999) underestimated the dust content of the galaxy because of the adopted diffuse distribution for the dust. Since the galaxy is optically thin, any additional dust component would have to be distributed in very dense clumps instead of being diffuse. Only then would a significant fraction of the lines of sight avoid the additional dust, so as not to affect the derived optical-NIR optical depth.

Such dust clumps could either be a component of star-formation regions, or could have no associated sources - we refer to the latter hypothesis as the "quiescent clumps". The quiescent clumps must be optically thick to the diffuse UV/optical radiation field in the disk to have an impact on the predicted submillimeter emission. They would radiate at predominantly longer wavelengths than the diffuse disk emission, in the FIR/sub-mm spectral range. One can speculate that such optically thick "quiescent clouds" could be physically identified with partially or wholly collapsed clouds that, for lack of a trigger, have not (yet) begun to form stars. However, due to the lack of intrinsic sources, a very substantial mass of dust would have to be associated with the quiescent clouds to account for the submillimeter emission missing from our model prediction.

In reality there must be also dark clouds associated with star-forming complexes. In the Milky Way HII regions around newly born massive stars are commonly seen in juxtaposition to parent molecular clouds (e.g., M17). This is thought to be a consequence of the fragmentation of the clouds due to mechanical energy input from the winds of the massive stars. Thus, warm dust emission from cloud surfaces directly illuminated by massive stars can be seen along a fraction of the lines of sight, together with cold sub-mm dust emission from the interior of the associated optically thick cloud fragments. These dense clumps (with or without associated sources) may contribute to the sub-mm emission, and thus supplement the contribution of compact HII regions.

However, the question remains whether it is possible to place such a substantial amount

of additional dust in clumps without affecting the opacity of the galaxy. Kuhinski et al. (1998) modeled a sample of highly inclined galaxies using both smooth and clumpy dust and concluded that clumpiness does not effect dramatically the opacity of highly inclined galaxies. On the other hand, Bianchi et al. (1999) adopt different parameterisation for clumps and they report that clumpiness does significantly effect the opacity of edge-on galaxies. It is beyond the scope of this paper to calculate a quantitative solution for a clumpy distribution, but we qualitatively consider the clumpy scenario, as quiescent clumps or associated with star-formation regions - to be a possibility to account for the missing FIR-sub-mm component.

4.5.4 A two-dust-disk model

We have seen that the observed sub-mm SED requires more dust in the galaxy than predicted by our "standard model". We have already discussed the possibility of including this extra dust in clumps. An alternative solution is obtained if it is postulated that this additional dust is confined in a diffuse thin disk, in which the young stellar population is embedded. (A thin young stellar disk, but with no associated dust, was considered in Xilouris et al. 1998.) If this second dust-disk component has a scaleheight comparable with the 90 pc scaleheight of molecular gas clouds in the Milky Way, it would not have been seen in the optical/NIR analysis of Xilouris et al. (1999), being totally obscured by the optically visible disk of dust. Indeed, since the galaxy is almost edge-on, adding a second thin disk of dust will probably not change the parameters for the intrinsic distributions of stars and dust derived by Xilouris et al. (1999). However, adding a second disk of dust will change the optical depth of the disk, transforming our solution into a moderately optically thick solution ($\tau_V^f = 3.1$).

We have calculated the energy density of the radiation field from UV to NIR for such a two-dust-disk model, and subsequently the infrared emission. The best solution was obtained for a SFR $= 3.8\,\mathrm{M}_\odot/\mathrm{yr}$, $F = 0.22$ and $M_{dust} = 7 \times 10^7\,\mathrm{M}_\odot$ in the second disk of dust. The corresponding non-ionising UV luminosity for this SFR is $\sim 8.2 \times 10^{36}\,\mathrm{W}$. This could be provided, for example, by a population of B5 stars ($T_{\rm eff} = 15500\,\mathrm{K}$) with a space density in the centre of the galaxy of $7.5 \times 10^{-4}\,\mathrm{pc}^{-3}$. The predicted combined SED from the two diffuse dust-disk components is shown by the dashed line in Fig. 5. By adding the further contribution from localised sources (dotted line), as discussed in Sect. 4, we were able to fit the SED of NGC891, from the FIR to the sub-mm. The luminosity of the diffuse component is $4.07 \times 10^{36}\,\mathrm{W}$, which accounts for 69% of the observed FIR luminosity, and the luminosity of the HII component is $1.82 \times 10^{36}\,\mathrm{W}$, making up the remaining 31% of the FIR luminosity. This model can thus successfully fit the shape of the SED. In the next section we will show that the predictions of the two-dust-disk model are in agreement with the observed radial profile at $850\,\mu$m. Nevertheless, further modelling of face-on galaxies will be required to test the validity of the two-dust-disk model. Ultimately, the two-dust-disk hypothesis will be directly tested observationally using the new generation of sub-mm interferometers, which will resolve edge-on disks.

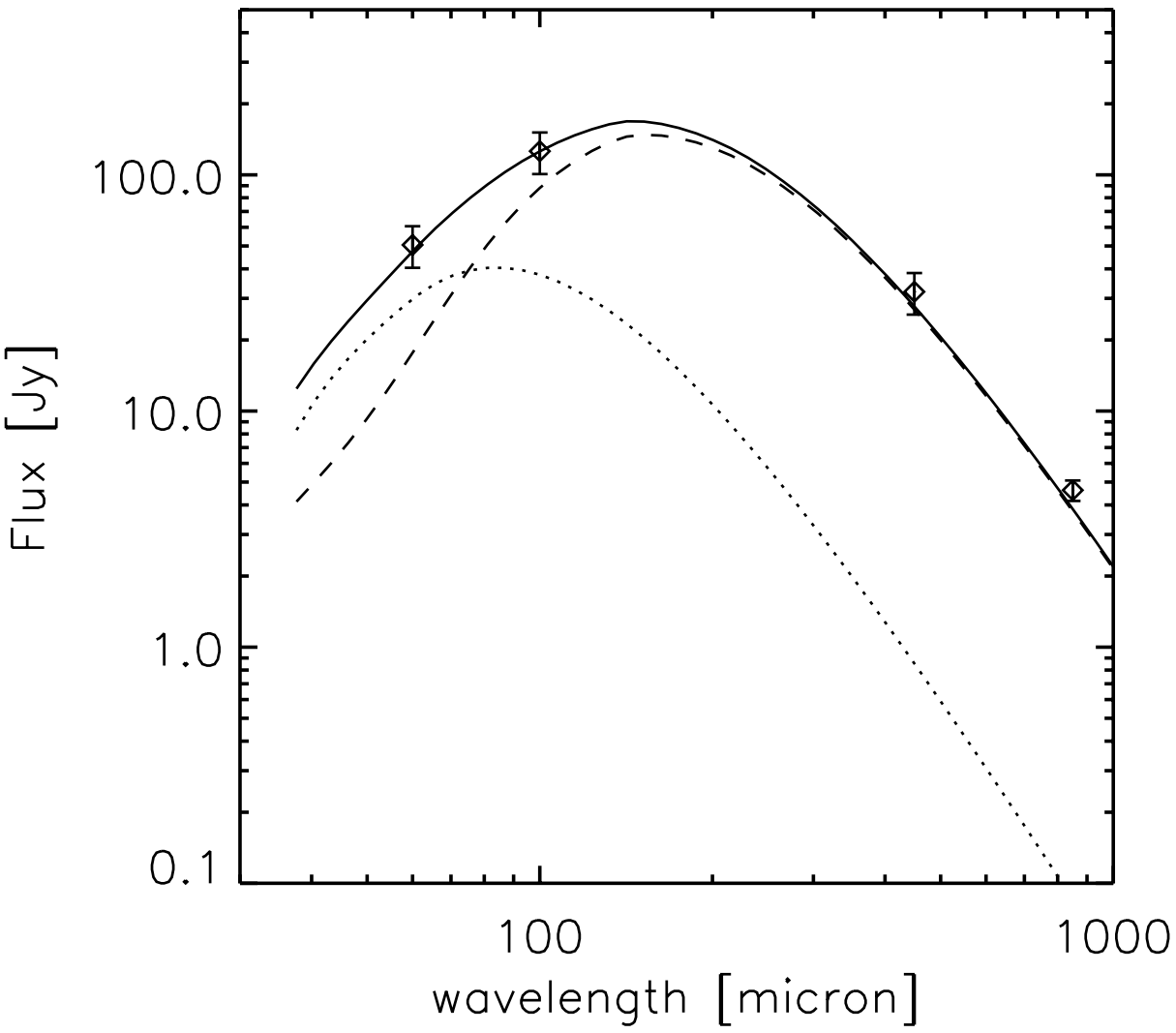

Figure 4.5: The predicted FIR emission from a two-dust-disk model, for a SFR = $3.8\,M_\odot$/yr and $F = 0.22$. The total predicted SED is given with solid line, the diffuse component with dashed line and the HII component with dotted line. The observed fluxes from Alton et al. (1998) are given as diamonds.

4.6 The radial profiles

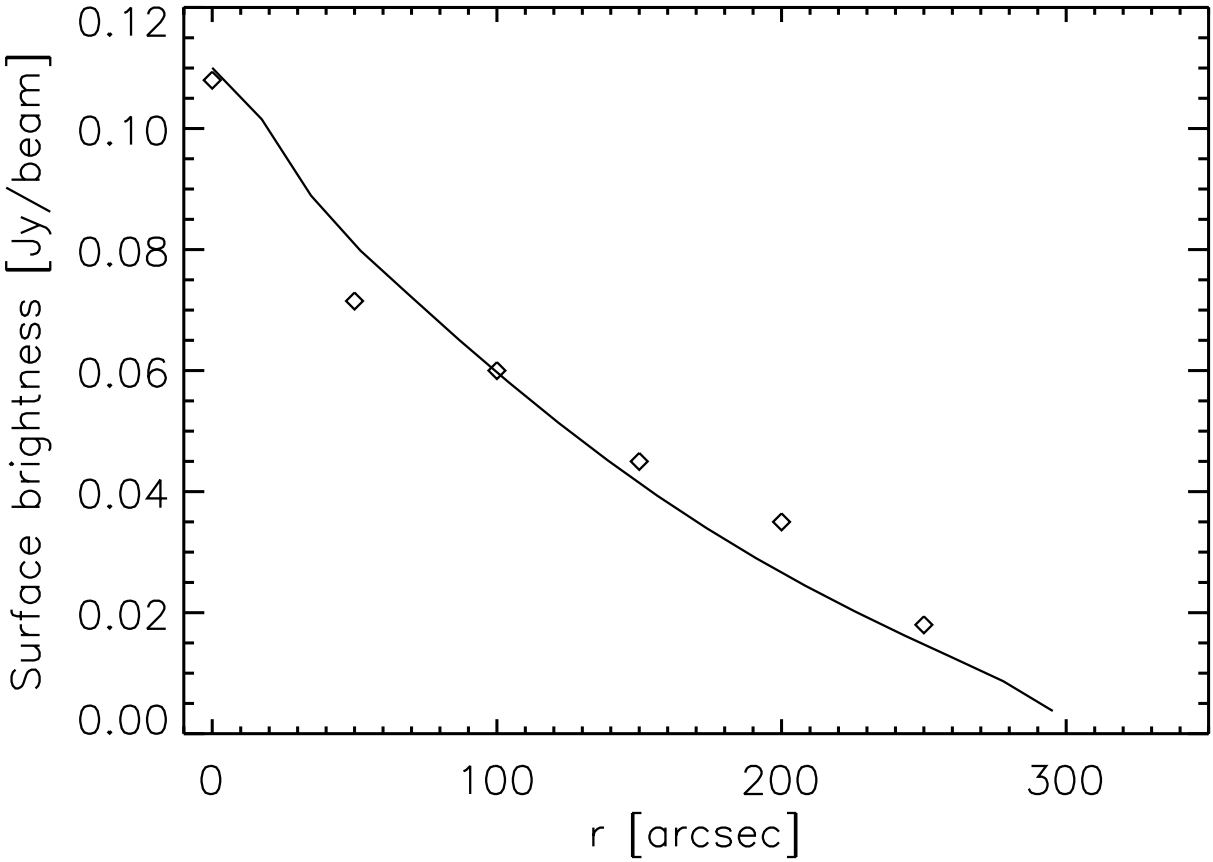

Figure 4.6: The averaged radial profile at 850 μm from the two-dust-disk model, plotted with the solid line. The profile is averaged over a bin width of 36″, for a sampling of 3″ and for a beam width of 16″, in the same way as the observed averaged radial profile from Alton et al. (2000a) (plotted with diamonds).

Since we have calculated the 3 dimensional FIR radiation field in NGC891, for both our "standard model" and the two-dust-disk model, it is straightforward to integrate along the line of sight and thus produce a 2-dimensional map of the galaxy at different wavelengths, and then radial profiles. Here we consider only the diffuse component of the IR emission. Because observed radial profiles were derived by Alton et al. (2000a) using the SCUBA observations at 850 μm, we first attempt to calculate the radial profiles at this wavelength and compare it with the observations. The calculations were done at high resolution and afterwards smoothed to 16″ resolution. Since the observed radial profile at 850 μm from Alton et al. (2000a) were derived as averages over a bin width of 36″, and with a sampling of 3″, we have also calculated an averaged radial profile in the same way as Alton et al. (2000a) did, and directly compare it with the observations. We have found that in the case of the two dust disk model there is a very good agreement between the model predictions and the observations and this comparison is illustrated in Fig. 6. The predicted radial profile can be traced out to 300 arcsec radius (15 kpc), as also detected

by the SCUBA.

In Figs. 7a and 7c we give our prediction for the radial profile of NGC891 at 850 μm, this time as it would be observed within a beam of $16''$, and without any averaging. This is shown for our "standard model" and the two-dust-disk model, respectively. In Fig. 7b.d we give the radial colour profiles at the wavelengths used by the IRAS, ISO and SCUBA, normalised to the radial profile at 850 μm. The strong colour gradients, seen in particular between the 60 or 100 μm and the sub-mm regime, are a consequence of the strong gradients in the radiation field calculated in our finite disk model. It is interesting to note that the stronger contribution of stochastic emission from small grains (relative to big grains) in the outer disk at 60 μm, does not strongly influence the gradients. Potentially, therefore, large-scale colour gradients in galaxy disks, could act as a diagnostic for the relative contribution of the diffuse emission and compact sources, as the latter would not be expected to have IR spectra strongly dependent on position in the disk. As expected, the 450/850 colour shows only a shallow gradient, as both these wavelengths are displaced well longwards of the spectral peak, and thus depend only approximately linearly on grain temperature.

4.7 Discussion: the contribution of different stellar populations in heating the dust in NGC891

The relative contribution of optical and UV photons in heating the dust has been a long standing question in the literature. Since we have a detailed calculation of the absorbed energy over the whole spectral range and at each position in the galaxy, we can directly calculate which part of the emitted FIR luminosity from each volume element of the galaxy is due to the optical and NIR photons, and which part is due to the UV photons. The IR emission from any given volume element arises from a common local grain population, so that the IR colours from that volume element will be the same for the emitted IR photons regardless of whether the absorbed energy had an optical or UV origin. However the relative fraction of energy absorbed from the UV and optical light varies with position in the galaxy, as does the dust temperature, so that the volume-integrated IR spectrum representing re-radiated optical light will differ from that of the re-radiated UV light. In this way, some information on the stellar populations heating the grains is preserved in the IR domain, in the form of the observed IR colours. Volume-integrated IR spectral components arising from re-radiated optical and UV light are presented in Fig. 8a,b for the "standard model" and in Fig. 8c,d for the two-dust-disk model, respectively. The overall contribution of the diffuse optical and NIR radiation ($4000 - 22000\,$Å) to the total FIR luminosity is $1.07 \times 10^{36}\,$W, or 22% for the "standard model". Since the predicted luminosity of this model is lower than the observed one, it is also meaningful to give the contribution of the diffuse optical radiation to the observed FIR luminosity, which is 18%. This component of the FIR SED is plotted with dashed line in Fig. 8a,b. The corresponding optically generated IR luminosity for the two-dust-disk model is $1.85 \times 10^{36}\,$W, or 31%, higher than in the "standard model", largely because the galaxy is becoming optically thick in the optical range. This component of the FIR SED is again plotted with dashed-line in Fig. 8c,d. The contribution of different stellar components to

Table 4.2: The contribution of the diffuse optical/NIR radiation L_{FIR}^{opt} ($4000 - 22000$ Å), diffuse UV radiation L_{FIR}^{UV} ($912 - 4000$ Å) and UV photons locally absorbed in HII regions L_{FIR}^{HII} to the total predicted FIR luminosity L_{FIR}^{model}.

	standard model SFR $= 3.5\,M_\odot$/yr $F = 0.28$	two-dust-disk model SFR $= 3.8\,M_\odot$/yr $F = 0.22$
L_{FIR}^{opt}	1.07×10^{36} W $22\%\, L_{FIR}^{model}$	1.85×10^{36} W $31\%\, L_{FIR}^{model}$
L_{FIR}^{UV}	1.60×10^{36} W $33\%\, L_{FIR}^{model}$	2.22×10^{36} W $38\%\, L_{FIR}^{model}$
L_{FIR}^{HII}	2.12×10^{36} W $44\%\, L_{FIR}^{model}$	1.82×10^{36} W $31\%\, L_{FIR}^{model}$
L_{FIR}^{model}	4.79×10^{36} W	5.89×10^{36} W
$L_{FIR}^{observed}$	5.81×10^{36} W	5.81×10^{36} W

the total FIR luminosity for the two dust models is summarised in Table 2. Table 3 gives the contribution of different stellar components to the FIR wavelength commonly used by IRAS, ISO and SCUBA.

We note that, regardless of the optical thickness of the adopted model, the diffuse optical radiation field makes only a relatively small contribution to the total emitted dust luminosity. This is in qualitative agreement with various statistical inferences linking FIR emission with young stellar populations, in particular the FIR-radio correlation which, also after normalisation to indicators of galactic mass, such as K-band flux, remains rather tight (Xu et al. 1994). Perhaps more surprising, at first glance, is the predicted predominance of UV-powered grain emission in the sub-mm range in both our dust models (Fig. 8b,d.). However, our analysis has demonstrated that the FIR colours have to be fundamentally interpreted also in geometrical terms, rather than simply as separate temperature components. Thus, the predicted increasing predominance of re-radiated diffuse UV photons over re-radiated diffuse optical photons going from the FIR into the sub-mm regime is due to an increasing fraction of the emission arising from more optically thin regions, where the ratio of optical to UV absorption is largely controlled by the relative optical and UV grain emissivities. This particularly applies in the the outer disk, which, in addition to being (relative to the inner disk) optically thin, has systematically lower grain heating and temperature.

Table 4.3: The relative contribution of the diffuse optical/NIR radiation f_{FIR}^{opt} (4000 − 22000 Å), diffuse UV radiation f_{FIR}^{UV} (912 − 4000 Å) and UV photons locally absorbed in HII regions f_{FIR}^{HII} to various FIR wavelengths. The wavelengths considered here were those commonly used by IRAS, ISO and SCUBA, namely 60, 100, 170, 450, and 850 μm.

	standard model SFR = 3.5 $M_\odot$/yr $F = 0.28$			two-dust-disk model SFR = 3.8 $M_\odot$/yr $F = 0.22$		
λ μm	f_{FIR}^{opt}	f_{FIR}^{UV}	f_{FIR}^{HII}	f_{FIR}^{opt}	f_{FIR}^{UV}	f_{FIR}^{HII}
60	0.15	0.19	0.67	0.20	0.19	0.62
100	0.24	0.35	0.41	0.33	0.37	0.30
170	0.30	0.50	0.20	0.39	0.50	0.11
450	0.33	0.60	0.08	0.39	0.58	0.03
850	0.33	0.61	0.06	0.39	0.59	0.02

4.8 Summary and Conclusions

In this paper we have modeled the edge-on spiral galaxy NGC891 from the UV to the FIR and sub-mm with the purpose of understanding what is the origin of the FIR/sub-mm emission. The strategy of the paper was to use a model for the intrinsic distribution of older stars and associated dust as derived from fitting the optical and NIR images of NGC891 by Xilouris et al. (1999), which, supplemented by a distribution of newly-form stars, should predict the diffuse FIR emission. By comparing the prediction of the "standard model" with the observations we tried to identify whether this model can reproduce the observed dust emission.

To calculate the FIR emission in the galaxy we needed to have a dust model and also the energy density of the radiation field at each position in the galaxy. In describing the properties of the grains we used the extinction efficiencies from Laor & Draine (1993) for spherical "astronomical grains", for a mixture of graphites and silicates of the MRN grain size distribution. For small grains not in equilibrium with the radiation it was necessary to model the stochastic emission. For this calculation we adopted the heat capacities from Guhathakurta & Draine (1989) for silicate grains and from Dwek (1986) for graphite grains. Our theoretical dust model was found to be consistent with the extinction coefficients in the optical and NIR spectral range, derived independently by Xilouris et al. (1999) for NGC891. The similarity between the extinction coefficients derived from our theoretical model and those derived as fitting parameters assure us that we can use the model for the distribution of old stars and associated dust of Xilouris et al. (1999).

The calculation of the energy density in the galaxy was done using the solution of the radiation transfer equation, based on the method of Kylafis & Bahcall (1987). This

calculation was done separately for the optical/NIR and UV radiation field. For the distribution of old and intermediate age stars we used a smooth exponential disk and a de Vaucouleurs bulge, with the parameters derived from Xilouris et al. (1999). For the distribution of newly-formed stars we used a smooth exponential disk, with fixed parameters, e.g., with the same scalelengths as that of the stars radiating in the B band, and with a scaleheight of 90 pc. The amplitude of the radiation emitted by the young stars (of the ionising and non-ionising UV radiation) was considered as a free parameter. Using the population synthesis models of Mateu & Bruzual (2000) we parameterised the UV radiation in terms of the recent SFR. Another free parameter was the fraction F between the UV photons which are locally absorbed within star-forming complexes and those which participate in the diffuse ISRF.

The predicted SED from our "standard model" was compared with the observed one. In the extreme case that $F = 0$, the SFR can be taken so as to exactly reproduce the total bolometric output in infrared. This is a solution with SFR $= 7.5\,\mathrm{M}_{\odot}$/yr. While requiring a high SFR, this solution fails to reproduce the sub-mm part of the spectrum. A solution with $F > 0$, which includes also the contribution of star-forming complexes, underestimates even more the emission in the sub-mm spectral range. The failure of our "standard model" to fit the observed SED of NGC891 indicates, most probably, that there is missing dust, which could not have been detected by Xilouris et al. (1999). Two scenarios are proposed to explain this missing dust component, namely a scenario in which the missing dust is in the form of very small optically thick clumps, such that they do not affect the optical extinction derived by Xilouris et al. (1999), or in the form of a second diffuse thin disk, where the young stellar population is embedded. For the second case we give a quantitative description of the model, and we make calculations for the FIR output. We have found that the two-dust-disk model reproduces very well the observed SED, as well as the radial profile at 850 μm. This solution requires a SFR $= 3.5\,\mathrm{M}_{\odot}$/yr and $F = 0.28$. This value of the SFR fits better with the preconception that NGC891 is a relatively quiescent normal galaxy.

Potentially, a further possibility exists to explain the shortfall in sub-mm emission predicted by our "standard model". A higher level of sub-mm emission could be attained from a given grain mass if the sub-mm grain emissivity were higher than assumed in our dust model. This approach was followed by Alton et al. (2000a). However, for a given grain heating the sub-mm/FIR colour of the grain emission will become colder, in order to preserve the energy balance between the absorbed UV/optical and the radiated emission. Thus, the peak of the SED would be shifted to longer wavelengths, so in this scenario there would be a need to increase the SFR to account for the observed fluxes in the 60-100 μm range.

We emphasise that, on the basis of currently available observational evidence, it is difficult to distinguish between the two dust-disk-model and the clumpy scenario. As present day sub-mm and FIR telescopes generally have insufficient angular resolution to resolve the postulated geometrical emission components, the best way of distinguishing between them might be to compare the statistics of quantities derived from the UV/optical/FIR/sub-mm SEDs. Such statistics could be, for example, the derived star-formation rates from a sample of edge-on and face-on systems with comparable morphological types. With the advent of the future generations of FIR telescopes with arcsec

resolution we will be able to directly distinguish between diffuse disk and cloud scenarios. Then such techniques will be needed to understand young galaxies at cosmological distances.

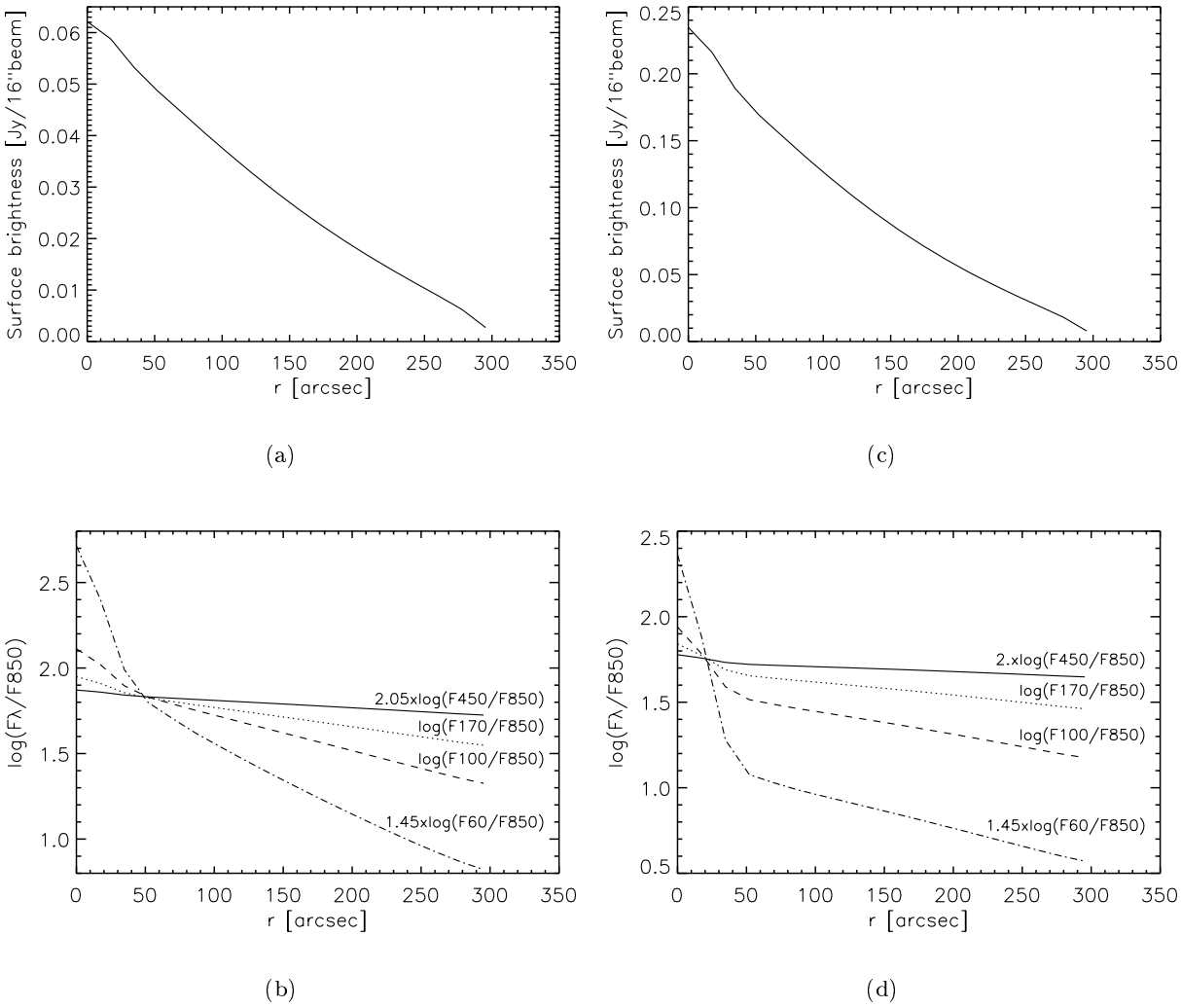

Figure 4.7: a) The predicted diffuse FIR radial profile from our "standard model" at 850 μm, for SFR $= 3.5\,M_{\odot}$/yr. The radial distance is given in arcsec, with $100'' \sim 5\,$kpc). b) The predicted colour profiles at different wavelengths, for the same model like in a). The ratios were multiplied by the given factors to provide the same colours at an angular radius of $50''$. The colour profiles show that for shorter wavelengths the effect of decreasing the dust temperature towards larger radii become more and more pronounced. The colour profile F60/F850 has the steepest gradient, with a very hot component within the inner 50 arcsec radius, followed by the increase of the cold dust at the larger galactocentric distances. c) The predicted diffuse FIR radial profile from our two-dust-disk model, at 850 μm, for SFR $= 3.8\,M_{\odot}$/yr. d) The colour profiles for the two-dust-disk model. Again, the ratios were multiplied by the given factors to provide the same colours at an angular radius of $20''$.

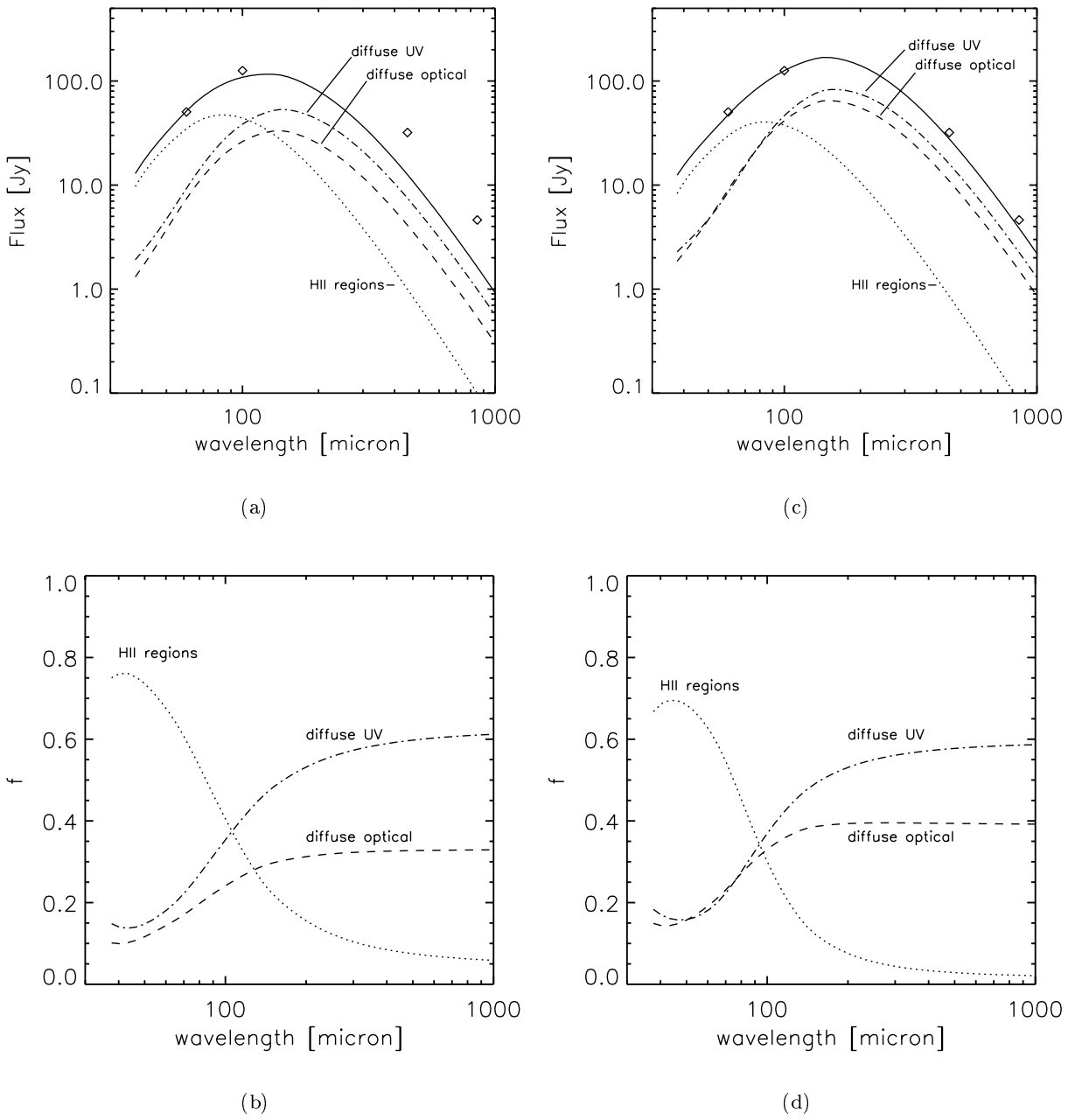

Figure 4.8: a) The contribution of different stellar components to the FIR emission, as a function of wavelength, for our "standard model". The legend is as follows: dashed-line: contribution of diffuse optical radiation ($4000-22000$ Å), dashed-dotted line: contribution of diffuse UV radiation ($912-4000$ Å), dotted-line: contribution of HII component, solid line: total predicted FIR SED. The observed fluxes from Alton et al. (1998) are given as diamonds. b) The same as in case a), but here the different contributions are given as the fraction f of the FIR emission produced by a certain component to the total FIR predicted emission. c) and d) are the same as a) and b), respectively, but for the two-dust-disk model.

Bibliography

Allen R.J., Baldwin J.E., Sancisi R., 1978, A&A 62, 397

Alton P.B., Bianchi S., Rand R.J., et al., 1998, ApJ 507, L125

Alton P.B., Xilouris E.M., Bianchi S., et al., 2000a, A&A 356, 795

Alton P.B., Rand R.J., Xilouris E.M., et al. 2000b, A&A in preparation

Bianchi S., Davies J.I., Alton P.B., 1999, A&A 344, L1

Christensen H. J., 1990, MNRAS 246, 535

Chini R., Kreysa E, Mezger P.G., Gemund H.-P, 1986, A&A 154, L8

Cox P.N., Krügel E., Mezger P.G., 1986, A&A 155, 380

de Jong T., Clegg P.E., Rowan-Robinson M., et al., 1984, ApJ 278, L67

Désert F.-X, Boulanger F., Puget J.L., 1990, A&A 237, 215

Dettmar R.-J., 1990, A&A 232, L15

Devereux N.A., Young J.S., 1990, ApJ 350, L25

Devriendt J.E.G., Guiderdoni B., Sadat R., 1999, A&A 350, 381

Draine B.T., Lee H.M., 1984, ApJ 285, 89

Draine B.T., Anderson N., 1985, ApJ 292, 494

Dumke M., Krause M., Wielebinski R., Klein U., 1995, A&A 302, 691

Dwek E., 1986, ApJ 302, 363

Ferguson A.M.N., Wyse R.F.G., Gallagher J.S., 1996, AJ 112, 2567

Guhathakurta P., Draine B.T., 1989, ApJ 345, 230

Henyey L. G., 1937, ApJ 85, 107

Henyey L. G., Greenstein J. L., 1941, ApJ 93, 70

Hoopes C.G., Walterbos R.A.M., Rand R.J., 1999, ApJ 522, 669

Howk J.C., Savage, B.D., 2000, AJ, in press

Hummel E., Dahlem E., van der Hulst J.M., Sukumar S., 1991, A&A 246, 10

Kuchinski L. E., Terndrup D. M., Gordon K. D., Witt A.N., 1998, AJ 115, 1438

Kylafis N. D., Bahcall J.N., 1987, ApJ 317, 637

Laor A., Draine B.T., 1993, ApJ 402, 441

Leger A., Jura M., Omont A., 1985, A&A 144, 147

Mateu J., Bruzual G., 2000 in preparation

Mathis J.S., Rumpl W., Nordsieck K.H. 1977, ApJ 217, 425

Mezger P.G., Mathis J.S., Panagia N., 1982, A&A 105, 372

Mihalas, D. 1978, Stellar Atmospheres (San Francisco: Freeman)

Mihalas D., Binney J., 1981, Galactic astronomy: Structure and kinematics (San Francisco, CA, W. H. Freeman and Co.)

Misiriots A., Kylafis N. D., Papamastorakis J., Xilouris E. M., 2000b, A&A, 353, 117

Misiriotis A., Popescu C.C., Kylafis N.D., Tuffs R.J., 2000a, A&A in preparation

Niklas S., Klein U., Wielebinski, R. 1997, A&A 322, 19

Ohta K., Kodaira K., 1995 PASJ 47, 17

Pildis R.A., Bregman J.N., Schombert J.M., 1994, ApJ 427, 160

Rand R.J., 1996, ApJ 462, 712

Rand R.J., Kulkarni S.R., Hester J.J., 1990, ApJ 352, 1

Rand R.J., Kulkarni S.R., Hester J.J., 1992, ApJ 396, 97

Silva L., Granato G. L., Bressan A., Danese L., 1998, ApJ 509, 103

van der Kruit P.C., Searle L., 1981, A&A 95, 116

Walterbos R.A., Schwering P.B.W., 1987, A&A 180, 27

Xilouris E. M., Kylafis N. D., Papamastorakis J., Paleologou E. V., Haerendel G. 1997, A&A 325, 135

Xilouris E. M., Alton P. B., Davies J. I., et al., 1998, A&A 331, 894

Xilouris E. M.,Byun Y.I., Kylafis N. D., Paleologou E. V., Papamastorakis J., 1999, A&A 344, 868

Xu C., Lisenfeld U., Völk H.J., 1994, A&A 285, 19

Chapter 5

Modeling the spectral energy distribution of galaxies. II. Disk opacity and star formation in 5 edge-on spirals

Using tools previously described and applied to the prototype galaxy NGC 891, we model the optical to far-infrared spectral energy distributions (SED) of four additional edge-on spiral galaxies, namely NGC 5907, NGC 4013, UGC 1082 and UGC 2048. Comparing the model predictions with IRAS and, where available, sub-millimeter and millimeter observations, we determine the respective roles of the old and young stellar populations in grain heating. In all cases, the young population dominates, with the contribution of the old stellar population being at most 40%, as previously found for NGC 891. After normalization to the disk area, the massive star-formation rate (SFR) derived using our SED modeling technique, which is primarily sensitive to the non-ionizing ultraviolet output from the young stellar population, lies in the range $7 \times 10^{-4} - 2 \times 10^{-2}\,\mathrm{M_\odot yr^{-1}kpc^{-2}}$. This is consistent with normalized SFRs derived for face-on galaxies of comparable surface gas densities from H_α observations. Though the most active star-forming galaxy of the five in absolute terms, NGC 891 is not an exceptional system in terms of its surface density in SFR.

5.1 Introduction

Optical and Far-Infrared (FIR)/sub-millimeter (submm) data from galaxies contain complementary information about the distribution of stars and dust, from which intrinsic quantities of interest - the star-formation rate (SFR) and star-formation history - can in principle be extracted. This is especially relevant to systems having intermediate optical depths to starlight, or to inhomogeneous systems with optically thin and thick components. Many, perhaps most, of normal (non-starburst) gas-rich galaxies in the local universe may fall into these categories.

On the one hand, optical data probes the colour and spatial distribution (after cor-

rection for extinction) of the photospheric emission along sufficiently transparent lines of sight. This is particularly useful to investigate older, redder stellar populations in galaxian disks with scale heights larger than that of the dust. A radiation transfer modeling technique that can be applied to edge-on systems, where the scale height of the stars and dust extinction can be directly constrained, was introduced by Kylafis & Bahcall (1987) and subsequently applied on several galaxies (Xilouris et al. 1997; 1998; 1999, hereafter referred to as X97, X98, X99 respectively). Radiative transfer codes in combination with observations of nearby edge-on galaxies were also used by Ohta & Kodaira (1995) and Kuchinski et al. (1998).

On the other hand, grains act as test particles probing the strength and colour of ultraviolet (UV)/optical interstellar radiation fields. This constitutes an entirely complementary constraint to studies of photospheric emission. In the FIR, grains are moreover detectable over the full range of optical depths present in a galaxy. At least part of this regime is inaccessible to direct probes of starlight, especially at shorter wavelengths, even for face-on systems. This particularly applies to light from young stars located in, or close by, the dust clouds from which they formed, since a certain fraction of the light is locally absorbed. Furthermore, there is at least a possibility that most of the remaining UV and even blue light from young stars that can escape into the disk might be absorbed by diffuse dust there. Observations from IRAS, IRAM (e.g. Neininger et al. 1996; Dumke et al. 1997), SCUBA (e.g. Alton et al. 1998; Israel et al. 1999; Dunne 2000; Bianchi et al. 2000) and ISO (e.g. Haas et al. 1998; Stickel et al. 2000) can provide information on the quantity and spatial distribution of the dust within spiral galaxies.

A combined analysis of the whole UV-optical/FIR/submm/mm spectral energy distribution (SED) of galaxies seems to be a promising way to constrain the problem. Radiative transfer codes for an assumed "sandwich" configuration of dust and stars were applied by Xu & Buat (1995) and Xu & Helou (1996) to account for the energy budget over the whole spectral range. They considered in detail the relative contribution of the non-ionizing UV photons and the optical photons in heating the grains. However these calculations did not incorporate a model for the dust grain emission, nor for radial variations in the absorbed radiation in the disk, and therefore could not account for the exact shape of the FIR SED. Recently, there have been several works modeling the SED of galaxies from UV to submm (Silva et al. 1998; Devriendt et al. 1999), by applying photometric and/or spectrophotometric and chemical evolution models of galaxies. While these models are adequate in describing the general shape of the volume-integrated SED, they make use of many free parameters and of a simplified geometry.

Bianchi et al. (2000) attempted to model NGC 6946 from the UV to FIR using a 3D Monte Carlo radiative-transfer code for a simplified geometry of emitters (a single stellar disk). They concluded that the total FIR output is consistent with an optically thick solution. However, their model did not consider a grain size distribution for grains, stochastic emission of small grains, and the contribution of localized sources within star-forming complexes. This resulted in a poor fit of the FIR SED and a failure to reproduce the IRAS flux densities.

Another work on modeling the UV to submm emission was presented by Efstathiou et al. (2000) for star burst galaxies which were treated as an ensemble of optically thick giant molecular clouds centrally illuminated by recently formed stars. This modeling technique

successfully reproduced the observed SED of M82 and NGC 6090. Such a technique obviously cannot be applied to normal "quiescent" disk galaxies dominated by emission from the diffuse interstellar radiation field.

In Popescu et al. (2000, hereafter referred to as Paper I) we gave a detailed description of a new tool for a combined analysis of the optical-FIR/submm SED of galaxies. This tool included solving the radiative-transfer problem for a realistic distribution of absorbers and emitters and by considering realistic models for dust, taking into account the grain size distribution and stochastic heating of small grains as well as the contribution of HII regions. We applied this tool to the edge-on system NGC 891.

In short, we used the intrinsic spatial distribution of dust and stars (in the B, V, I, J, K bands) derived for this galaxy by X99 as a constraint on the old stellar population and part of the dust distribution. In order to fully explain the optical-FIR-submm SED, it was found necessary to add to the components of the X99's solution both a young stellar population (to correct for a shortfall in FIR brightness in terms of re-radiated non-ionizing UV) and more dust mass (to correct for a shortfall in submm brightness). Our solution explained both the observed SED in the FIR and submm, as well as the observed radial profile at $850\,\mu$m. We found that the dust is predominanly heated by the young stellar population.

Although NGC 891 was chosen for study in Paper I as the prototypical and most extensively observed edge-on galaxy, it exhibits some extreme features, raising the possibility that it might not in fact be representative of a "typical" spiral. In this paper we extend our SED modeling technique to four additional edge-on systems - NGC 5907, NGC 4013, UGC 1082 and UGC 2048 - with the aim of examining whether the features of the solution we obtained for NGC 891 might be more generally applicable. Radiation transfer solutions accounting for the appearance of these four galaxies in the optical bands have been obtained by X99, X98 and X97. We use these solutions to constrain our model for the optical-FIR SEDs in the same fashion as for NGC 891.

The paper is arranged as follows: In Sect. 2 we overview the model and its application to the objects in the present work. In Sect. 3 we present predictions for the FIR SED of all five galaxies studied. These are obtained using our "standard model", i.e. a model with radiation fields derived from the radiation transfer solution for the optical appearance supplemented by a hidden population of young stars embedded in HII regions, but with no additional dust. In Sect. 4 we describe and discuss the SED of one of our four galaxies, namely NGC 5907, in terms of the more complex "two-dust-disk model" and compare this with the corresponding solution obtained for NGC 891 in Paper I. In Sect. 5 we discuss the dependence of the derived star-formation rates on the assumptions of the model, in particular the assumed geometries for the dust and stars. We show that after normalization to disk area, NGC 891 has comparable star-formation characteristics to the other four objects. We also compare the disk-area normalized massive star-formation rate in the five edge-on galaxies, obtained from the optical-FIR SED analysis, with the same quantity derived from H_α measurements of statistical samples of face-on galaxies given in the literature. In Sect. 6 we give a summary of our work.

5.2 Model calculations for the five galaxies

A full description of our model and its application to NGC 891 can be found in Paper I. Here we give an overview of the basic idea and its specific application to the four galaxies.

To determine the propagation of light in a galaxy we take both emitters and absorbers to be smoothly arranged as a superposition of simple cylindrically symmetric geometrical distributions. The assumption of an axisymmetric model and the neglect of the spiral structure does not seem to introduce a systematic error on the estimate of the overall opacity, at least when a statistical sample of edge-on galaxies is considered (Misiriotis et al. 2000). The emitters are divided into a young (predominantly UV-emitting) stellar population, distributed in a disk with a small scale height, an old (predominantly optical-NIR emitting) population, distributed in a disk with a larger scale height and a bulge. The absorbers are arranged in "young" and "old dust disks", associated with the old and young stellar populations. The "old dust disk" has a larger scale height than the "young dust disk", though not so large as the old stellar disk. Both the stellar- and dust-disk distributions are specified as exponential density distributions in radius and height, while the stellar bulge is described by a de Vaucouleurs law. All radial distributions have a common truncation at three scale lengths of the "old dust disk".

The first step in the calculation of the optical-FIR SED is to determine the geometric and amplitude parameters for the old stellar disk and bulge independently in each band pass ranging from the B band to the NIR for a common "old dust disk" (whose geometry and opacity is also determined). This can be achieved by a radiation transfer analysis matching as closely as possible the predicted and observed brightness distributions, following Kylafis & Bahcall (1987) and including inclination as a free parameter. For the five galaxies discussed in this work we adopt the solutions given in X97 and X99 on the basis of observations in B, V and I, and in the case of NGC 891 also in J and K bands.

This analysis of the optical-NIR emission also yields the extinction coefficient as a function of wavelength for the "old dust disk". For all five galaxies studied, the measured extinction law was found to be close to the predicted law derived from the dust model used in the calculation of the IR emission. This corresponds to the graphite-silicate mix and dust size distribution determined for the Galaxy by Mathis et al. (1977) (see Eqs. [2] and [3] of Paper I) with optical constants taken from Laor & Draine (1993). When calculating the IR emission we take grains in the "young dust disk", if present, to have the same size distribution and optical properties as those in the "old dust disk".

To this fixed basis for the old stellar population and associated dust disk, the model allows the addition of a young, UV-emitting stellar population and, optionally, associated dust. The additional stars and dust are taken to be distributed in a common exponential disk with a scalelength equal to that of the already determined intrinsic B-band population, and a scale height fixed at 90 pc (as for the Milky Way). Since this scale height is typically a factor of several times smaller than the scale heights derived by X97 and X99 for the "old dust disk", this constitutes the simplest assumption for the distribution of these extra components, which hide UV-optical indicators of the young stellar population and associated additional opacity. As emphasized in Paper I, a clumpy distribution for the dust associated with the young stellar population is also possible, though very difficult to calculate, and, due to the lack of high angular resolution FIR images of spiral galaxies,

at present not directly verifiable. The luminosity of the young stars is a free parameter of the model, which we express as a recent star-formation rate SFR, based on the population synthesis models of Bruzual & Charlot (2001) for $Z = Z_{\odot}$, a Salpeter IMF with a cut-off mass of $100\,\mathrm{M}_{\odot}$ and $SFR = (1/\tau)\exp(-t/\tau)$ with $\tau = 5\,\mathrm{Gyr}$.

The model also incorporates a parameter F representing the fraction of the non-ionizing UV luminosity from the young stellar population, which is locally absorbed in star-formation regions by optically thick fragments of their parent molecular clouds. This fraction of the luminosity is considered to be re-radiated in the FIR according to a spectral template matching the observed spectrum of galactic HII regions. This template generally has a warmer $60/100\,\mu$m colour than that calculated for the diffuse disk.

Given the intrinsic distributions of stellar emissivities in the UV, optical and NIR, and the distribution of absorbers in the "old" and (if present) the "young dust disks", we then proceed with a radiative transfer calculation to determine the UV-NIR energy density of the radiation field throughout the galaxy. In the absence of solutions in the J and K bands, we extrapolate the energy density from the B, V, I bands assuming a black-body spectral distribution and a colour temperature of 4000 K. In calculating the heating of grains placed in the resulting radiation field, we include an explicit treatment of stochastic emission as detailed in Paper I. The IR-submm emission from grains is then calculated for a grid of positions in the galaxy. Subsequently we integrate over the entire galaxy to obtain the IR-submm SED of the diffuse disk emission. Prior to comparison with observed FIR-submm SEDs, the spectral template for the HII regions, scaled according to the value of F, must be added to this calculated spectral distribution of diffuse FIR emission.

Due to the precise constraints on the distribution of stellar emissivity in the optical-near infrared (NIR) and the distribution of dust in the "old dust disk" yielded by the radiation transfer analysis of the highly resolved optical-NIR images, coupled with the simple assumptions for the distribution of the young stellar population and associated dust, our model has a maximum of three free parameters from which the FIR-submm SED can be fully determined. These are the SFR for massive stars, the parameter F representing the fraction of the non-ionizing UV luminosity from massive stars which is locally absorbed, and the mass of dust in the "young dust disk". In general terms, the last parameter is principally constrained by the submm emission, the non-ionizing UV luminosity by the bolometric FIR-submm output and the factor F (in the absence of high resolution images) by the FIR colour. In the analysis of the five galaxies in subsequent sections, we refer to the following variants of the model:

1. The *simple model*: The simplest possible model takes into account only the information from the optical observations, i.e. the dust and old stellar distribution in the old disk without massive UV-emitting stars. The sole purpose of the "simple model" is to demonstrate that the old stellar population can not adequately heat the dust to account for the observed FIR luminosity.

2. The *standard model*: This is the "simple model" supplemented by a disk population of UV-emitting stars without associated dust, but with localised FIR emission. The free parameters are the SFR and the factor F.

3. The *two-dust-disk model*: This is the "standard model" supplemented by the pres-

Table 5.1: Properties of the galaxies used in the modeling of the FIR-submm SEDs. The dust mass is that quoted in X97 and X99 (corresponding to the "old dust disk" in this paper). The submm fluxes are taken from [1]Alton et al. (1998), [2]Young et al. (1989), [3]Soifer et al. (1989), [4]Moshir et al. (1990). The mm fluxes from [5]Dumke et al. (1997), [6]Guelin et al. (1993).

Galaxy	Hubble type	distance (Mpc)	dust mass ($M_\odot \times 10^7$)	F_{60} (Jy)	F_{100} (Jy)	F_{450} (Jy)	F_{850} (Jy)	F_{1200} (Jy)	F_{1300} (Jy)
NGC 891	Sb	9.5	5.6	50.5[1]	126[1]	32[1]	4.62[1]	-	0.85[6]
NGC 5907	Sc	11.0	1.5	16.3[2]	55.9[2]	-	-	0.54[5]	-
NGC 4013	Sbc	11.6	0.45	7.0[3]	23.1[3]	-	-	-	-
UGC 1082	Sb	37.0	0.99	1.6[4]	3.7[4]	-	-	-	-
UGC 2048	Sb	31.5	3.5	1.7[4]	3.5[4]	-	-	-	-

[1] The flux densities from this reference are integrated in the range $\pm 225''$ along the major axis of the galaxy.

ence of dust in the young stellar disk. The free parameters are the SFR, the factor F, and the dust mass in the "young dust disk".

The predictions of the model calculations are compared with available FIR, submm and mm data from the literature. In Table 5.1 we summarise the data used for comparison in the present work. We adopted 20% errors in the IRAS and IRAM data. For the SCUBA data we adopted the errors quoted by Alton et al. (1998). In Table 5.1 we also give some basic information on the properties of the sample galaxies. One factor in the choice of these galaxies for the radiation transfer analysis by X97 and X99 was their prominent dust lanes.

5.3 Results for the "standard model"

To demonstrate the need for a population of massive stars to account for the observed FIR luminosities in all five galaxies, we first calculated SEDs for the "simple model", in which the stellar and dust distributions are completely determined from the optical-NIR data as described in Sect. 2. These are plotted in the left column of Fig. 5.1 In all cases, the predicted FIR flux densities in the 60 and 100 μm IRAS bands fall short of the observed luminosities by factors of between 5 and 10, showing that the heating of the dust from the old stellar population cannot account for the FIR emission. The results of the "simple model" are summarised in the second column of Table 5.2 ($L_{\rm simple}$), where we give the FIR luminosity of the galaxies that can be attributed to the old stellar population.

Assuming that the optically determined dust content we used for each galaxy is exact, the "standard model" can account for the observed FIR luminosity by transforming non-ionizing UV radiation from massive stars into the FIR through a combination of local absorption and absorption in the diffuse old disk, controlled by the factor F. If all the young stellar luminosity is absorbed locally ($F = 1$), then the efficiency of the transformation from non-ionizing UV to the FIR is unity, as for starburst galaxies. In the total absence of local absorption ($F = 0$) the global absorption efficiency is lower, with a

value depending on the relative geometries of the diffuse dust and the massive stars. In principle, the factor F can be determined from the FIR colours.

We investigated the combinations of F and SFR for which the "standard model" was consistent with the IRAS 60 and 100 μm measurements. For NGC 891 and UGC 2048, good agreement between model and data could be found for values of F well above zero. However, for the remaining galaxies, the IRAS colours required F values of zero or close to zero. This would imply high current star-formation rates and an amplitude in the UV stellar emissivity which would not join up smoothly with the empirically determined B band stellar emissivities. Consequently, we have plotted in Fig. 5.1 the model prediction corresponding to the maximum value of F still consistent with the IRAS colours. This also gives a monotonically increasing SED for the UV-optical stellar emissivities. Corresponding FIR bolometric luminosities ($L_{\rm standard}$), SFRs and factors F are given in Table 5.2, columns 3, 4, 5 respectively. We emphasise however, that in principle one could have a non-steady SFR, so that the tabulated SFR are at the same time lower limits in SFR and upper limits for the factor F. Therefore we can discuss the results for the "standard model" also in terms of a range of possible values for F and SFR, which will be compatible with the range in the IRAS errors.

We remark that a comparison of the values in the second and third column of Table 5.2 reveals that, according to the standard model, only 10% to 30% of the dust emission is powered by the old stellar population.

In the above we have made the assumption that the "standard model" is a sufficiently realistic model of the galaxies. Some evidence that this may not be the case is apparent from Fig. 5.1 (right column), where all the model spectra peak at around 120 μm, well shortward of the typical peak near 150 μm seen in spiral galaxies. This may be an indication that the overall optical depth of the galaxies is underestimated by the "standard model", indicating the presence of a further dust component in the plane of each galaxy. This component may either be smoothly distributed or be in the form of optically thick clumps or some combination of these. For the two galaxies that submm and/or mm measurements are available (NGC 891 and NGC 5907), this is explicitly confirmed by the undershoot of the "standard model" prediction in the submm and mm regime. In Paper I, we used the available submm fluxes to quantify the missing dust and introduced the "two-dust-disk model", which successfully reproduced the spectrum and the spatial distribution of the FIR emission in NGC 891. In the next section we will apply the "two-dust-disk model" to NGC 5907 to determine the total dust content of this galaxy and examine the effect of this more realistic case on the derived SFRs.

5.4 Application of the "two-dust-disk model" to NGC 5907

In Paper I we proved that in NGC 891 the amount of dust (on the basis of the grain optical constants adopted) quoted by X99 is underestimated by a factor of two, and that the addition of a second dust disk, that follows the spatial distribution of the young stellar population, reproduces very well the observed FIR luminosity and the radial profiles observed by Alton et al. (1998). For NGC 5907, the measurement at 1200 μm by Dumke

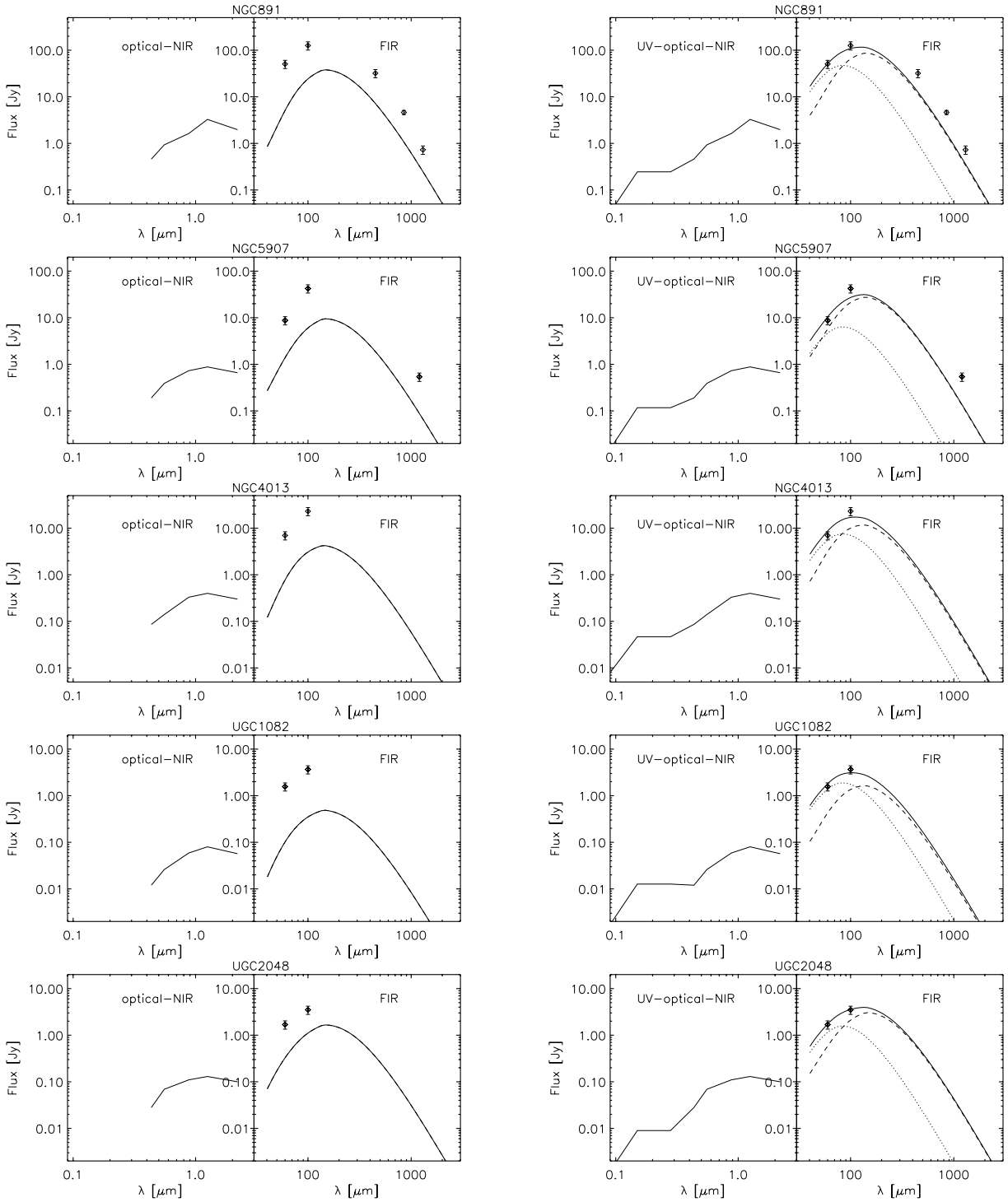

Figure 5.1: The SED of the 5 galaxies. In the left column the SED is derived for the "simple model". In the right column the SED is derived for the "standard model". The predicted FIR emission from the diffuse disk is plotted with dashed lines and the contribution of localised sources with dotted lines. The corresponding SFR and factor F for each galaxy are given in Table 5.2. For NGC 891 and UGC 2048, the model corresponding to the value of F which best fits the IRAS colour is plotted. In the cases of NGC 5907, NGC 4013 and UGC 1082, the model corresponding to the maximum value of F still consistent with the IRAS colour is plotted (see text).

Table 5.2: Results for the "standard model". $L_{\rm simple}$ denotes the bolometric re-radiated luminosity when only the old stellar population (B, V, I, J, K bands) is taken into account (i.e. for the "simple model"). $L_{\rm standard}$ denotes the bolometric re-radiated luminosity obtained by integrating the solution for the "standard model" as plotted in Fig. 5.1. Columns 4 and 5 contain the corresponding SFRs and factors F.

Galaxy	$L_{\rm simple}$ $\mathrm{W}\times10^{35}$	$L_{\rm standard}$ $\mathrm{W}\times10^{35}$	SFR $\mathrm{M_\odot yr^{-1}}$	F
NGC 891	10.8	48.1	3.48	0.28
NGC 5907	3.7	15.5	2.17	0.08
NGC 4013	2.0	11.0	1.23	0.19
UGC 1082	2.3	21.3	2.59	0.23
UGC 2048	5.7	18.3	1.36	0.27

et al. (1997) can be used to constrain the quantity of dust in the second disk.

Inspection of Fig. 5.1 (right column) shows that the "standard model" solution for $F = 0.08$, which is in agreement with the IRAS points, crassly undershoots the 1200 μm point. As for NGC 891, the only way to account for both the IRAS and the 1200 μm observations is to include more dust in our model, as simply increasing the star-formation rate would provide too much luminosity in the IRAS range.

The second-dust-disk's spatial distribution was constrained to follow that of the young stellar population, which is taken to be exponential with scalelength and scaleheight $h_{\rm d} = 5020$ pc and $z_{\rm d} = 90$ pc respectively (see Sect. 2). To find the solution, the total amount of dust in the second dust disk was varied jointly with the SFR until the FIR-submm SED of our model fitted all three measurements. In Fig. 5.2 we present the resulting spectrum overlaid with the data. This spectrum corresponds to a SFR$= 2.2\,\mathrm{M_\odot yr^{-1}}$ and $F = 0.10$. The total dust mass in the second dust disk is $4.5 \times 10^7\,\mathrm{M_\odot}$. By comparison, the dust mass quoted for the old disk of NGC 5907 by X99 is $1.5 \times 10^7\,\mathrm{M_\odot}$.

Thus, we have had to add 3 times more dust over the quantity implied by the observed dust lane to obtain agreement with the data on the basis of the "two-dust-disk model". The derived value of F is still very low, but the spectrum of the diffuse component is too warm (NGC 5907 is more optically thin than NGC 891) to allow the addition of a warm component related to HII regions. While we could have produced a colder spectrum for the diffuse emission, allowing some room for HII regions, this would have been at the cost of adding yet more dust in the second disk. A larger quantity of dust in the second disk does not seem very likely, as the total dust mass for the fitted $F = 0.10$ case already implies a gas-to-dust ratio of 130 by mass (instead of 520 according to X99). As a comparison, the gas-to-dust ratio in the Milky Way is 133.

The total IR-submm re-radiated luminosity of NGC 5907, obtained by integrating the $F = 0.10$ "two-dust-disk model" SED, is 50.5×10^{35} W out of which 27.0×10^{35} W is attributed to heating from the young stellar population. Thus, about 40% of the dust emission is powered by the old stellar population. More dust in the "young dust disk", a lower SFR and a higher factor F would increase the disk opacity and thus the contribution of the old stellar population, but we excluded this solution due to the high dust-to-gas ratio. The 40% contribution from the old stellar population represents

an upper limit, since a possible clumpiness in the dust distribution would decrease the absorption efficiency in the optical band.

On the basis of the model's inherent assumption, that all the dust (in both disks) of the galaxy is distributed smoothly, the central face-on optical depth in the optical band is $\tau_{\rm v} = 1.4$ for NGC 5907.

The major difference between NGC 891 and NGC 5907, on the basis of the "two-dust-disk model", is that the spectrum of the former apparently allows for the existence of a larger contribution from HII regions. Presumably NGC 5907 must have HII regions, and there is no obvious reason why the local properties of these HII regions, in particular the probability of local absorption of the UV radiation, should differ between the two systems.

One potential way out of this difficulty might be to suppose that the spectral template for the HII regions used in our model underestimates the associated submm emission. As stated in Paper I, we did not attempt to include potential cold dust emission components that might be expected from "parent" molecular clouds in juxtaposition to their "offspring" HII regions. These might contribute a significant fraction of the observed submm emission, but be relatively faint in the IRAS range. If so, the dust content and the luminosity of the diffuse disk would be lower for both galaxies, but more so for the more optically thin diffuse disk of NGC 5907. This would make room for larger values of F in the model fits, particularly for NGC 5907.

An alternative scenario, also discussed in Paper I, would be the presence of truly quiescent cold dust clouds in the disk not associated with HII regions. In that case, the difference between the two galaxies might indicate a greater star-formation activity in the disk of NGC 891, in the sense that a larger proportion of the cold dust clouds in the disk had been triggered into massive star formation.

5.5 Discussion

Our results confirm that it is a common tendency for edge-on galaxies to hide a significant fraction of their dust from optical extinction studies. In two cases where sub- or near-mm data are available (NGC 891, as analyzed in Paper I and NGC 5907 in this work), we have modeled the FIR-submm SED assuming that the additional dust is distributed in a second diffuse disk associated with the young stellar population. We have found that the SEDs could be fitted in terms of total dust masses of respectively twice and four times the masses inferred by X99 from the optical radiation transfer analysis for NGC 891 and NGC 5907. The corresponding SFRs and local non-ionizing UV absorption factors F in the best fits were SFR $= 3.8\,{\rm M}_\odot{\rm yr}^{-1}$ and $F = 0.22$ for NGC 891 and SFR $= 2.2\,{\rm M}_\odot{\rm yr}^{-1}$ and $F = 0.10$ for NGC 5907.

The main uncertainty in the inferred SFRs is the value of the factor F. In principle, F can be determined from the colour of the FIR SED, especially the $60/100\,\mu$m colour ratio. However, as discussed in Sect. 4, the value of the factor F, which can be fitted, in practice is constrained by the assumption of the "two-dust-disk model" that all the additional dust needed to fit the submm measurements is diffuse. In reality, the geometry of the additional dust could be, as emphasised in Paper I, in the form of optically thick clumps associated with the HII regions. In this case the inferred SFRs would, depending

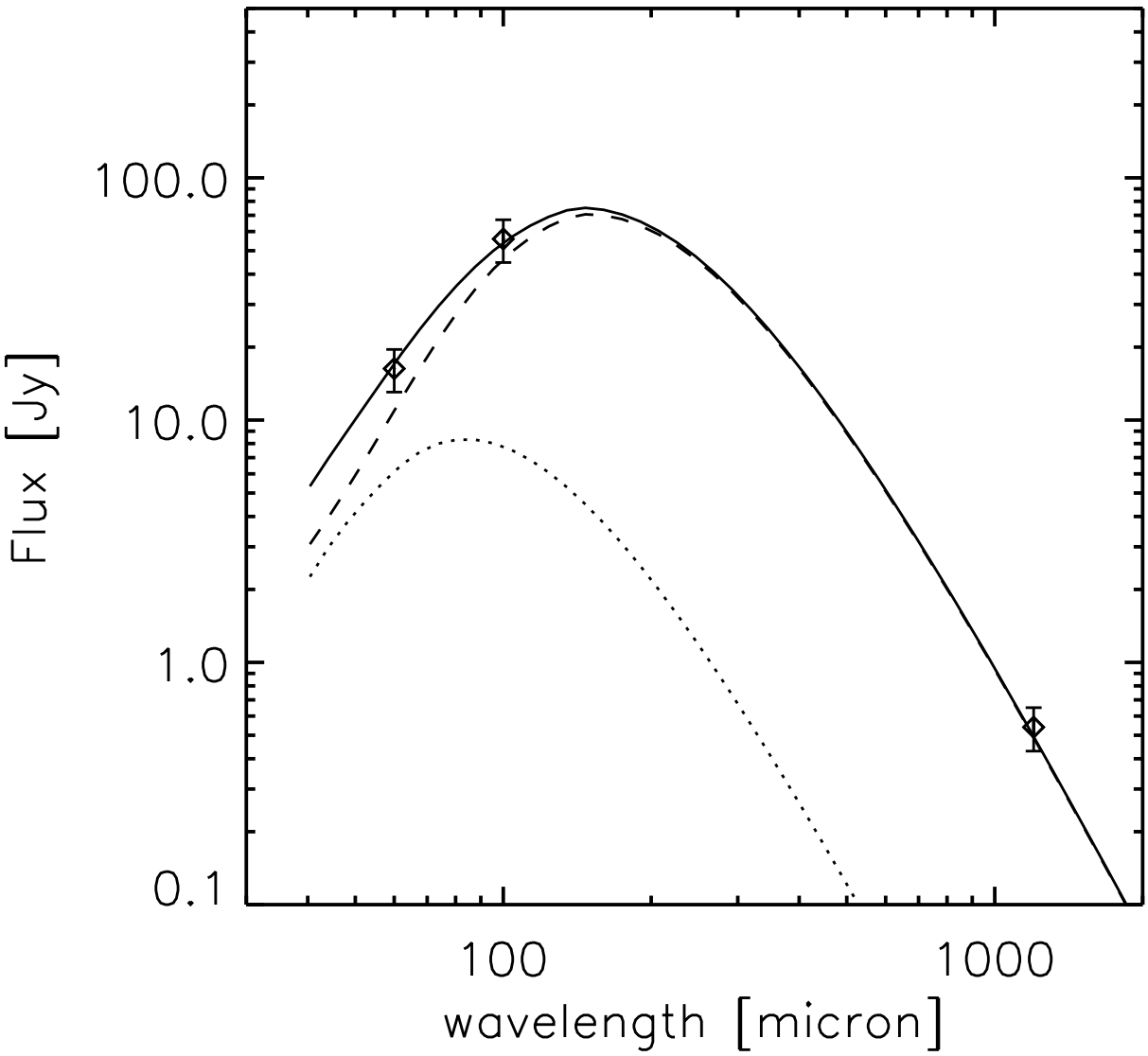

Figure 5.2: SED of the "two-dust-disk model" for NGC 5907 for $F = 0.10$ and SFR $= 2.2\,\mathrm{M}_{\odot}\mathrm{yr}^{-1}$, overlaid with data points given in Table 5.1. The predicted FIR emission from the diffuse disk is plotted with a dashed line and the contribution of localized sources with a dotted line.

on the factor F, differ from those determined on the assumption of a purely diffuse dust distribution without local absorption. However, at present, the available data does not allow us to quantify the clumpy component of UV-absorbing dust.

The SFRs and factors F inferred from the "standard model" for NGC 891 and NGC 5907 in Sect. 3 (where the dust content and distribution is determined from X99's optical analysis) hardly differs from the values determined from the "two-dust-disk model" applied to NGC 891 and NGC 5907 in Sect. 4. This is at first sight surprising, as one would expect lower SFRs due to the higher opacity of the diffuse disk in the "two-dust-disk model". However, the SFR determined from the "standard model" was obtained by fitting the SEDs exclusively to the IRAS 60 and 100 μm measurements common to

the sample of the 5 galaxies. The reason that the SFRs determined from the "standard model" are so similar to those derived from the "two-dust-disk model" is simply that the additional submm luminosity arises from the extra dust (from the second dust disk) rather than from additional SFR. As remarked in Sect. 3, the rather warm SEDs for all the "standard model" fits suggest that additional dust is present in the disks of all 5 galaxies.

To statistically evaluate our results for SFR, we make the assumption that the SFRs determined from the "standard model" fits to the IRAS 60 and 100 μm measurements for our sample of 5 galaxies give, as is the case of NGC 891 and NCG 5907, a reasonable estimate of the SFR which would have been obtained with an analysis based on the "two-dust-disk model". We can then compare the SFR characteristics of the 5 edge-on galaxies with the larger sample of 61 galaxies with inclinations less than 75 degrees which were studied by Kennicutt (1998) on the basis of H_α measurements.

Fig. 5.3 depicts the relation between the disk-averaged surface density in SFR ($\Sigma_{\rm SFR}$) determined from the "standard model" as a function of the average gas surface density ($\Sigma_{\rm g}$) for the 5 galaxies. The plotted data is summarized in Table 5.3. The $\Sigma_{\rm SFR}$ is calculated from the SFRs determined from the "standard model" and listed in Table 5.2. The full range in conceivable SFRs is given by the vertical error bars. The upper and lower limits for the SFRs are calculated such that the predicted SED is still consistent with the IRAS colours (within the 20% IRAS error bars). Lower error bars are not given when the plotted SFRs represent lower limits for the SFR (maximum values for the factors F, see discussion in Sect. 3). In these cases lower limits would be possible only if we allowed for different sources of uncertainties, like variations in the spectral shape of the template used for the HII regions. However this is hard to quantify, and in the following we assume that the errors of the SFR are given only by the uncertainties in the IRAS data.

The $\Sigma_{\rm g}$ were calculated from the gas masses taken from García-Burillo et al. (1992) and Rupen (1991) respectively for H_2 and HI in NGC 891, from Dumke et al. (1997) for H_2 and HI in NGC 5907, from Bottema (1995) and Gomez & Garcia (1997) for H_2 and HI in NGC 4013, from Giovanelli & Haynes (1993) for HI in UGC 1082 and from Huchtmeier & Richter (1989) for HI UGC 2048. In the last two cases, where only data for HI was available, we estimated the total gas mass by doubling the HI gas mass. The horizontal error bar corresponds to the uncertainty in the gas masses for which we adopted an average 0.2 dex error. The surface area of the disk was calculated for $R_{\rm o} = (3 \pm 0.5) h_{\rm d}$, where $h_{\rm d}$ is the intrinsic radial scalelength determined from the radiation-transfer modeling in the I band. In their analysis of surface photometry of the outer regions of spiral disks, Pohlen et al. (2000) show that the disk boundaries are typically in this range.

The points for the 5 galaxies in Fig. 5.3 lie within the area of the diagram occupied by the galaxies in the Kennicutt sample. The match is even better for those members of the Kennicutt sample with Hubble types Sb to Sc. This agreement is quite reassuring, bearing in mind the several factors which could introduce a systematic difference between the SFRs inferred for a sample of nearly face-on systems from H_α measurements compared with the present technique for edge-on systems based on an analysis of broad-band non-ionizing UV re-radiated in the FIR-submm range.

Firstly, the H_α analysis is sensitive to the most massive stars and in particular to the assumed mass cut of 100 $M_\odot$. Whereas the FIR-submm modeling also assumes the same

mass cut in the conversion of SFR to non-ionizing luminosity (see Sect. 2 and Paper I), our model is less sensitive to this effect.

Secondly, whereas the H_α is sensitive to the star-formation history of the last 10^7yr, our broad-band FIR-submm SED analysis samples approximately the last 10^8yr. Thus, our analysis is consistent with the basic hypothesis (see Kennicutt 1998) for "normal" spiral galaxies of a steady star-formation activity. In principle, we could extend our analysis based on our determinations of the intrinsic populations and use the determined intrinsic colours to determine more accurately the SFR history of the galaxies, though this is beyond the scope of this paper.

The assumption of a steady-state star-formation rate is also broadly consistent with the timescales for the exhaustion of the current gas supply under the derived SFRs. The dotted, dashed and dot-dashed lines in Fig. 5.3 represent star-formation efficiencies corresponding to consumptions of 100, 10 and 1 percent of the gas mass in 10^8 yr. We note that in constructing Fig. 3, we have assumed that the HI line emission, from which the gas masses for the 5 edge-on galaxies were in part determined, have not been affected by self absorption in the 21cm line. The effect of self-absorption would be to shift the points for the 5 edge-on galaxies to the left of the positions corresponding to their actual gas surface densities in Fig. 5.3.

Thirdly, the SFRs derived from H_α were corrected by a single factor for extinction, despite the varying orientations. As well as possibly affecting the vertical position of the galaxies on the plot, this may induce some scatter, especially if all the dust were diffusely distributed. The systematic effect may be expressed in terms of the factor F: an overestimation of the factor F is equivalent to an overestimation of the local extinction in the star-formation regions (statistically averaged over the population of HII regions in a disk). Thus, while moving to higher factors F would move the points for the 5 galaxies towards lower SFRs, it would have the opposite effect for the SFRs determined from the H_α.

Lastly, we remark that NGC 891 does not appear as an exceptional system compared with the other 4 galaxies in our sample (and with Kennicutt's [1998] normal galaxy sample) on the basis of SFR normalized to disk area. Our work thus provides no evidence that this galaxy's exceptional layer of extraplanar H_α-emitting diffuse ionizing gas (e.g. Hoopes et al. 1999) and surrounding X-ray-emitting hot gas (e.g. Bregman & Houck 1997) is attributable to unusual star-formation activity.

5.6 Summary

- This paper is the second part on a series of papers dedicated to the modeling of the SEDs of disk galaxies. In Paper I we described a new tool for the analysis of the UV to the submm SED and applied this tool to the well known nearby edge-on galaxy NGC 891. In the present paper we have extended the analysis from Paper I to a sample of four additional edge-on galaxies (NGC 5907, NGC 4013, UGC 1082, UGC 2048) and proved that the solution obtained for NGC 891 is generally valid. We have also shown that NGC 891 is not an exceptional system in terms of its SFR density.

Table 5.3: The average gas surface density ($\Sigma_{\rm g}$) and disk-averaged SFR surface density ($\Sigma_{\rm SFR}$) for our galaxy sample. The lower and upper limits in the $\Sigma_{\rm SFR}$ are also given together with the disk area used to normalize the SFRs and gas masses.

Galaxy	$\log \Sigma_{\rm g}$ $\frac{M_\odot}{pc^2}$	$\log \Sigma_{\rm SFR}$ $\frac{M_\odot}{yr\,kpc^2}$	$\log \Sigma_{\rm SFR}^{\rm min}$ $\frac{M_\odot}{yr\,kpc^2}$	$\log \Sigma_{\rm SFR}^{\rm max}$ $\frac{M_\odot}{yr\,kpc^2}$	Area kpc^2
NGC 891	1.09	-2.30	-2.54	-2.07	687
NGC 5907	1.27	-2.29	-2.29	-2.15	421
NGC 4013	1.40	-1.85	-1.85	-1.63	88
UGC 1082	0.87	-2.27	-2.27	-1.89	482
UGC 2048	0.70	-2.80	-3.17	-2.60	855

- In all the systems the dust is predominantly heated by the young stellar population. The contribution of the old stellar population can account for at most 40%.
- The SFRs derived from our "standard model" are consistent with the SFRs derived from the more sophisticated "two-dust-disk model" and are also consistent with the Kennicutt's (1998) Schmidt law for disk galaxies.

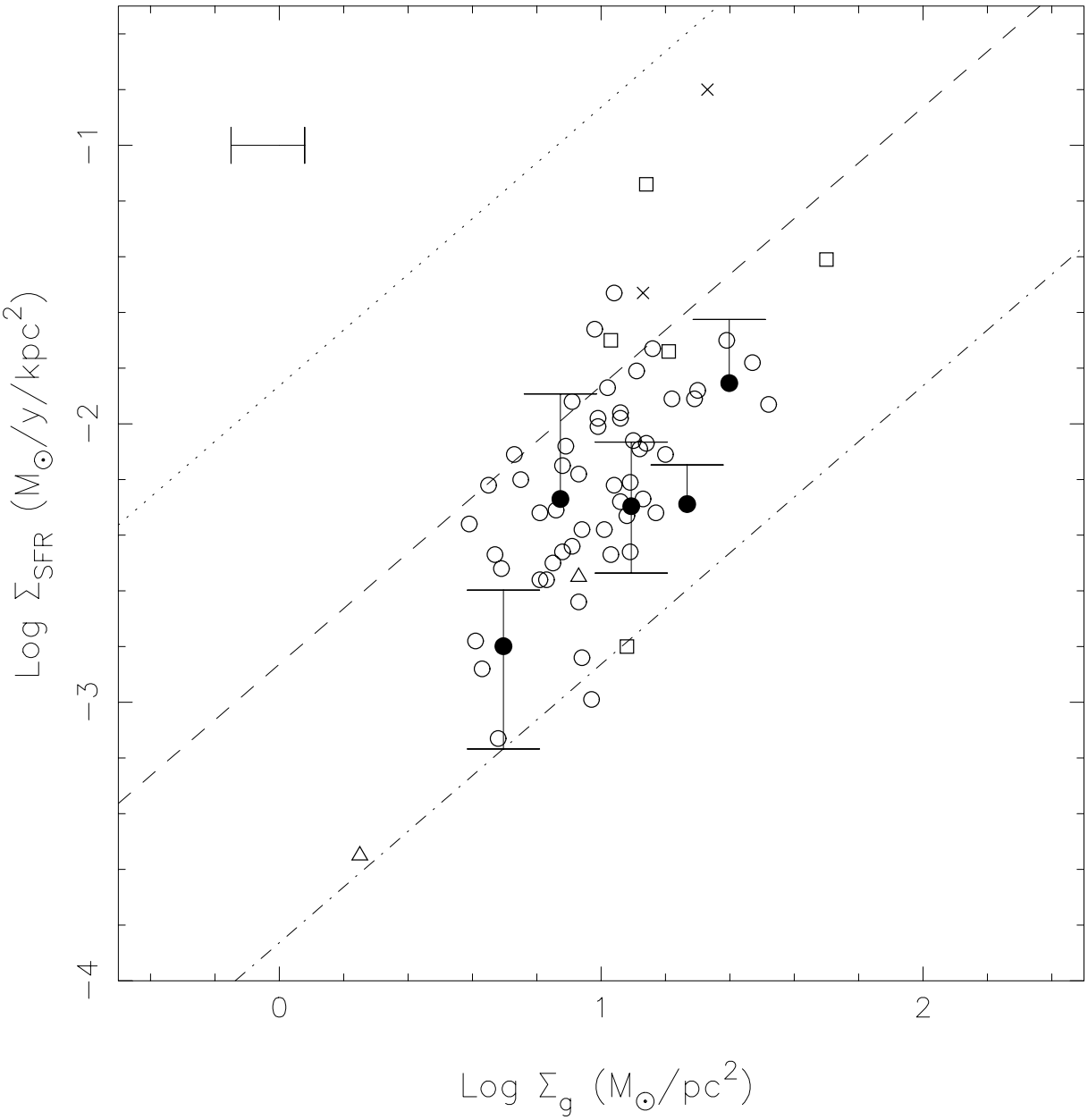

Figure 5.3: Disk-averaged SFR surface density ($\Sigma_{\rm SFR}$) as a function of average gas surface density ($\Sigma_{\rm g}$) for our galaxy sample and for the sample of Kennicutt (1998) of 61 normal disk galaxies with SFR determined from H_α measurements. The 5 galaxies from our sample are plotted as filled circles and the corresponding $\Sigma_{\rm SFR}$, $\Sigma_{\rm SFR}^{\rm min}$, $\Sigma_{\rm SFR}^{\rm max}$, $\Sigma_{\rm g}$ and disk areas are listed in Table 5.3. The SFR surface densities were calculated by averaging the SFRs determined from the "standard model" (Sect. 3) over disks with an optically defined boundary ($R_{\rm o}$) taken to be 3 times the intrinsic radial scalelength $h_{\rm s}$ determined from the radiation transfer modeling in the I band. The galaxies from the sample of Kennicutt are plotted as open circles (Sb,Sc,SBb,SBc), triangles (Sa), open squares (Unknown/Not Available), crosses (Irr). The dotted, dashed and dot-dashed lines represent star-formation efficiencies corresponding to consumptions of 100, 10 and 1 percent of the gas mass in 10^8 yr.

Bibliography

Alton, P. B., Bianchi, S., Rand, R. J., et al., 1998, ApJ, 507, L125

Bianchi, S., Davies, J. I., Alton, P. B., Gerin, M., Casoli, F., 2000, A&A, 353, L13

Bianchi, S., Davies, J. I., Alton, P. B., 2000, A&A, 359, 65

Bottema, R., 1995, A&A, 295, 605

Bregman, J. N., & Houck, J. C., 1997, ApJ, 485, 159

Bruzual, A. G., & Charlot, S., 2001, in preparation

Devriendt, J. E. G., Guiderdoni, B., Sadat, R., 1999, A&A, 350, 381

Dumke, M., Braine, J., Krause, M., et al., 1997, A&A, 325, 124

Dunne, L., Eales, S., Edmunds, M., et al., 2000, MNRAS, 315, 115

Efstathiou, A., Rowan-Robinson, M., Siebenmorgen, R., 2000, MNRAS, 313, 375

García-Burillo, S., Guélin, M., Cernicharo, J., Dahlem M., 1992, A&A, 266, 21.

Giovanelli, R., Haynes, M. P., 1993, AJ, 105, 1271

Gomez de Castro, A. I., García-Burillo, S., 1997, A&A, 322, 381

Guelin, M., Zylka, R., Mezger, P.G., et al., 1993, A&A, 279, L37

Haas, M., Lemke, D., Stickel, M., et al. 1998, A&A, 338, L33

Hoopes, C. G., Walterbos, R. A. M., & Rand, R. J., 1999, ApJ, 522, 669

Huchtmeier, W. K., Richter, O. G., 1989, A general catalog of HI observations of galaxies, New York, Springer-Verlag

Israel, F. P., ven der Werf, P. P., Tilanus, R. P. J., 1999, A&A, 344, L83

Kennicutt, R. C. Jr., 1998, ApJ, 498, 541

Kuchinski, L. E., Terndrup, D. M., Gordon, K. D., Witt, A. N., 1998, AJ, 115, 1438

Kylafis, N. D., Bahcall, J. N., 1987, ApJ, 317, 637

Laor, A., Draine, B. T., 1993, ApJ, 402, 441

Mathis, J. S., Rumple, W., Nordsieck, K. H., 1977, ApJ, 217, 425

Misiriotis, A., Kylafis, N. D., Papamastorakis, J., Xilouris, E. M., 2000, A&A, 353, 117

Moshir, M., et al. 1990, IRAS Faint Source Catalogue.

Neininger, N., Guélin, M., García-Burillo, S., et al., 1996, A&A, 310, 725

Ohta, K., Kodaira, K., 1995, PASJ, 47, 17

Pohlen, M., Dettmar, R.-J., Lutticke, R., 2000, A&A, 357, 1

Popescu, C. C., Misiriotis, A., Kylafis, N. D., Tuffs, R. J., Fischera, J., 2000, A&A, 362, 138 (Paper I)

Rupen, M. P., 1991, AJ, 102, 48

Silva, L., Granato, G .L., Bressan, A., Danese, L., 1998, ApJ, 509, 103

Soifer, B. T., Boehmer, L., Neugebauer, G., Sanders, B., 1989, AJ, 98, 766

Stickel, M., Lemke, D., Klaas, U., et al. 2000, A&A, 359, 865

Xilouris, E. M., Kylafis, N. D., Papamastorakis, J., Paleologou, E. V., Haerendel, G., 1997, A&A, 325, 135 (X97)

Xilouris, E. M., Alton, P. B., Davies, J. I., et al., 1998, A&A, 331, 894 (X98)

Xilouris, E. M., Byun, Y. I., Kylafis, N. D., Paleologou, E. V., Papamastorakis, J., 1999, A&A, 344, 868 (X99)

Xu, C., Buat, V., 1995, A&A, 293, L65

Xu, C., Helou, G., 1996, ApJ, 456, 163

Young, J. S., Xie, S., Kenney, J. D. P., Rice, W. L., 1989, ApJS, 70, 699

Chapter 6

Morphology, photometry and kinematics of N-body bars. I Three models with different halo central contrations

We discuss the morphology, photometry and kinematics of the bars which have formed in three N-body simulations. These have initially the same disc and the same halo-to-disc mass ratio, but their haloes have very different central concentrations. The third model includes a bulge. The bar in the model with the centrally concentrated halo (model MH) is much stronger, longer and thinner than the bar in the model with the less centrally concentrated halo (model MD). Its shape, when viewed side-on, evolves from boxy to peanut and then to X-shaped, as opposed to that of model MD, which stays boxy. The projected density profiles obtained from cuts along the bar major axis, both for the face-on and the edge-on views, show a flat part, as opposed to those of model MD which are falling rapidly. A Fourier analysis of the face-on density distribution of model MH shows very large $m = 2$, 4, 6 and 8 components. Contrary to this for model MD the components $m = 6$ and 8 are negligable. The velocity field of model MH shows strong deviations from axial symmetry, and in particular has wavy isovelocities near the end of the bar when viewed along the bar minor axis. When viewed edge-on, it shows cylindrical rotation, which the MD model does not. The properties of the bar of the model with a bulge and a non-centrally concentrated halo (MDB) are intermediate between those of the bar of the other two models. All three models exhibit a lot of inflow of the disc material during their evolution, so that by the end of the simulations the disc dominates over the halo in the inner parts, even for model MH, for which the halo and disc contributions were initially comparable in that region.

6.1 Introduction

A bar is an elongated concentration of matter in the central parts of a disc galaxy. Within this loose and somewhat vague definition fit a number of very different objects. Thus dif-

ferent bars have very different masses, axial ratios, shapes, mass and colour distributions. They can also have widely different kinematics. Several observational studies have been devoted to the structural properties of bars and/or to their morphology, photometry and kinematics, thus providing valuable information on these objects and on their properties.

Many N-body simulations of the evolution of disc galaxies have witnessed the formation of bars. Most studies have focused on understanding what favours or hinders bar formation. Not much work, however, has been done on the "observable" properties of N-body bars. This is quite unfortunate since such studies are necessary for the comparison of real and numerical bars. In fact several observational studies have taken an N-body simulation available in the literature and have analysed it in a way similar to that used for the observations in order to make comparisons (e.g. Kormendy 1983, Ohta, Hamabe & Wakamatsu 1990, Lütticke, Dettmar & Pohlen 2000). Although this is very useful, it suffers from lack of generality, since the specific simulation may not be appropriate for the observational question at hand, and since it does not give a sufficient overview of the alternative properties N-body bars can have. Here we will approach the comparisons between real and N-body bars from the simulation side, giving as wide a range of alternatives as possible, while making an analysis as near as possible to that used by observers. We hope that in this way our work will be of use to future observational studies and will provide results for detailed comparisons.

An obvious problem when comparing N-body bars to real bars is that simulations trace mass, while observations give information on the distribution of light. The usual way to overcome this hurdle is to assume a constant M/L ratio. This assumption should be adequate for the inner parts of galaxies (e.g. Kent 1986, Peletier & Balcells 1996), particularly early types that have relatively little star formation, and in the NIR wavelengths, where the absorption from dust is least pronounced.

By their nature, real bars can be observed in only a much more limited way than N-body bars. Galaxies are projected on the plane of the sky and their deprojection is not unambiguous, particularly for barred galaxies, which are the object of the present study. This problem of course does not exist for simulations, which we furthermore can "observe" from any angle we wish. It is thus possible to "observe" the same snapshot both face-on and edge-on. This is of course impossible to do for real galaxies and has led to a number of complications e.g. regarding the nature of peanuts and the 3D structure of bars. A second limitation is that in observations light is integrated along the line of sight and one can not observe the various components separately, as in N-body bars. Finally the biggest limitation comes from the fact that there is no direct way to observe dark matter, while in N-body simulations the halo can be analysed as any other component of the galaxy. All these limitations lead to complications in the comparisons, but are also one of the reasons for which the observations of N-body bars are most useful. We can observe our bars both in the restricted manner that real galaxies allow and in the more detailed manner accessible to simulations and, by comparing the two, derive the signatures of the latter in the former. This can help us obtain information on properties of real bars which are not directly observable.

In this paper we will discuss at length the observable properties of three simulations. In section 6.2 we present the simulations and their initial conditions. In section 6.3 we present the basic properties of our three fiducial models and in section 6.4 the shape and

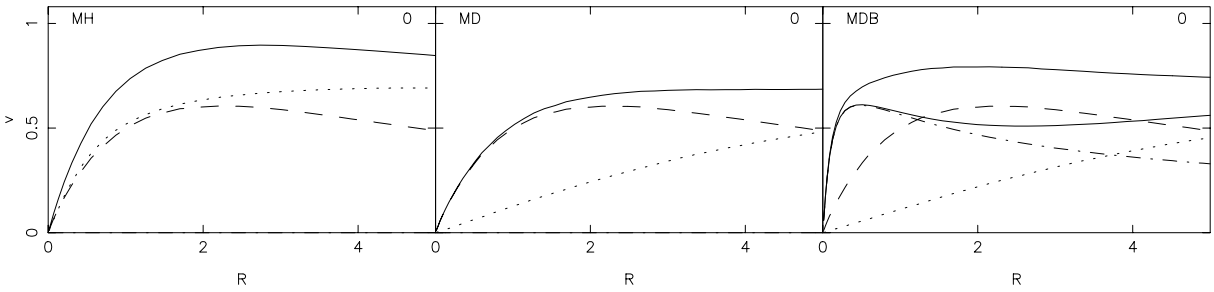

Figure 6.1: Circular velocity curves of our three fiducial models at the beginning of the simulation. The dashed, dotted and dash-dotted lines give the contributions of the disc, halo and bulge respectively, while the thick full lines give the total circular velocity curves. For simulation MDB we also give the the total contribution from the two spherical components with a thin solid line. The left panel corresponds to simulation MH, the middle one to simulation MD and the right one to simulation MDB. The simulation name is given in the upper left corner and the time in the upper right corner of each panel.

the axial ratio of the isodensities in the bar region. Projected density profiles with the disc seen face-on and edge-on are presented in sections 6.5 and 6.6, respectively. In section 6.7 we present the Fourier components of the mass distribution seen face-on, in section 6.8 we compare various ways of measuring the bar length, and in section 6.9 we quantify the peanut shape. Kinematics are presented in sections 6.10 and 6.11 and the shape of the bulge is discussed in section 6.12. We summarise in section 6.13. In a companion paper (hereafter Paper II) one of us (E.A.) will present more simulations, compare to observations and discuss implications about the distribution of the dark matter in barred galaxies.

In this paper and its companion we will willingly refrain from discussing resonances, their location and their effect on the evolution of the bar. This discussion necessarily implies the knowledge of the pattern speed of the bar, which is not directly available from observations. Together with the discussions relying on dynamics and/or some knowledge of the orbital structure it will be left for a future paper.

6.2 Simulations

We have made a large number of simulations of bar-unstable discs, three of which we will discuss in this paper. Each is characteristic of a class of models, other members of which will be discussed in paper II.

In order to prepare the initial conditions we basically followed the method of Hernquist (1993), to which we brought a few improvements, described in Appendix 6.14.

The density distribution of the disc is given by

$$\rho_d(R,z) = \frac{M_d}{4\pi h^2 z_0} \;\; exp(-R/h) \;\; sech^2(\frac{z}{z_0}), \tag{6.1}$$

that of the bulge by

$$\rho_b(r) = \frac{M_b}{2\pi a^2} \quad \frac{1}{r(1+r/a)^3}, \tag{6.2}$$

and that of the halo by

$$\rho_h(r) = \frac{M_h}{2\pi^{3/2}} \quad \frac{\alpha}{r_c} \quad \frac{exp(-r^2/r_c^2)}{r^2+\gamma^2}. \tag{6.3}$$

In the above r is the radius, R is the cylindrical radius, M_d, M_b and M_h are the masses of the disc, bulge and halo respectively, h is the disc radial scale length, z_0 is the disc vertical scale thickness, a is the bulge scale length, and γ and r_c are halo scale lengths. The parameter α in the halo density equation is a normalisation constant defined by

$$\alpha = [1 - \sqrt{\pi} \quad exp(q^2) \quad (1 - erf(q))]^{-1} \tag{6.4}$$

where $q = \gamma/r_c$ (cf. Hernquist 1993). In all simulations we have taken $M_d = 1$, $h = 1$ and have represented the disc with 200 000 particles. The halo mass, calculated to infinity, is taken equal to 5, and r_c is always taken equal to 10. The halo mass distribution is truncated at 15. The disc distribution is cut vertically at $z_{cut} = 3z_0$ and radially at half the halo truncation radius, i.e. $R_{cut} = 7.5$. The velocity distributions are as described by Hernquist (1993) and in Appendix 6.14.

The first two fiducial models that we will discuss at length here have very different central concentrations. For the first one we have taken $\gamma = 0.5$, so that the halo is centrally concentrated and in the inner parts has a contribution somewhat larger than that of the disc. Since the mass of the disc particles is the same as that of the halo particles, the number of particles in the halo is set by the mass of the halo within the truncation radius (in this case roughly 4.8) and in this simulation is roughly equal to 963030. We will hereafter call this model "massive halo" model, or, for short, MH. For the second model we have taken $\gamma = 5$, so that the disc dominates in the inner parts. The halo is represented by 931206 particles. We will hereafter call this model "massive disc" model, or, for short, MD. Both MH and MD models have no bulge. In order to examine the effect of the bulge we will consider a third fiducial model, which is similar to MD but has a bulge of mass $M_b = 0.6$ and of scale length $a = 0.4$. We will hereafter refer to this model as "massive disc with bulge", or, for short, MDB. In the three fiducial simulations we adopted a disc thickness of $z_0 = 0.2$ and $Q = 0.9$. Their circular velocity curves are shown in Figure 6.1, together with the contribution of each component separately. For model MDB we also show the total contribution from the two spherical components. The halo and disc contributions in the inner parts are comparable in the case of model MH, while the disc dominates in model MD. For model MDB as one moves from the center outwards one has first a bulge dominated part, then a disc dominated part and finally a halo dominated part. Thus its evolution could in principle be different from both that of the MH and that of the MD models. All three cases have a flat rotation curve, at least within a radius of five disc scale lengths. If we consider larger radii, say up to 15 disc scale lengths, then the rotation curves for models MD and MDB are still flat, while that of model MH decreases, because its halo is centrally concentrated. By adding an extra extended halo component we can keep the rotation curve flat up to such distances.

This, however, more than doubles the total mass of the system, and raises the number of particles accordingly, to a number which was beyond our CPU capacities, particularly seen the large number of MH-type simulations described in this and the companion paper. We thus ran a simulation with particles of double the mass, and therefore half the number. This allowed us to check that the introduction of this extended halo does not change qualitatively the results of the morphology, photometry and kinematics of the bar. Having established this, and since this simulation has only 100 000 particles in the disc, so that the noise is higher and the quantities describing the bar which are discussed here less well defined, we will present in this paper the results of the simulation without the more extended halo component.

These three simulations are part of a bigger ensemble, covering a large fraction of the available parameter space. In this paper we will discuss only these three, which are each characteristic of a certain type of simulations. By limiting ourselves to three simulations we will be able to make a very thorough analysis of each case. In Paper II we will discuss more simulations in order to assess how certain parameters, like Q or the thickness of the disc, influence the main results presented here.

The simulations were carried out on a Marseille Observatory GRAPE-5 system consisting of two GRAPE-5 cards (Kawai *et al.* 2000) coupled via a PCI interface (Kawai *et al.* 1997) to a Compaq DS 20 or an XP-1000. We used a GRAPE treecode similar to that initially built for the GRAPE-3 system (see e.g. Athanassoula *et al.* 1998). For simulation MH we used an opening angle of 0.7, while for simulations MD and MDB we used an opening angle of 0.6. With the XP-1000 front end, one time-step for 10^6 particles takes roughly 15 sec for $\theta = 0.6$ and less than 12 sec for $\theta = 0.7$. We used a softening of 0.0625 and a time-step of 0.015625. This gave us an energy conservation better than or of the order of one part in a thousand over the entire simulations, which were terminated after $t = 900$, i.e. after 57600 time-steps. Full information on all the particles in the simulation is kept every 20 time units, while information on the total potential and kinetic energy and on the center of mass of the system is saved every 8 time steps, i.e. every 0.125 time units. We calculate on line (Athanassoula *et al.* 1998) the amplitude and the phase of the $m = 2$ and 4 Fourier components of the mass every 0.5 time units. We also produce gif files of the face-on and edge-on distributions of the disc particles every 0.5 time units which, when viewed consecutively as a movie with the help of the xanim software, give a good global view of the evolution.

In this paper, unless otherwise noted, all quantities are given in computer units scaled so that the scale length of the disc is unity, the total mass of the disc equal to 1 and $G = 1$. It is easy to convert them to standard astronomical units by assigning a mass and a scale length to the disc. Thus, if the mass of the disc is taken to be equal to 5×10^{10} $M_\odot$ and its scale length equal to 3.5 kpc, we find that the unit of mass is 5×10^{10} $M_\odot$, the unit of length is 3.5 kpc, the unit of velocity is 248 km/sec and the unit of time is 1.4×10^7 yrs. Thus time 500 corresponds to 7×10^9 yrs and time 800 to 1.1×10^{10} yrs. This calibration, however, is not unique. Adopting different values for the disc scale length and mass would have led to alternative calibrations.

6.3 Two types of N-body bars

Figures 6.2 and 6.3 give some basic information on the three fiducial simulations at times 600 and 800 respectively. The upper panels give the total circular velocity curves together with the contribution of each component separately. In all three cases the disc material has moved inwards as a result of the evolution and the configurations become much more centrally concentrated. As a result, the circular velocity curve of model MH rises much faster than initially and after the rising part stays roughly constant. Also the center-most part is disc dominated, contrary to what was the case at the start of the simulation. The circular velocity curves of models MD and MDB develop a peak near the center, also due to the increased central concentration of the disc material. In model MD all the central part is disc dominated, as it was at the start of the simulation. On the other hand for model MDB there is no region which is disc dominated because of the joint effect of the halo and bulge. There is not much difference between the circular velocity curves at times 600 and 800.

Observed face-on[1] (second and fifth rows in Figures 6.2 and 6.3) the disc particle distributions are quite different in the three fiducial cases. The bar in the MH model is longer and thinner than the bar in model MD. At time $t = 600$ it has "ansae" at the extremities of the bar, similar to those observed in early type barred galaxies. These structures do not exist at time 800. The bar in model MD is rather short and fat, while the bar in model MDB is intermediate both in length and shape of the bars of models MD and MH, but nearer to that of MH.

Model MH has a ring, which observers would call an inner ring since it surrounds the bar and since its radius is roughly equal to the bar semi-major axis. It shows up clearer in the dot-plots of the fifth row than in the isodensity plots of the second row. It can be discerned in the isodensity plots at time 800, but not at time 600, due to the fact that the region between the ring and the bar has a much lower projected surface density at the later time. Such a ring does not exist in the MD model. For model MDB it shows as a broad diffuse structure. In model MH the ring has a density enhancement near the ends of the bar both at times 600 and 800, which is slightly stronger towards the leading side. In fact rings have not been witnessed before this in purely stellar N-body simulations, with the notable exception of the fiducial simulation of Debattista & Sellwood (2000). It is worth noting that both in their simulation and in our MH model the maximum of the halo rotation curve is near the center of the galaxy.

We use the methods described in Appendix 6.15 to determine the parameters of the ring. Applying the local (global) method to model MH at time $t = 600$ we find that the ring has a radius of 3.0 (3.2) and an axial ratio b/a of 0.7 (0.8). It is very thick – the width of the fitting gaussian (cf. Appendix 6.15) being of the order of 1.8 (1.4) –, it is aligned parallel to the bar major axis and its mass is 31 (28) percent of the total disc mass. For time $t = 800$ we find that the radius is 3.6 (3.7) and the axial ratio 0.8 (0.9). The width of the fitting gaussian is 1.4 (1.3), it is aligned parallel to the bar major axis and its mass is 20 (20) percent of the total disc mass. This shows that the ring has become less eccentric and that its diameter has increased with time. The results from the two methods agree

[1]Unless otherwise noted, in this paper we adopt a coordinate system such that the x and y axes lie on the equatorial plane, the y axis being along the bar major axis.

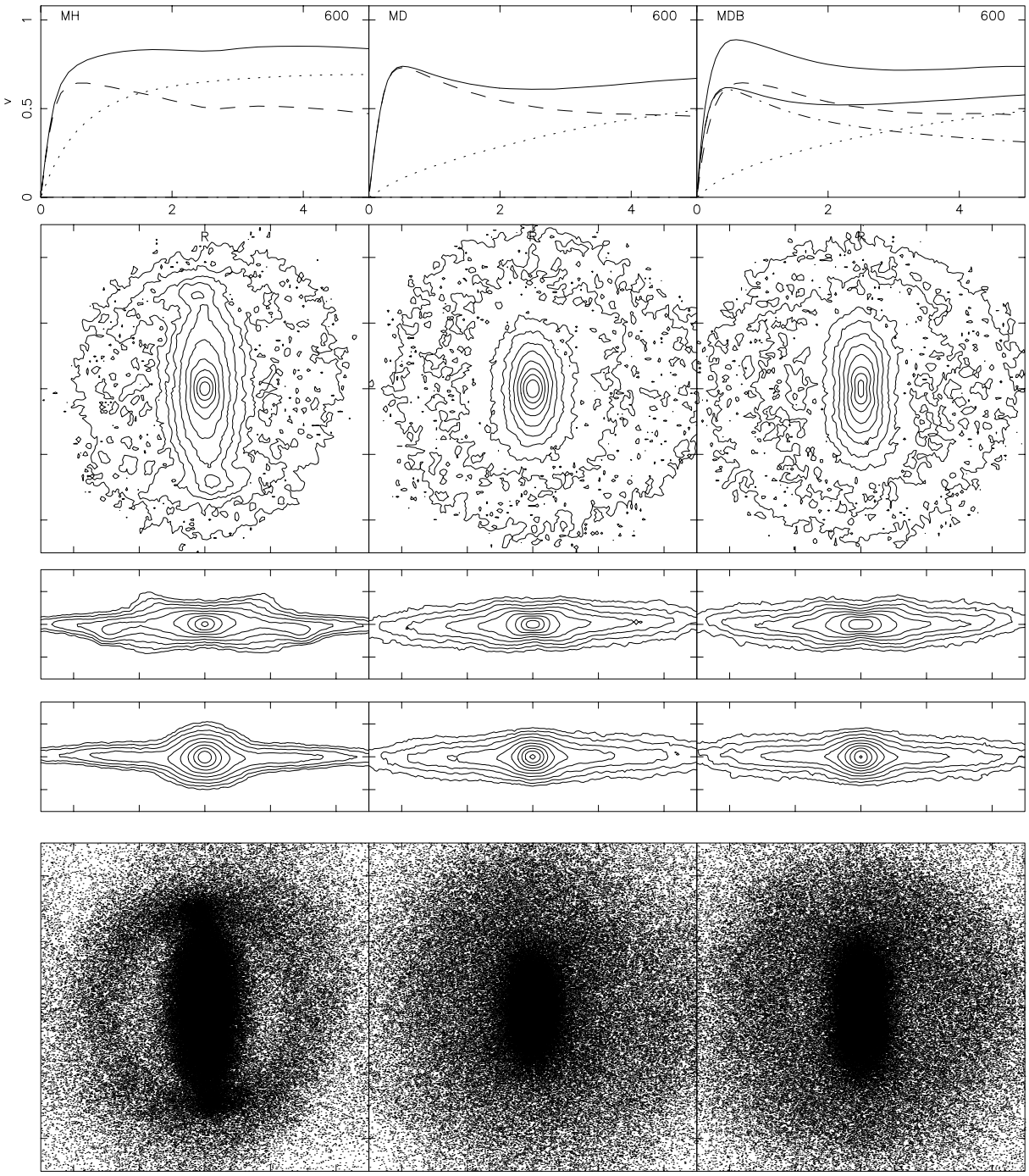

Figure 6.2: Basic information on the three fiducial simulations at time $t = 600$. Left panels correspond to simulation MH, middle ones to simulation MD and right ones to simulation MDB. The upper panels give the circular velocity curve. The dashed, dotted and dash-dotted lines give the contributions of the disc, halo and bulge respectively, while the thick full lines give the total circular velocity curves. For simulation MDB we also give the the total contribution from the two spherical components (thin solid line). The second row of panels gives the isocontours of the density of the disc particles projected face-on, and the third and fourth row the side-on and end-on edge-on views, respectively. The fifth row of panels gives the dot-plots of the particles in the (x, y) plane. The side of the box for the face-on views is 10 units, and the height of the box for the edge-on views is 3.33 units.

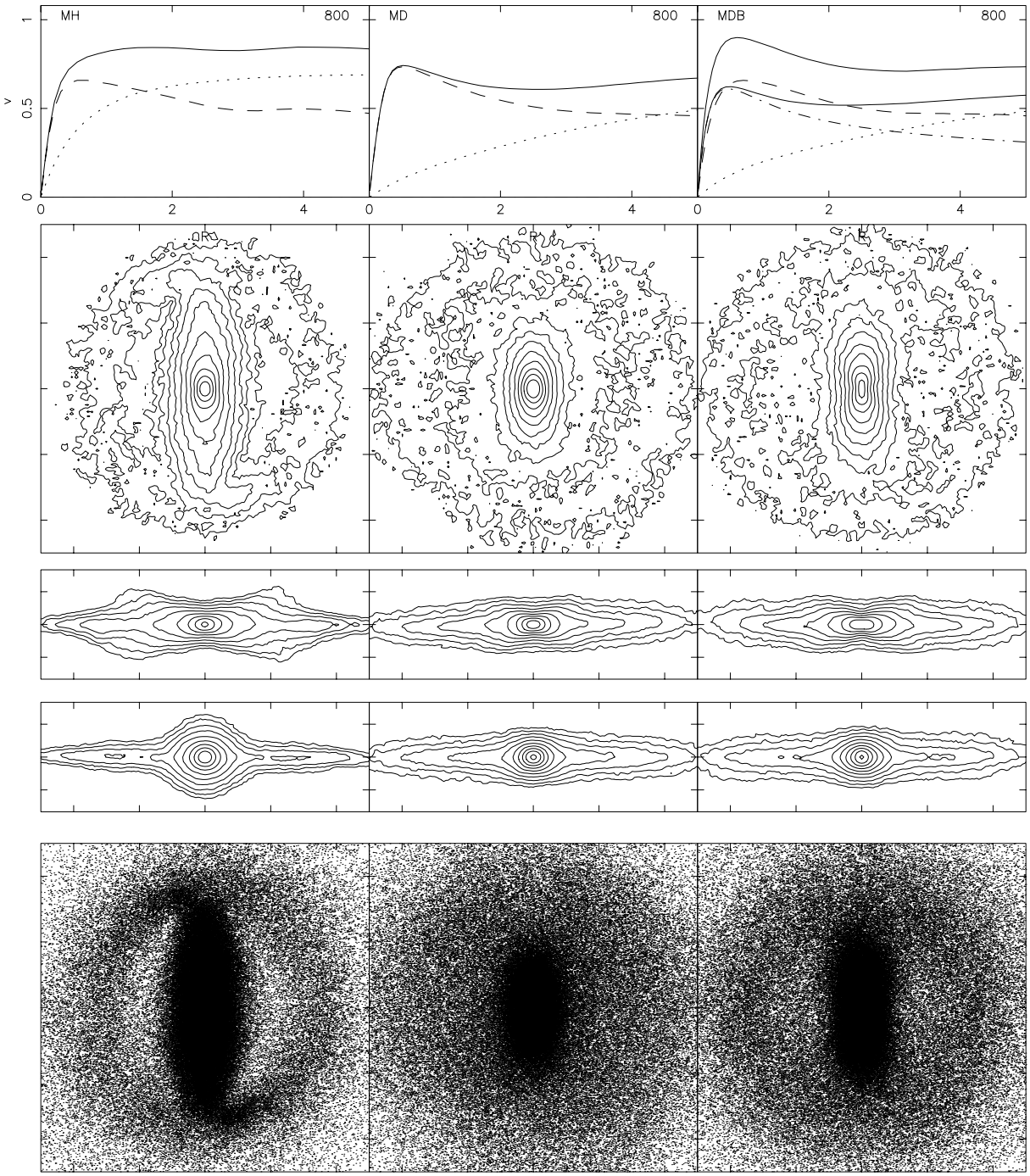

Figure 6.3: Same as the previous figure, but for time $t = 800$.

well, but they both overestimate the mass of the ring, since they consider the total mass under the fitted gaussian, so that the wings of the gaussian contribute substantially. Had we truncated the gaussian we would have obtained a considerably lower value. Since, however, we do not know where to truncate we leave it as is, and let the reader obtain the mass after truncation from the values of the parameters we give above.

Model MDB also shows a ring. At times 600 its radius is 3.1 (3.2) and its axial ratio 0.9 (0.9). It is even broader than the ring in model MH – the width of the gaussian being of the order of 2.1 (1.9) – and thus we can not give a reliable estimate of its mass, as argued in Appendix 6.15. At times 800 its radius is 3.6 (3.6) and its shape is near-circular. Again we note that the size of the ring has increased with time and that its shape has become more circular. Again there is good agreement between the two methods.

The edge-on projections of the disc density (given by isodensities in the third and fourth rows in Figures 6.2 and 6.3) are also widely different in the three fiducial cases. In the side-on[2] view, model MD has a boxy outline. On the other hand model MH is peanut-like at time 600 and is X shaped at time 800. Model MDB has the form of a peanut. Seen end-on, models MH and MDB show a central structure of considerable size, which could well be mistaken for a bulge. This is particularly strong for model MH at time 800. At that time we also see the signature of the ring on the side-on view, as closing isodensities on either side of the central area.

6.4 The axial ratio and shape of the isodensities in the bar region. Face-on view

In order to measure the axial ratio and shape of the bar isodensities seen face-on we project all disc particles on the (x, y) plane on which we superpose a 200 X 200 cartesian grid covering a square of length $(-16, 16)$. The density at the center of each cell is calculated by counting the number of particles in the cell and dividing by its area. The density at intermediate points is calculated using bilinear interpolation. We then fit generalised ellipses to the isodensities. The equation of the generalised ellipse, initially introduced by Athanassoula *et al.* (1990), is

$$(|x|/a)^c + (|y|/b)^c = 1, \tag{6.5}$$

where a and b are the semi-major and semi-minor axes respectively, and c is a parameter describing the shape of the generalised ellipse. For $c = 2$ we obtain a standard ellipse, for $c < 2$ a lozenge, while for $c > 2$ the shape approaches a rectangle, and will, for simplicity, be called hereafter rectangular-like. Athanassoula *et al.* (1990) have used generalised ellipses to quantify the shape of the isophotes of strongly barred early-type galaxies and we will use them here to describe the shape of our N-body bars. Unfortunately the comparison between the two is not as straightforward as it sounds. All galaxies in the Athanassoula *et al.* sample have a sizeable bulge, so that it was not possible to get information on the isophotes of the inner parts of the bar. Since isophotes are determined

[2]We call side-on view the edge-on view for which the line of sight is along the bar minor axis. Similarly we call end-on view the edge-on view where the line of sight is along the bar major axis.

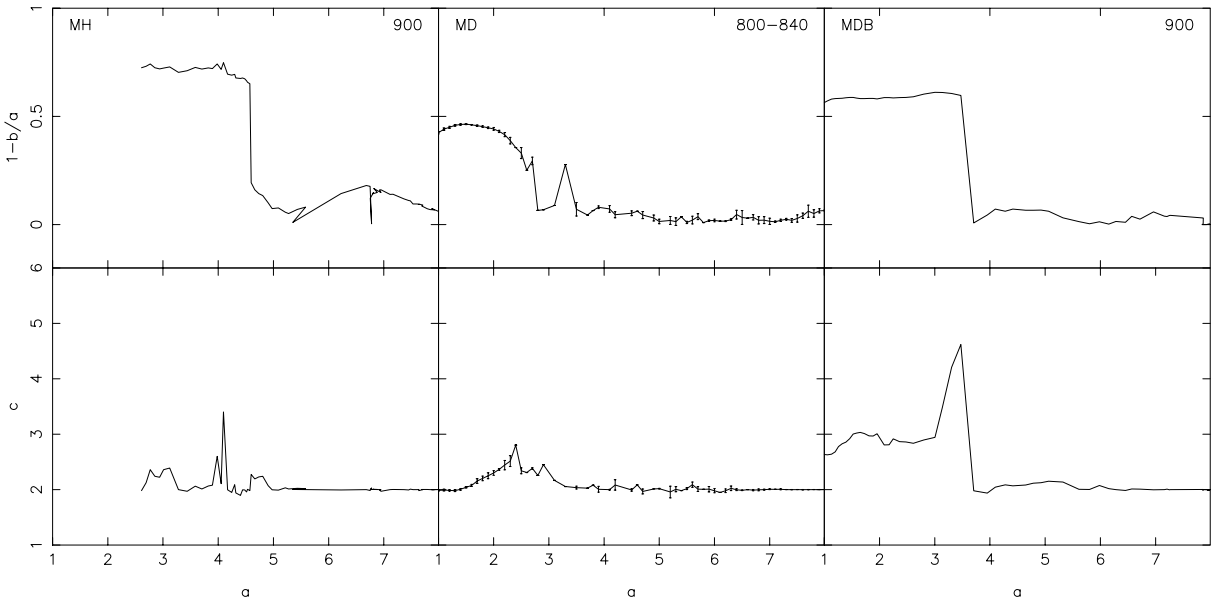

Figure 6.4: The upper panels show the run of the ellipticity 1 - b/a as a function of the semi-major axis a. The lower panels show the run of the shape parameter c, also as a function of a. The left panels corresponds to model MH, the middle ones to model MD and the right ones to model MDB. For reasons explained in the text we show for models MH and MDB the results at a given time, namely $t = 900$, while for model MD we give the average of a time interval, namely [780, 860]. The dispersion during that time is indicated by the error bars. The simulation name is given in the upper left corner and the times in the upper right corner of the upper panels.

both by the light of the bulge and that of the bar, it was necessary to blank out the inner parts of the galaxy, where the bulge light dominates. In a few cases there were also small spiral features starting off from the end of the bar, and these also had to be blanked out. Since the sample was relatively small it was possible to determine interactively the areas to be blanked out, separately in each frame.

Models MH and MD have no bulge, so it is possible to continue the fits much further in than in the case of early-type barred galaxies. (It is nevertheless recommended to exclude the innermost few pixels, where the shape of the pixel may influence the shape of the isophote). Comparisons with observations, though, will not extend all the way to the center. Model MDB has a sizeable bulge, but we fitted the generalised ellipses to the disc component only. We did this in order to be able to discuss the effect of the bulge on the real shape of the bar, rather than the shape of the disc and bulge components combined. This is trivial to do in the case of models, but of course impossible for real galaxies. We will discuss at the end of this section how the existence of the bulge obscures the issue when the generalised ellipses are fitted to both components, as is the case in real galaxies.

For every simulation and for every time step for which full information on the particle position is available – i.e. 45 time steps per simulation – we fitted generalised ellipses to 70 isodensities covering the density range in the disc. We repeated the exercise twice, once generously excluding a central region, and the other excluding only a very small central region. For reasons of homogeneity and seen the very large number of frames to be treated, we determined the area to be blanked out automatically and not interactively. For this we first took the difference of the projected density along the minor and major axes of the bar and calculated the radius at which this is maximum. In the first passage we excluded all the region within this radius, and in the second the region within one tenth of this radius. We made several tests with other blanking radii and thus asserted that our results are not dependent on this radius. Since the blanking out was done automatically we did not blank out the spirals coming from the ends of the bar. This presents problems in the early steps of the simulations, where the spirals are important and therefore influence wrongly the fits. In the later stages though, no such spirals are present, and the fits pertain to the bar only.

For models MD the generalised ellipses fit the isodensities very well all the way to the center, and thus the results obtained with the generous and with the limited blanking agree very well in the region where both give information. This is true also for most of the MDB and a large fraction of the MH cases. For some MH cases, however, the b/a values obtained with the two fits are in good agreement, but the c values are not. The reason is that the generalised ellipse is too simple a shape to fit properly the isophotes which have ansae or rectangular-like tips of the bar. In fact, for those cases, the shape enclosed by the isodensities is fatter around the major axis than what the generalised ellipse will allow. Thus the c value obtained by such a fit is not meaningful if the central parts have not been blanked out. This shortcoming was not clear for real galaxies, since there the inner parts are bulge dominated and thus were blanked out.

The upper panels of Figure 6.4 show the ellipticity, $1 - b/a$, as a function of semi-major axis a for our three fiducial models. For model MD we present the average of the five times in the time interval [780, 860] for which we have full information on all the particle positions. This was done in order to get a better signal-to-nose ratio, and was

possible because the axial ratio does not show any clear evolution with time. This is not the case for models MH and MDB, where evolution is present and we can not make averages without loosing information. These curves establish quantitatively the general impression we had already from Figures 6.2 and 6.3, namely that the bar in model MH is much thinner than that in model MD, the one in MDB being intermediate. Indeed the $(1-b/a)_{max}$ is 0.75, 0.44 and 0.69 respectively for models MH, MD and MDB. The run of the ellipticity with radius is also different in the three cases. For model MD the $1 - b/a$ rises to a maximum, occuring around $a = 1.9$, and then drops again. In many cases the drop after the maximum is more gradual than that shown in the Figure. This means that the isodensities are nearer to circular in the innermost and outermost parts of the bar and are more elongated in the intermediate region. For models MH and MDB the ellipticity curve is quite flat, meaning that the bar is thin even in the inner and outermost parts. After this flat region there is a very steep drop to a near-circular value. The value of a at which this drop occurs increases noticeably with time, so that making time averages would have smoothed out this feature considerably. Right after the steep drop there is a region with very low values of the ellipticity, after which the ellipticity rises again, albeit to a lower value. This intermediate low ellipticity region corresponds to the near-circular isophotes in the ring region, while the disc outside it has more elongated isophotes, their orientation being perpendicular to the bar, as expected. The disc of models MD and MDB outside the bar region has less elongated isophotes.

The lower panels of Figure 6.4 give, for our three fiducial models, the shape parameter c as a function of the semi-major axis a. This is less well determined than the axial ratio. One reason is that the value of c is much more sensitive to noise than the axial ratio, and our isodensities have significant noise since we have "only" 200 000 particles in the disc. A second reason, as argued above, is that in cases where the shape of the isodensity is not well described by a generalised ellipse the parameter c is more prone to error than the axial ratio b/a. Although individual profiles can show a number of spurious jumps, due mainly to noise, it is nevertheless possible to see that there are considerable differences between the three fiducial models. The form of this curve for model MD does not evolve with time, so we give here, as in the upper panel, the average of the five times in the time range [780,860], in order to increase the signal-to-noise ratio. We note that the value of c increases from a value around 2 in the center-most parts to a value around 3 for $a = 3.3$ and then drops again to a value near 2. This means that the isophotes are well fitted by ellipses in the center-most and outer parts of the bar, with a region in between with somewhat rectangular-like isophotes. The deviations from the elliptical shape, however, are never very pronounced. The shape of the c profile for model MH is very different. It has a sharp peak in the outer parts of the bar, after which the value of c drops abruptly. The maximum value is very high, around 5, but the region in which high values are seen is rather narrow. The value of a at which the c value drops sharply increases considerably with time, and for this reason we have not taken time averages, but present in Figure 6.4 only the values for $t = 900$. For model MDB the fits to generalised ellipses can extend to the innermost regions. Starting from the innermost parts we find first an extended region where c drops from over 3 to roughly 2, and then a very sharp peak of $c = 8.1$ at a radius of 3.9. The drop after the maximum is very steep. For model MDB, as for model MH, the value of a at which the maximum occurs increases with time.

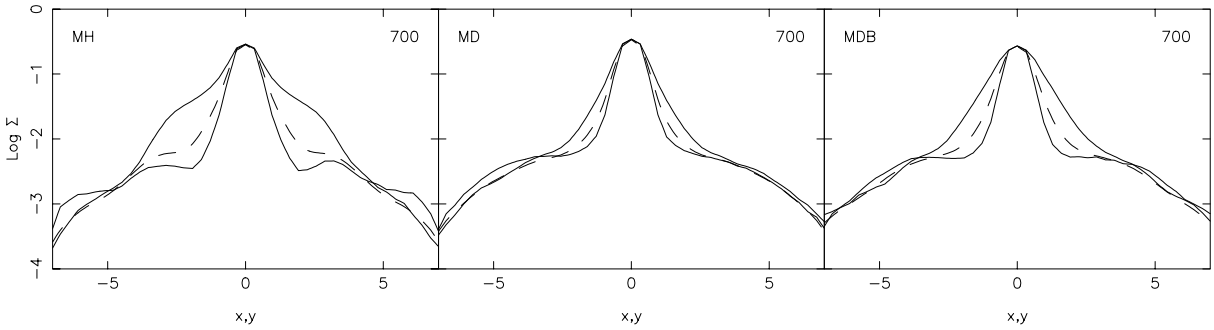

Figure 6.5: Projected density profiles along the bar major and minor axes (solid lines) and azimuthally averaged (dashed lines). The disc is seen face-on. The left panel corresponds to model MH, the middle one to model MD and the right one to model MDB. The simulation name is given in the upper left corner and the time in the upper right corner of each panel.

We repeated the exercise for model MDB, this time keeping both the disc and the bulge particles, in order to see what effect the inclusion of the bulge would have on the results. We find that the shape parameter c has considerably smaller values, in fact in between 2 and 3. Also the ellipticity drops, by something of the order of 0.1. Of course this value will depend on the density profile of the bulge, but the general trend should always be that including the bulge will make the isophotes nearer to ellipses and less eccentric.

The isophotes in the outermost disc region are also of interest, since they are often used by observers to deproject a galaxy, with the assumption that they are circular. In order to check whether this is a reasonable hypothesis we fitted ellipses to the outermost parts of the disc of our three fiducial models. We find that the deviations of the ellipticity from unity - i.e. of the isodensities from circularity - are less than 0.1 in the outermost parts. For model MH the slight elongation is perpendicular to the bar major axis, while for models MD and MDB it is along it. This may mean that for the latter two we are outside the outer Lindblad resonance, and for the former not. We will discuss this further in a future paper, after we have introduced the measurements of the pattern speed. Independent of the orientation of the outermost ellipses, their ellipticity is very near unity. Our fiducial models thus argue that it is reasonable to use the outermost disc isophotes to deproject an observed barred galaxy.

6.5 Density profiles along the major and minor axes of bars seen face-on

Figure 6.5 shows the projected density profiles along the minor and major axes of the bar of our three fiducial simulations at time $t = 700$. We note that the three sets of profiles differ significantly. For MD models the bar has along its major axis a fast decreasing profile, with a slope that is steeper than that of the outer disc. The MDB major axis profile resembles that of MD. On the other hand for MH models the profile has a flat part

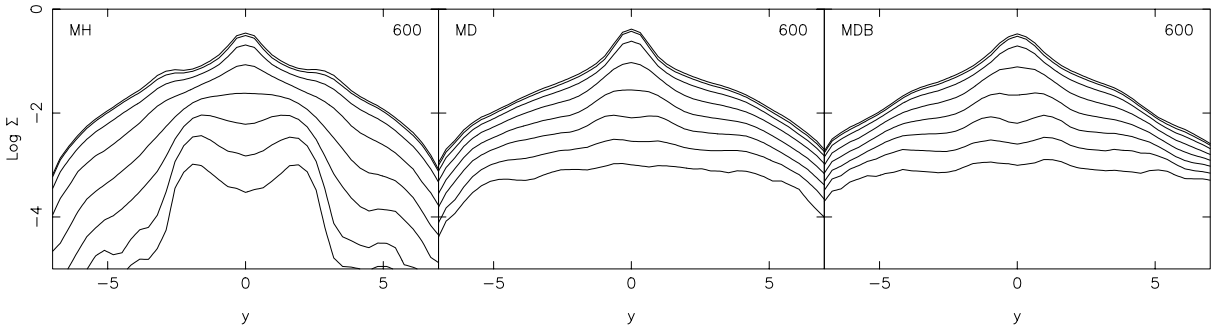

Figure 6.6: Projected surface density along cuts which are parallel to the major axis (the bar is seen side-on) at equidistant z values differing by $\Delta z = 0.2$. The uppermost curve corresponds to a cut at $z = 0$ and the lower-most one to a cut at $z = 1.4$. The left panel corresponds to model MH, the middle one to model MD and the right one to model MDB, all taken at time 600. The simulation name is given in the upper left corner and the time in the upper right corner of each panel.

followed by a relatively abrupt drop at the end of the bar region. MD bar profiles stay of the same shape all through the simulation, while the shape of MH profiles shows some evolution; their flatness shows clearest between times 540 and 740.

Model MH also shows a considerable density concentration in the innermost parts, well above the flat part. If such an enhancement was present in observations it would be attributed to a bulge component and this would have been wrong since we know that this simulation does not have a bulge. It is just an important central concentration of the disc component. It can also be present in models MD and MDB. Since, however, the bar has an exponential-like profile, it is not easy to disentangle the contribution of this component from that of the remaining bar. In this respect it is worth noting that the central projected surface density has roughly the same value for the three models.

The minor axis profiles of MD and MH models fall at considerably different rates. This, however, is not a new finding. It is just due to the fact that the MH bars are considerably thinner than the bars of type MD. In fact from the major and minor axis cuts alone one can get an estimate of the axial ratio of the bar at different isophotal levels, simply by drawing horizontal lines at given isophotal levels on plots like those of Figure 6.5 and measuring the radii at which the two profiles reach the given isophotal level.

6.6 Density profiles of bars seen edge-on

Let us now observe our three fiducial models edge-on with the bar seen side-on, i.e. with the line of sight perpendicular to the bar major axis. Figure 6.6 shows the projected density along cuts parallel to the major axis made at equidistant z values differing by $\Delta z = 0.2$. Again we note clear differences between the three models. For cuts which are offset from the equatorial plane of the galaxy, model MH shows a clear minimum at the center, followed on either side by a maximum, followed by a steep drop. This is the direct signature of the peanut, which is due to the minimum thickness in the center, followed

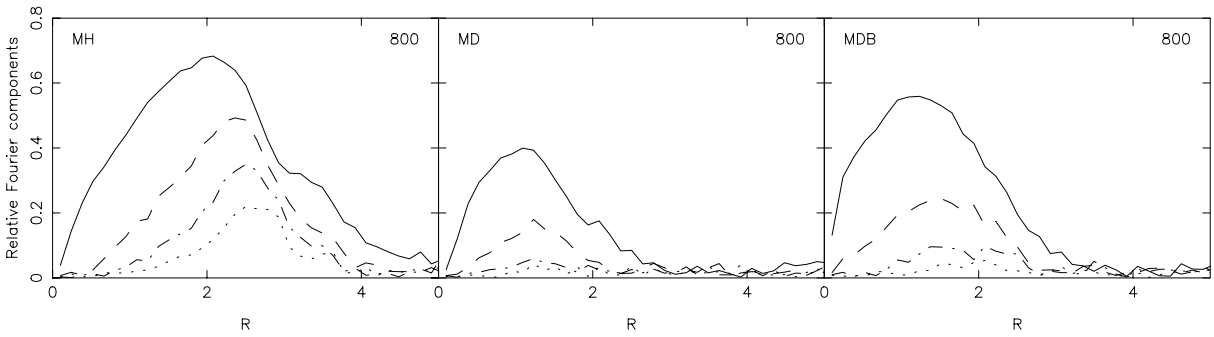

Figure 6.7: Relative amplitude of the $m = 2$ (solid line), 4 (dashed line), 6 (dot-dashed line) and 8 (dotted line) components of the mass or density. The left panel corresponds to model MH, the middle one to model MD and the right one to model MDB. The simulation number is given in the upper left corner and the time in the upper right corner of each panel.

by two maxima on either side. This is very clear in the three cuts which correspond to the highest z displacements, i.e. for z between 1.0 and 1.4. For models MD and MDB the peanut signature is much less pronounced. The profiles have, if any, a very shallow minimum at the center followed by a maximum nearer to the center than in model MH, visible in a rather restricted range of z displacements.

Another clear distinction between the MH and MD models is the form of the profile at $z = 0$. For model MH it shows clear ledges on either side of the peak, while there are no corresponding structures on the MD and MDB profiles. Thus for model MH at time 500 the ledge at $z = 0$ ends roughly at 2.9. These ledges can be found also on cuts somewhat displaced from $z = 0$, but disappear after the displacement has become too large, in this case $|z|$ of the order of 0.4. Similar values are found for time 800. The ratio of the maximum distance to which the ledge on the $z = 0$ cut extends to the radius of the very steep drop found on cuts offset from $z = 0$ is roughly 1.5.

The peak in the center is due to material that has accumulated in the central regions of the galaxy and is the edge-on analog of the corresponding density enhancement seen in the face-on profiles . This peak can be seen only on profiles near $z = 0$, and disappears once the displacement from the equatorial plane becomes sufficiently large, i.e. $|z| > 0.8$.

6.7 Fourier components of the face-on density distribution

Figure 6.7 shows the relative amplitude of the $m = 2$, 4, 6 and 8 components of the mass or density for our three fiducial cases. To calculate them we first projected the disc particles on the (x, y) plane and then obtained the Fourier components

$$A_m(r) = \frac{1}{\pi} \int_0^{2\pi} \Sigma(r, \theta) cos(m\theta) d\theta, \qquad m = 0, 1, 2, ... \tag{6.6}$$

and

$$B_m(r) = \frac{1}{\pi}\int_0^{2\pi} \Sigma(r,\theta) sin(m\theta) d\theta, \qquad m = 1, 2, ... \tag{6.7}$$

by dividing the surface into annuli of equal width $\Delta r = 0.14$ and calculating the A_m and B_m for each annulus. In practice instead of the surface density $\Sigma(r,\theta)$ we use the mass, but this comes to the same thing since we will be using only the ratios of the amplitudes $\sqrt{A_m^2 + B_m^2}/A_0$.

The maximum amplitude of the $m = 2$ component is biggest in the MH and smallest in the MD model, reflecting the fact that the bar in the MH model is the strongest and that in the MD model is the weakest of the three. Also in model MH the maximum occurs at a larger radius than in MD, and in general the region where this component is large extends to larger radii. This reflects the fact that, as seen in section 6.3, the bar in model MH is the longest and that in MD the shortest of the three. The most striking difference, however, between the three models concerns the higher order terms. Thus for the MD and MDB the $m = 6$ and $m = 8$ components basically stay within the noise, while in the MH model they are 44 and 27 percent of the $m = 2$ respectively. The relative importance of the $m = 4$ is also very different. It is 68, 34 and 55 percent of the $m = 2$ respectively in models MH, MD and MDB.

At time 500 the form of the curves is roughly the same as at 800. There is, however, a growth of the relative amplitude with time, which is quite strong for simulations MH, and exists also for MDB. Thus the maximum relative amplitude at time 500 is 0.56, 0.32 and 0.52 for models MH, MD and MDB respectively. Also the locations of the maxima of simulations MH and MDB move further out with time. At time 500 they are at $R = 1.4$, 1.4 and 1.2 respectively for the three models. Finally the secondary maximum occurring in simulation MH at larger radii – R somewhat less than 4 – is very pronounced at time 500 and is located at a smaller radius.

6.8 Length of the bar

Measuring the length of the bar is not unambiguous and several methods have been proposed so far. In order to apply them to our simulations we have had in certain cases to extend them or modify. Thus we have defined the length of the bar as follows:

1. From the value of the semi-major axis at which the ellipticity is maximum ($L_{b/a}$). One can use this value as such, or take a multiple of it. Here we adopted the former.

2. From the steep drop in the run of the ellipticity (or axial ratio) as a function of the semi-major axis (L_{drop}). As we saw in section 6.4, in model MH the ellipticity presents a steep drop towards the end of the bar region. Although this is not the case for model MD we will still use the radius at which the axial ratio shows the largest drop as a possible measure of the bar length, because it is a straightforward and direct method and it does not introduce any *ad hoc* constants. It could prove to be a good estimate for cases like model MH, where the drop is clear. It can unfortunately not be used blindly, since in some cases, as in model MD, there may not be a steep drop.

3. From the phase of the bar (L_{phase}). The phase of a perfect (theoretical) bar should be constant. This is of course only approximately true in N-body or observed bars. Nevertheless the phase varies little and the bar can be defined as the region within which the phase varies less than a given amount. Instead of considering the differences between the phases in two consecutive annuli, which may be heavily influenced by noise, we use a somewhat less local definition. We first calculate the phase of the $m = 2$ component of the whole disc, i.e. the phase of the bar. Then we repeat the exercise after slicing the disc in circular annuli. In the innermost parts the amplitude of the $m = 2$ is very low and the noise in the phase can therefore be important. Then there is a region where the phase is nearly constant and equal to the phase of the bar, and then it starts varrying with radius. We define as length of the bar the radius of the first annulus for which the phase differs by more than $asin(0.3)$ from the phase of the bar. The choice of the constant is of course *ad hoc*. It has simply been estimated so as to give reasonable results in a few test cases.

4. From the $m = 2$ component, or from the ratio of the $m = 2$ to the $m = 0$ components ($L_{m=2}$). In a model in which the disc does not respond to the bar, one would expect the end of the bar to be where all components except $m = 0$ go to zero. This is not true in N-body simulations and in real galaxies, where the disc responds to the bar and thus is not perfectly axisymmetric. One can, nevertheless, get an estimate of the bar length from the radius at which the relative $m = 2$ component is less than a given fraction of the maximum, provided there is no clear spiral structure. Here we will adopt as length of the bar the radius at which the relative $m = 2$ component reaches 20 per cent of its maximum value. Again the choice of the constant is *ad hoc*, estimated so as to give reasonable results in a few test cases.

5. From the face-on profiles (L_{prof}). We take the difference between the projected density profiles along the bar major and minor axes. This is of course zero at the center and increases with distance to reach a maximum and then drops. In a theoretical case of a bar in a rigid disc the end of the bar would be where the two projected density profiles became again equal. Since in N-body simulations the disc is responsive, the difference will not be zero even in the disc. We thus define as bar length the outer distance from the center at which the difference falls to 5 per cent of the maximum. Again the choice of the constant is *ad hoc*, estimated so as to give reasonable results in a few test cases.

6. From the edge-on profiles (L_{zprof}). We can define as length of the bar the distance of the end of the ledge on the $z = 0$ cut from the center of the galaxy.

7. From the ratio of the intensities in the bar and the inter-bar region (L_{Ohta} and L_{Agr}). Ohta *et al.* (1990) defined as bar region the zone with a contrast I_b/I_{ib} exceeding 2, where I_b and I_{ib} are, respectively, the bar and the inter-bar intensities. These can be simply defined as $I_b = I_0 + I_2 + I_4 + I_6$ and $I_{ib} = I_0 - I_2 + I_4 - I_6$. This criterion was modified by Aguerri *et al.* (2000) to delineate the region where $I_b/I_{ib} > 0.5[(I_b/I_{ib})_{max} - (I_b/I_{ib})_{min}] + (I_b/I_{ib})_{min}$. The length of the bar is then simply the outer radius at which $I_b/I_{ib} = 0.5[(I_b/I_{ib})_{max} - (I_b/I_{ib})_{min}] + (I_b/I_{ib})_{min}$.

This definition can be applied to N-body bars by changing the intensity for the density, so we will adopt it as one of our definitions. Contrary to other definitions it has the advantage of being applicable to analytic models, for which the length of the bar is known exactly. We have thus applied it to all models in Athanassoula (1992) and found in all cases an agreement of better than 4 per cent, except for the models with the very thin homogeneous bars, of axial ratio a/b larger than 4, where the error can reach 8 per cent.

Several of the above definitions are much easier to apply in N-body models than in real galaxies, since in the former we are sure to be in the equatorial plane of the disc, and thus we do not have the considerable uncertainties which a deprojection from the plane of the sky can bring to real galaxies. Most of them have been used in one study or another. Unfortunately they have never been applied all to the same case, so as to allow comparisons. For this reason we have applied them all to all simulations and to all time steps, and give the results for two times of our three fiducial simulations in Table 6.1. Since these estimates suffer from the existence of noise we have used an average over a given time range. This time range, however, should be rather small, since the length of the bar increases with time. Thus the σ given in the table is an overestimate of the real uncertainty, since it includes the effect of time evolution. The first column in Table 6.1 gives the name of the model, the second one the time range over which the average was taken and columns 3 to 9 give the estimates of the various methods. The second line in each case is similar, but contains the values of the dispersion. For the first two estimates ($L_{b/a}$ and L_{drop}) we use the ellipse fitting with the generous blanking (cf. section 6.4), since this is more generally applicable. Ohta's estimate is not adapted to our bars, so we do not include it in the Table. For the cases where the ellipticity is almost flat (like MH and MDB) $L_{b/a}$ is not meaningful, while for MD the ellipticity profile does not show a steep drop, so that L_{drop} is not well defined. Generally the largest values are given by L_{phase} and L_{prof}, and the smallest values are given by $L_{b/a}$ and L_{Agr}. L_{drop} and $L_{m=2}$ give generally estimates which are intermediate.

It is clear that the differences between the various methods are larger than the dispersions within each method. It is thus of interest to see which method, if any, gives the best results. For this in figures 6.8 and 6.9 we overlay on the isodensity curves taken at times 600 and 800 respectively, circles with radii the various estimates of the bar length. We note that there is no single method which fares well in all cases. For time 600 the best estimates are L_{drop} and $L_{m=2}$ for MH, L_{zprof} and L_{Agr} for MD, and $L_{b/a}$ and $L_{m=2}$ for MDB. For time 800 the best estimates are L_{zprof} for MH, L_{phase} for MD, and L_{drop}, L_{phase} and L_{prof} for MDB.

It is also interesting to see whether the average values represent the length of the bar well or not. Column 10 gives the average of all the estimates (L_1) in the first line and the standard deviation in the second. We also tried a second average (L_2) for which we omitted the entries which were considered unsafe. For this we rely on the applicability of the method to the models and not on whether they give results compatible with the visual estimates of the bar. For cases MH and MDB $L_{b/a}$ is meaningless, since the ellipticity profile is very flat. Similarly for model MD L_{drop} is unreliable since there is no clear drop in the b/a profile. For model MD there are two more estimates that could be unreliable.

Table 6.1: Length of the bar

model	Time	$L_{b/a}$	L_{drop}	L_{phase}	$L_{m=2}$	L_{prof}	L_{zprof}	L_{Agr}	L_1	L_2	LP_1	LP_2	LP/L_2
MH	540-660	2.9	3.4	4.1	3.4	4.3	2.9	2.6	3.4	3.4	1.7	1.9	0.5
MH	540-660	0.2	0.6	0.8	0.2	0.5	0.2	0.3	0.7	0.7	0.3	0.2	
MD	540-660	2.0	3.5	4.0	4.1	4.6	2.4	2.5	3.3	3.1	1.0	1.1	0.3
MD	540-660	0.1	1.6	1.6	0.2	0.3	0.5	0.2	1.0	1.1	0.1	0.1	
MDB	540-660	2.8	3.4	3.3	3.0	3.3	2.5	2.3	3.0	3.0	1.3	1.4	0.5
MDB	540-660	0.2	0.1	0.1	0.1	0.1	0.2	0.1	0.4	0.5	0.3	0.1	
MH	740-860	2.8	4.4	5.1	4.3	5.5	3.6	2.9	4.1	4.3	2.2	2.5	0.6
MH	740-860	0.2	0.1	0.9	0.4	0.5	0.1	0.1	1.0	1.0	0.0	0.1	
MD	740-860	2.1	4.3	2.4	4.1	4.4	2.1	2.3	3.1	2.7	1.0	1.2	0.4
MD	740-860	0.1	0.2	2.0	0.1	0.3	0.4	0.2	1.1	0.9	0.2	0.0	
MDB	740-860	3.3	3.9	3.7	3.4	3.8	2.9	2.6	3.4	3.4	1.5	1.7	0.5
MDB	740-860	0.1	0.1	0.1	0.1	0.1	0.1	0.1	0.5	0.5	0.1	0.1	

By examining the individual face-on profiles we see that the difference between the profile along the bar and perpendicular to it is not very dependent on radius (cf. Figure 6.5) and thus L_{prof} is badly defined. Finally the ledge is also not clear on the edge-on profiles, so that the L_{zprof} estimate is also unreliable. We thus omitted these two estimates as well for model MD[3]. L_2 and its standard deviation are given in the first and second line of column 11. Taking into account the error bars, we see that average values are good estimates of the length of the bar. This, however, is not a big help, since the error bars are rather large, particularly so for model MD.

Columns 12 to 15 contain information on the peanut length and will be discussed in the next section.

6.9 Quantifying the peanut shape

From the third row of panels of Figures 6.2 and 6.3 we can see that simulation MDB and the earlier time of simulation MH show a clear peanut shape, simulation MD is boxy, while in the later times simulation MH has clear X signature. In this section we will make this comparison more quantitative. We explore two different ways of quantifying the peanut shape.

The first relies on cuts parallel to the major axis when the galaxy is observed side-on, as introduced in section 6.6. From such cuts the strength of the peanut can be parametrised by

$$SP_1 = \Sigma_{max}(y, z_{ref})/\Sigma(0, z_{ref}), \tag{6.8}$$

[3]In fact the ledge is also difficult to see for model MDB up to time 620. So a more careful treatment would omit this estimate for part of simulation MDB.

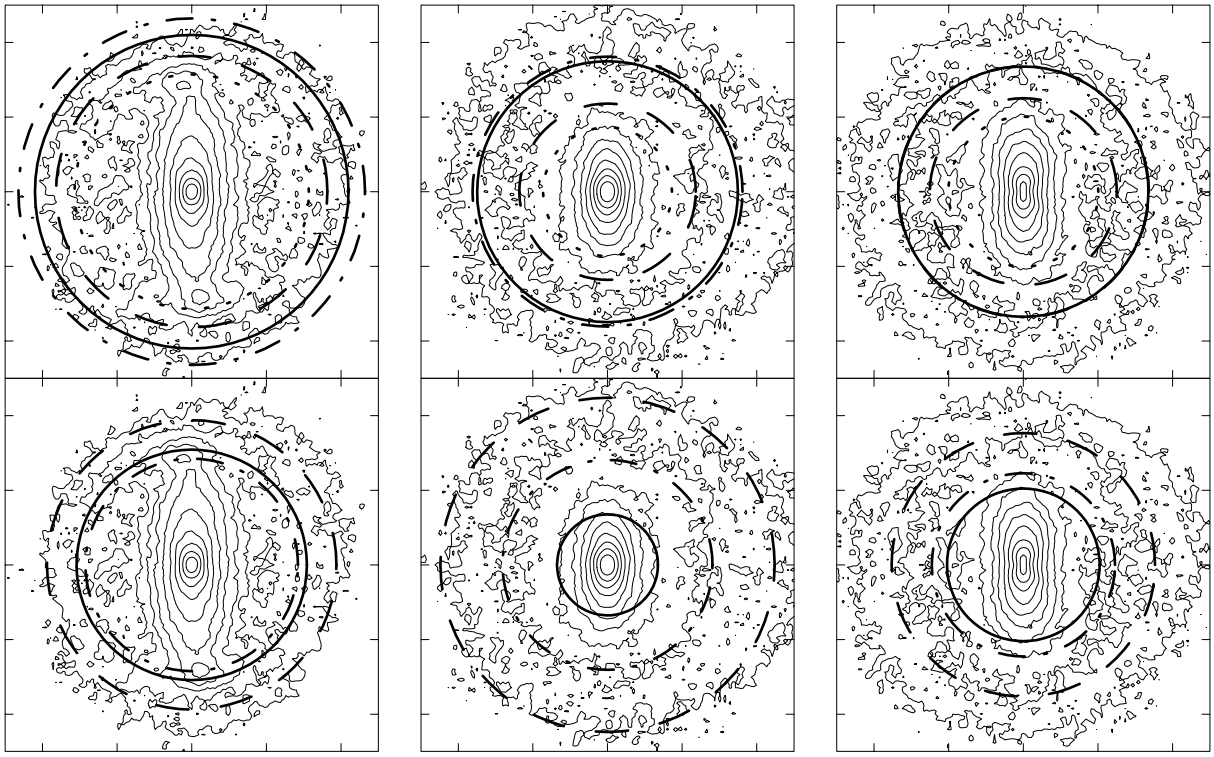

Figure 6.8: The main determinations of the bar length superposed on isocontours of the projected density for the disc component. In the upper panel we give L_{phase} (solid line), $L_{m=2}$ (dashed), L_{prof} (dash-dotted) and L_{Agr} (dotted). In the lower panel we give $L_{b/a}$ (solid line), L_{drop} (dashed) and L_{zprof} (dash-dotted). The name of the simulation is given in the upper left corner of the upper panels. The isocontours correspond to the time given in the upper right corner. The bar length estimates are obtained by averaging the results of seven times, centered around the time given, and spaced at equal intervals of $\delta t = 20$, as in Table 1. The length of the tick marks is 2 computer units.

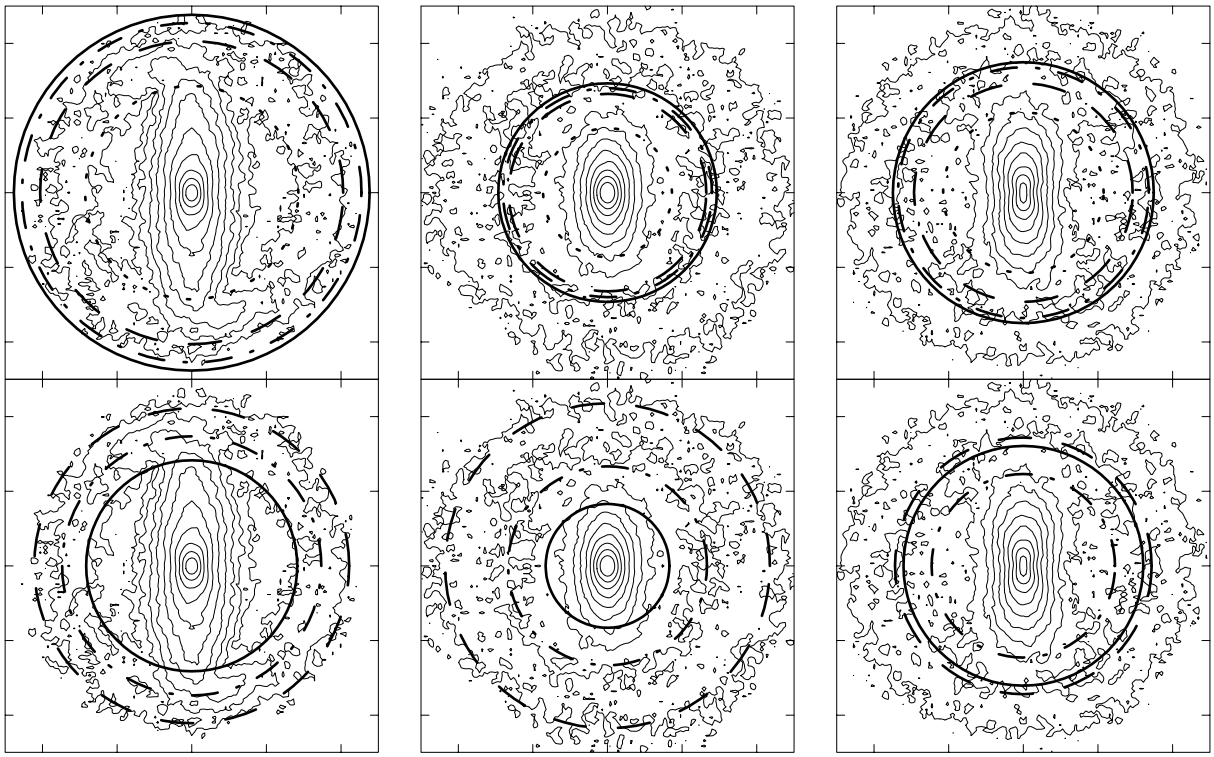

Figure 6.9: Same as the previous figure, but for time 800.

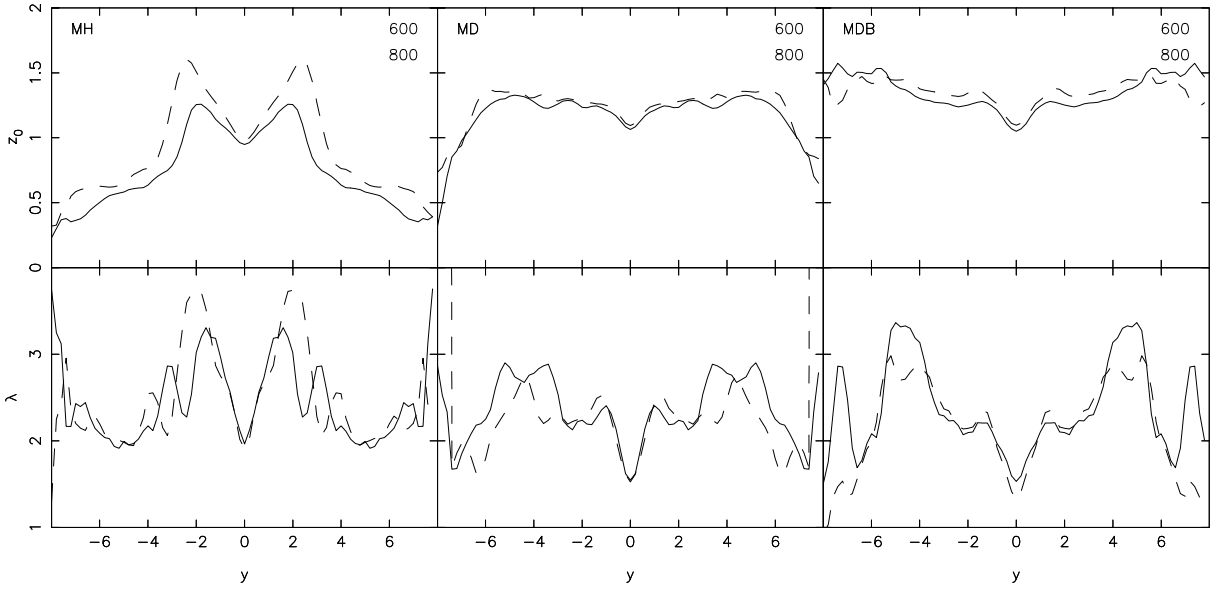

Figure 6.10: Parameters z_0 (upper panels) and λ (lower panels) of the generalised gaussian fitting best cuts parallel to the z axis. The left panels correspond to model MH, the middle one to model MD and the right one to model MDB. The name of the simulation is given in the upper left corner and the times in the upper right corner of the upper panels. The solid line corresponds to time 600 and the dashed one to time 800.

where y the distance from the center along the cut, z_{ref} is the z value at which this cut is made, $\Sigma(y, z_{ref})$ is the projected density along the cut, Σ_{max} is the maximum value of the density along the cut and $\Sigma(0, z_{ref})$ is the value at the center of the cut. The value of SP_1 is heavily dependent on the value of z_{ref}. For too low a value of z_{ref} the peanut strength is not well revealed, while for too high a value $\Sigma(0, z_{ref}) = 0$, and therefore the above definition is not applicable. We have chosen $z_{ref} = 1$, which we believe is a reasonable compromise. Such cuts can also tell us the radial size of the peanut, defined as the value of y for which $\Sigma(y, z_{ref})$ is maximum. This also depends on z_{ref}. It increases strongly with z for small values of z and less so for larger z values. We choose as our first measure of the peanut length L_{P1}, the value of y for which $\Sigma(y, 1)$ is maximum.

Applying this definition to model MH we get $SP_1 = 5.5$ for time 600 and $SP_1 = 12$ for time 800. The corresponding lengths of the peanut are $LP_1 = 1.7$ and $LP_1 = 2.2$ correspondingly. For model MDB we get for SP_1 and time 600 (800) the value of 2.2 (3.0), and for model MD the value 1.5 (1.2). For the latter model the minima and maxima, and therefore the values of the peanut length, are poorly defined, showing that the form is more a box than a peanut.

For the second method we "observe" our models side-on and make cuts parallel to the z axis at different values of y. For each cut we make a profile of the projected surface density as a function of z. We symmetrise the profiles with respect to $z = 0$, fit to them generalised gaussians of the form $exp(-(z/z_0)^\lambda)$ and thus determine the values of z_0 and λ for which the generalised gaussian fits best the profile. Larger values of z_0 correspond to broader gaussians, while the parameter λ defines the shape of the generalised gaussian. For $\lambda = 1$ the generalised ellipse becomes an exponential and for $\lambda = 2$ a standard gaussian. For small values of λ the generalised gaussian is very peaked at the center and for large ones it has a relatively flat top.

Figure 6.10 shows the values of z_0 and λ as a function of the y value at which the cut was made. Since the results are relatively noisy we apply a sliding means. For model MH z_0 shows a clear minimum at $y = 0$ followed by a clear maximum. This is a signature of a peanut. Thus our second way of quantifying the peanut is from the ratio of the maximum of z_0 to its value at the center, namely

$$SP_2 = z_{0,max}/z_0(0). \tag{6.9}$$

This is 1.3 (1.8) for times 600 (800) and model MH. For model MD, the value of SP_2 at time 600 (800) is 1.1 (1.1), and for model MDB 1.2 (1.3). From these and a number of other cases we can see that SP_2 can distiguish well between shapes which are boxy, where it gives values hardly above 1, peanuts, where it gives larger values, and X shapes, where it gives considerably larger values. It can thus be used as a measure of the box/peanut/X strength.

The location of the maximum of z_0 can be used as a measure of the radial extent of the peanut (LP_2). We find $LP_2 = 2.0$ (2.6) for time 600 (800). The results for the peanut length obtained with the two above definitions averaged in the [540, 660] and [740, 860] time ranges are listed in columns 13 and 14 of Table 6.1. The agreement between the two results is of the order of 10 per cent, except for the later time of model MD, where the difference is 20 per cent. We can thus consider either of them, or their average, as a reliable estimate of the peanut length. They show clearly that the radial extent of the

peanut increases considerably with time. We also calculated the ratio of the peanut length (as the average of the two estimates) to the bar length (L_2) and give it in the last column of Table 1.

The parameter λ also shows a minimum in the center surrounded by two maxima, one on either side. This does not necessarily imply that it can be used as a measure of the peanut strength or length. Indeed the shape of the gaussians need not correlate with their width.

A different parametrisation, based on the a_4 parameter (Bender *et al.* 1989) often used for elliptical galaxies, will be discussed in a future paper in collaboration with M. Bureau.

6.10 Rotation

The orbits of particles in a barred galaxy are far from circular, and this of course reflects itself on the galaxy velocity field. Figure 6.11 shows the velocity fields of our three fiducial models. It is obtained in a way that varies somewhat from that of observations, yet it is the most convenient for comparing with observations of galaxies at intermediate inclinations, for which the contribution of the z component of the velocity is relatively small. To obtain it we project all particles on the equatorial plane, observe their v_y velocity component and plot the corresponding isovelocities. For the three views shown in the figure this is equivalent to observing along the bar major axis, at 45 degrees to it and along the bar minor axis, respectively.

Model MD gives velocity fields analogous to those given by previously published models. When we observe along the bar major axis, the isovelocities show a characteristic concentration towards the central region, due to the fact that particle orbits are elongated along the bar and the velocity along an orbit is larger at pericenter than at apocenter. The intermediate angle velocity field shows the Z structure characteristic of barred galaxy velocity fields (see e.g. Peterson *et al.* 1978, for NGC 5383), and finally the velocity field obtained when we view along the bar minor axis shows a sizeable area of solid body rotation in the inner parts.

Several of these features are seen also in the case of model MH, but with some notable differences. Thus when we observe along the bar major axis we note a strong pinching of the isovelocities in the innermost region, on or near the bar minor axis. For the 45 degrees orientation the Z shape is much more pronounced than in the MD case, which could be expected since the bar in model MH is so much stronger. The greatest surprise, however, comes from the last orientation, where we view the disc along the bar minor axis. The innermost solid body rotation part is there, as for model MD. But as we move away from the kinematical minor axis the isovelocities show a clear wavy pattern, indicating that the mean velocities is lower at the ends of the bar than right above or right below that. This is due to the fact that near the ends of the bar the particles are at their apocenters. The mean velocities in those regions can be further lowered if the corresponding periodic orbits have loops at their apocenters. Athanassoula (1992) discusses such loops, and the regions where they appear in her models correspond roughly to the low velocity regions discussed here. She also shows that such loops occur mainly in periodic orbits in strong bars, i.e.

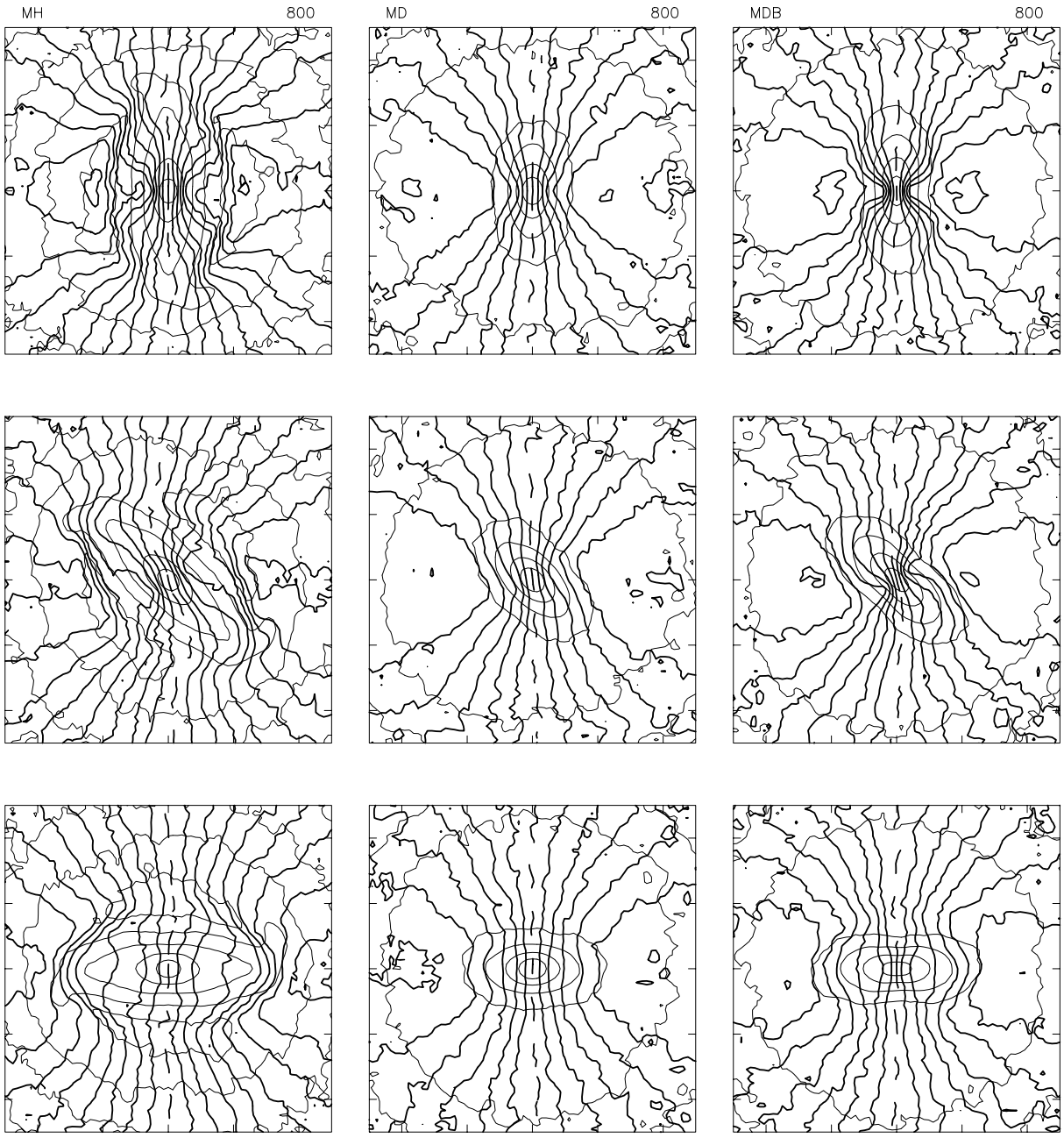

Figure 6.11: Velocity field of the disc, for three different orientations of the bar: along the y axis (upper panels), at 45 degrees to it (middle panels), and along the x axis (lower panels). The isovelocities are given by thick lines and the kinematic major axis, i.e. the isovelocity corresponding to the systemic velocity (in our case zero), with a dashed line. The Δv between two consecutive isovelocities is 0.1. We also overlay the isodensities with thin line contours. The line of sight is along the y axis. The left panels correspond to model MH, the middle ones to model MD and the right ones to model MDB, all at time 800.

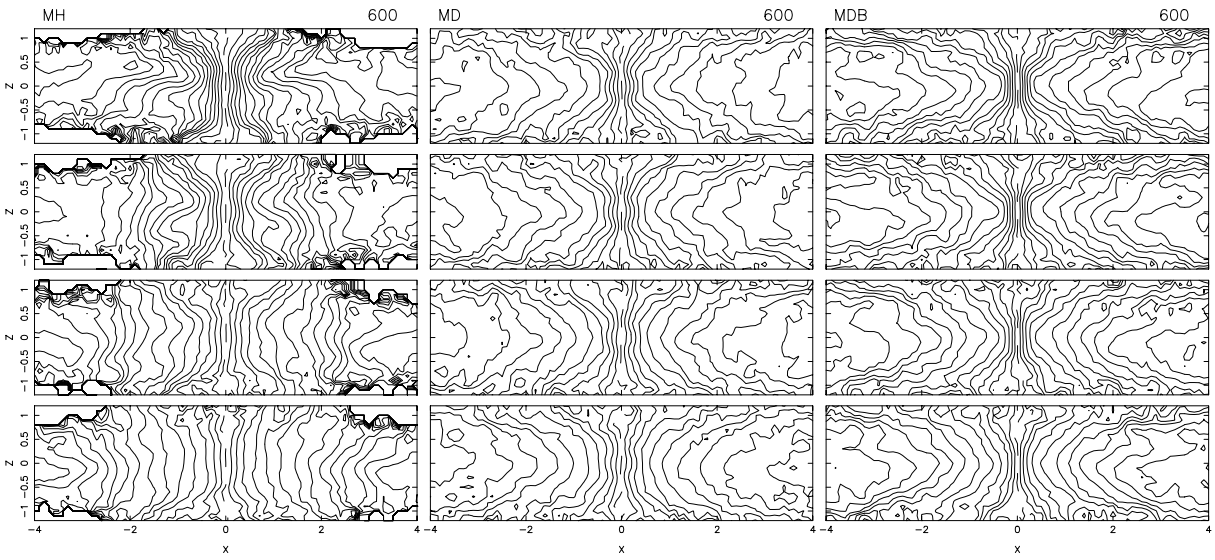

Figure 6.12: Velocity field of the three fiducial discs seen edge-on, for four different orientations of the bar: end-on (upper row), at 30 degrees to the line of sight (second row), at 60 degrees to the line of sight (third row) and side-on (fourth row). The kinematic major axis is given by a dashed line. The left panels correspond to model MH, the middle ones to model MD and the right ones to model MDB, all at time 500.

that such loops are more liable to be found in model MH than in model MD. A more quantitative comparison will have to wait for a complete study of the orbital structure in these models, which should furthermore elucidate the formation and properties of the ansae. Let us also note here that the velocity field is that of a stellar component and should not be compared to those obtained by observing the gas or from hydrodynamical simulations.

The velocity field of model MDB is intermediate of those of models MH and MD. This holds both for the Z pattern seen in the 45 degrees orientation and the wavy pattern at the ends of the bar when we view along the bar minor axis. The central crowding, however, is more important than in models MD and MH. This is due to the extra central concentration of the bulge component.

Let us note in passing that no velocity gradients are seen along the line of sight when that coincides with the major or the minor axis of the bar. Furthermore, hardly any velocity gradient can be seen in the MD and MDB cases, even when the line of sight is at 45 degrees to these axes. Thus the existence of a velocity gradient along the minor axis is not a very good criterion to picking out bars and oval distortions and should be left for cases where only limited information along slits is available. If a 2D velocity field is available one should rather look at whether the kinematical major and minor axes are orthogonal to each other (cf. e.g. Bosma 1981 for a discussion) and at the twists of the isovelocity contours.

Figure 6.12 shows the velocity field that is obtained when the disc is seen edge-on, for four different angles of the bar with respect to the line of sight, for models MH, MD and MDB respectively. Again there are important differences between models MH and

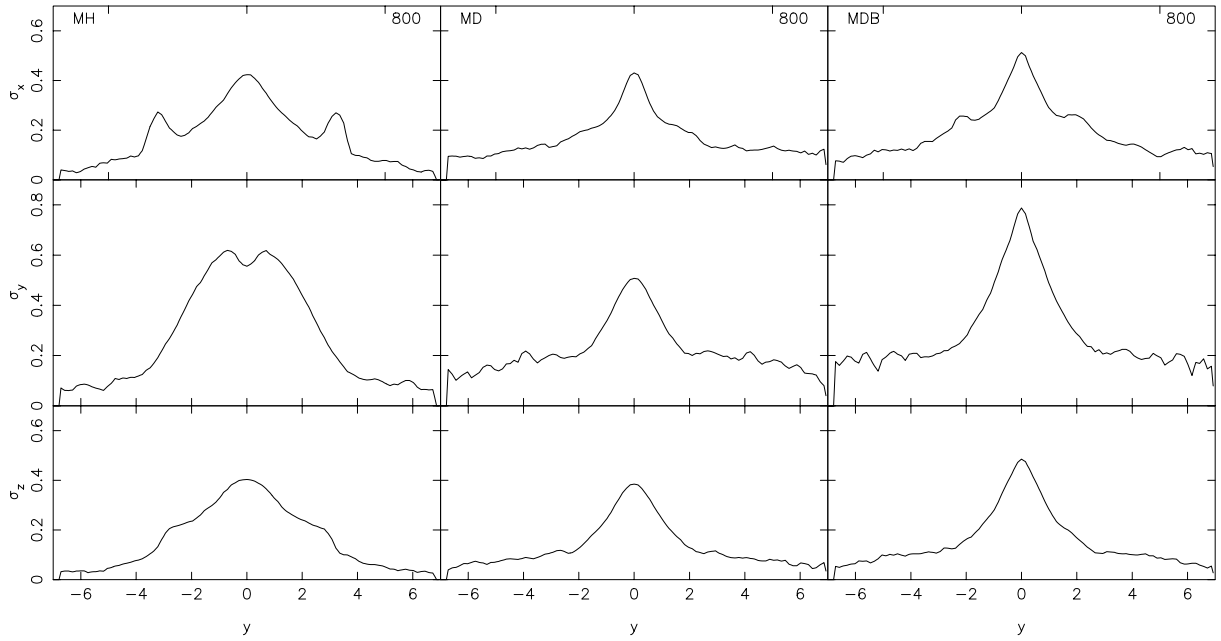

Figure 6.13: Velocity dispersion as a function of distance from the center for our three fiducial models at time 800, as discussed in section 6.11. The components σ_x, σ_y and σ_z are shown in the upper, middle and lower panels respectively. The left panels corresponds to model MH, the middle ones to model MD and the right ones to model MDB. The simulation name is given in the upper left corner and the time in the upper right corner of the upper panels.

MD. For model MH the mean rotation does not depend on the the distance z from the equatorial plane in a central region, whose size depends on the orientation of the bar. Perpendicularly to the equatorial plane it extends roughly as far as the bar material extends. The distance along the equatorial plane is smallest when the bar is seen end-on and biggest when the bar is seen side-on. In the latter case it extends over most of the area covered by the peanut. On the other hand in the MD model the mean rotational velocity drops considerably with increasing distance from the equatorial plane, thus again providing a clear dichotomy between the two fiducial cases. Model MDB has a velocity field similar to that of model MD.

As already discussed, the form of the MH bar viewed side-on evolves from box-like to peanut and then to X shaped. When it reaches this last stage the area within which the rotation does not depend on z is somewhat less extended, particularly in the low density areas on and around the z-axis, on either side of the center.

6.11 Velocity dispersions of a thin strip of particles taken along the bar major axis

In order to get more information on the motions in our fiducial models we have isolated a strip of particles centered on the bar major axis and having a width of 0.07. Figure 6.13

shows the three components of the velocity dispersion, σ_x, σ_y and σ_z, as a function of the distance from the center of the galaxy measured along the strip, at time 800. The σ_x for model MH shows two sizeable maxima, one at either side of the center. They should be due to the form of the x_1 orbits in that region, either to the loops that these orbits can have on the major axis, or to their more rectangular like shape, and will be discussed in those terms in a future paper, where the orbital structure of these models will be presented. Here we will note that the shape of the isophotes in that region is very rectangular-like for model MH. The σ_x for model MDB also shows two similar maxima, of relatively lower amplitude. This model also has bar isophotes with a rectangular-like shape, but the maximum rectangularity occurs at larger distances from the center than the secondary maxima of the σ_x profile. No such maxima can be seen for model MD.

The central value of all three components for model MDB are much larger than those of the other two models, presumably due to the presence of the bulge. This is particularly clear for the σ_y component. Also the velocity dispersions are large over a more extended region in model MH than in model MD. This can be easily understood by the fact that the size of the bar is larger, and that the velocity dispersions are larger within the bar region.

It is also worth noting that the σ_y component for model MH has a minimum at the center, surrounded by two low maxima close to it and on either side of the bar, and followed by a quasi-linear drop. This is not the case for models MD and MDB, where the maximum velocity dispersion is reached at the center. Again the explanation of this in terms of orbits will be discussed after we present the orbital structure in each model.

6.12 The bulge

We used the inertia tensor to obtain information on the shape of the bulge. For this we first calculated the local density at the position of each bulge particle, using the distance to its six nearest neighbours (Casertano & Hut 1985) and then sorted the bulge particles in order of increasing local density. We believe that the density is more appropriate than the radius – which introduces a circular bias – or than the binding energy – which also introduces such a bias, albeit much less than the radius. We then discarded the 10 per cent in the most dense environment, part of which could be influenced by the softening, and the 10 per cent in the least dense environment, which contains particles at very large distances from the center, divided the remaining particles into five groups of equal mass and calculated the eigenvalues and eigenvectors of the inertia tensor separately for each group and then for the five groups together. The axial ratios can then be obtained (e.g. Barnes 1992) as those of the homogeneous ellipsoid that has the same moment of inertia. We thus obtain

$b_b/a_b = \sqrt{q_2/q_1}$

and

$c_b/a_b = \sqrt{q_3/q_1}$

where a_b, b_b and c_b are the lengths of the three principal semi-axes of the bulge, and q_1, q_2 and q_3 are the eigenvalues of the inertia tensor.

When considered as a whole, the bulge of the fiducial MDB model is an oblate object, with the shortest dimension along the z axis, i.e. perpendicular to the disc plane. The value of c_b/a_b is around 0.9. However, when we consider each group of particles separately, the departure from sphericity can be much more important. Thus the group with the highest densities, which has a mean distance from the center of 0.3, is somewhat triaxial with axial ratios roughly 0.75 and 0.7 respectively. The median group, with a mean distance from the center of 1.2, has axial ratios of roughly 0.9 and 0.8 respectively. In general, as we go from highest to lowest densities, the shape becomes gradually more spherical.

6.13 Summary and discussion

In this paper we present three simulations of bar unstable disc galaxies. Initially in the first model, MH, the halo mass is concentrated in the inner parts, while in the second one, MD, it is the disc mass that dominates in the central parts. The third model, MDB, is similar to model MD, but has also a bulge of mass 60 per cent of the disc mass. In all three cases the halo mass is about five times the mass of the disc. All three models evolve and form a bar in their central parts. The properties of the bar, however, are very different in the three cases.

Model MH forms a very strong bar, which is long and thin when viewed face-on. It is surrounded by a massive inner ring, slightly elongated along the bar. Seen edge-on the galaxy has a peanut or X shape. This model has initially no bulge, so the particles forming the peanut are disc particles, or, more precisely, bar particles. It is thus not appropriate to call this component a bulge, as is often done. This is not, however, the only way that we could have attributed material to a bulge in this bulge-less galaxy. When seen end-on the disc material has a definite central spheroidal concentration, extending well out of the plane, which could easily be mistaken as a bulge sticking out of an edge-on disc galaxy. Surface photometry will only enhance this impression. Projected density profiles, obtained both from face-on and edge-on views, show clear central concentrations in the inner part, which would again easily be attributed to a bulge.

The bar of model MH is not only strong and long, but it is also thin and rectangular-like, as we could show by fitting generalised ellipses to the isophotes. The rectangularity is particularly strong in the outer parts of the bar. Within the main bar region the ellipticity of the bar isophotes does not change much with distance from the center, and then it drops abruptly to near-circular in the ring region. Outside the ring the isophotes become somewhat more elliptical shaped and are oriented perpendicular to the bar. At sufficiently large distances from the center they are again near-circular. Thus even in this very strongly barred case the ellipticity of the outer disc isophotes is sufficiently low for observers to be able to consider them circular and use them for deprojecting.

For model MH the projected surface density profiles, obtained from cuts along the bar major axis of the galaxy viewed face-on, show a flat region on either side of the central concentration, the end of which can be used as a measure of the bar length. Similar profiles, now from the galaxy seen edge-on, also show this characteristic ledge. Cuts which are offset from the equatorial plane and parallel to the bar major axis reveal a

two-horned shape, characteristic of a peanut. They can be used to parametrise the length and the strength of the peanut.

We also Fourier analysed the face-on density distribution of the disc particles. We find that the $m = 2$ component is quite large, between 0.6 and 0.8 for the times we discuss here. The position of the maximum is well within the bar; half or a quarter of the way to the center. Nevertheless the $m = 2$ component is important all through the bar region. The relative amplitudes of the higher m components are smaller than that of the $m = 2$, but are still very big. Even $m = 8$ is of the order of one third of the $m = 2$. The distance of the location of the maximum of the relative amplitude from the center increases with m.

The velocity field also shows very strong deviations from circular motion, due to the presence of the bar. When the line of sight is along the bar major axis, or at 45 degrees to it we observe crowding of the isovelocities in the center-most areas. The 45 degrees orientation shows very clearly the strong Z-type isovelocities, classical of barred galaxies. When the line of sight is along the bar minor axis the isovelocities passing near the ends of the bar show a strong wavy form. This is due to the low mean velocities in the end of the bar region.

When viewed edge-on the model exhibits strong cylindrical rotation over a large area. The bar signature is also clear in the velocity dispersions, which are high in all the bar region. The component perpendicular to the bar major axis shows clear local maxima around the ends of the bar. The component parallel to the bar major axis shows a shallow minimum or a plateau at the center.

The bar in the MD model is quite different. It is considerably shorter, thicker and less rectangular-like than the MH bar. Viewed edge-on it has a form which is better described as boxy. Its projected density profiles decrease steeply with radius in the bar region and that both in the face-on and edge-on view, as opposed to the flatter profiles of the MH bar. The relative amplitude of the $m = 2$ component is less than 0.4, and the $m = 6$ and 8 components are negligible. The relative $m = 4$ component is considerably smaller than the relative $m = 8$ component of the MH model. Viewed edge-on model MD does not display cylindrical rotation.

Finally, model MDB has a bar which is intermediate in length and shape to that of the previously discussed two models. Viewed edge-on it has a peanut shape, which never evolves to an X shape, at least within the times considered here. Its projected density profiles, both for the face-on and the edge-on viewing, as well as its velocity field are intermediate of those of models MH and MD. In the face-on profiles there is more difference between the major and the minor axis profiles than in the MD case. On the other hand there is no flat part, except perhaps at the very late times of the evolution, where such a structure starts to form.

In all three cases the formation and evolution of the bar is followed by a substantial inflow of disc material towards the central parts. This implies qualitative changes for model MH. Indeed at the initial times the halo contribution is somewhat larger than the disc one in the inner parts. The halo density distribution does not change much with time, while the disc becomes considerably more centrally concentrated. Thus at latter times the disc dominates within the central region, to a distance larger than an initial disc scale length. For the MD and MDB spheroids also the density distribution does not change

much with time, and again the disc component becomes more centrally concentrated. Thus the central areas become even more disc dominated than they were at the beginning of the simulation. The difference, however, is quantitative, rather than qualitative, as it was for the MH model.

We used a number of different ways of measuring the bar length. Some of them are more suited for MH type models, others for MD types, while others can be used for both. Unfortunately we could not find any criterion which could do well for all simulations and all times. Average values give satisfactory estimates within their error bars, but their error bars are rather large. This will prove to be a major problem when we will want to compare the length of the bar to the corotation radius, to see how evolution affects this ratio and whether it stays compatible with observational limits (cf. Debattista & Sellwood 2000).

We also introduced two ways of measuring the strength and length of the peanut. They allow to distinguish between boxy, peanut-shaped and X-shaped outlines. They also show that the length of the peanut is considerably shorter than the length of the bar.

Acknowledgments. We would like to thank A. Bosma for useful discussions and J. C. Lambert for his help with the GRAPE software and the administration of the simulations. We would also like to thank the IGRAP, the Region PACA, the INSU/CNRS and the University of Aix-Marseille I for funds to develop the GRAPE computing facilities used for the simulations discussed in this paper. Part of this paper was written while one of us (E.A.) was visiting INAOE. She would like to thank the ECOS-Nord and the ANUIES for financing this trip and INAOE for their kind hospitality.

Bibliography

Aguerri J.A.L., Muñoz-Tuñón C., Varela A.M., Prieto M., 2000, A&A, 361, 841

Athanassoula E., 1992, MNRAS, 259, 328

Athanassoula E., Bosma A., Lambert, J.C. & Makino J., 1998, MNRAS, 293, 369

Athanassoula E., Morin, S., Wozniak, H., Puy D., Pierce M.,

Lombard J. & Bosma A., 1990, MNRAS, 245, 130

Bosma A., 1981 AJ86 1825

Barnes J. E., 1992, ApJ, 393, 484

Bender R., Surma P., Döbereiner S., Möllenhoff C., Madejsky R., 1989, A&A, 217, 35

Casertano, S., Hut, P., 1985 ,ApJ, 298, 80

Debattista V.P., Sellwood J.A., 2000, ApJ, 543, 704

Hernquist L., 1993, ApJS, 86, 389

Kawai, A., Fukushige, T., Makino, J., Taiji, M., 2000, PASJ, 52, 659

Kawai, A., Fukushige, T., Taiji, M., Makino, J., Sugimoto, D., 1997, PASJ, 49, 607

Kent, S., 1986, AJ, 91, 1301

Kormendy J., 1983, ApJ, 275, 529 Lütticke, R., Dettmar, R.-J., Pohlen, M. 2000, A&A, 362, 435

Ohta K., Hamabe M., Wakamatsu K., 1990, ApJ, 357, 71

Peletier R.F., Balcells M., 1996, AJ, 11, 2238

Peterson C.J., Rubin, V.C., Ford, W.K., Thonnard, 1978, ApJ, 219, 31

Toomre A., 1964, ApJ, 139, 1217

6.14 Appendix. Initial conditions

In order to generate the initial conditions of our simulations we widely followed the method described by Hernquist (1993), with the following small differences:

1. For the radial velocity dispersion Hernquist (1993) adopts $\sigma_R^2(R) = Cexp(-R/h)$, where the constant C is normalized so that the Toomre Q parameter (Toomre 1964) has a prescribed value at a given radius. One technical problem with this choice is that the central parts may be very hot, making the epicyclic approximation, on which the calculation of the asymmetric drift and of the azimuthal velocity dispersion is based, totally inadequate. A second problem is that, for certain choices of C and of the reference radius, the disc may turn out to be locally unstable at certain radii. As an alternative we have adopted a Q that is constant all through the disc. This also has some technical problems, but we found them to be less severe than those of Hernquist's choice. Namely in cases with strong bulges one has to take care that the forces are properly calculated in the central parts of the disc before obtaining the epicyclic frequency (see also point iii below). Even so, in difficult cases, it is possible that the streaming velocity becomes larger than the circular velocity. In such cases we artificially lower the value of the streaming velocity to the value of the circular velocity.

2. In Hernquist's method, the velocities of the halo particles are drawn from a gaussian whose second moment is the velocity dispersion of the halo distribution at the radius under consideration. While a gaussian is the most natural choice, it has the inconvenience of extending to infinity. Thus particles are often drawn with velocities larger than the escape velocity. To avoid this we have used another function, namely :

$$F(v,r) = \begin{cases} C_1 \left(1 - \frac{v_i^2}{C_2^2}\right) & v_i \leq C_2 \\ 0 & v_i > C_2 \end{cases}$$

   where v_i is the x, y, or z component of the velocity and the constants C_1 and C_2 are calculated so that the zeroth and second moments are the same as those of the gaussian. This function limits the values of the velocity components to the interval $(-C_2, C_2)$. While it is still possible for some particles to be drawn with velocities larger than the escape velocity, their number is significantly smaller than in the case of the gaussian.

3. In order to calculate the epicyclic frequency we need first to calculate the force on the disc particles, and for that we used direct summation, including the softening. This allows a more accurate determination of the forces, particularly in the central parts of models with bulges. In fact Hernquist (1992) does not give sufficient information on how he calculates the force, so we can not be sure that this is indeed a difference between his method and ours.

6.15 Appendix. Measuring the mass, radius and axial ratio of the ring

We developed two different, independent, methods of fitting a ring and obtaining its basic parameters. In the first we fit a single function $I(R,\theta)$ simultaneously to most of the face of the galaxy. We first exclude the regions with $R < 1$, as they do not contain information relative to the ring, and the regions where $cos(\Delta\phi) < 0.5$, where $\Delta\phi$ the azimuthal angle measured from the major axis of the bar, since there the ring does not detach itself sufficiently well from the inner part of the profile to allow an accurate fit. To the remaining part we fit a function

$$I(R,\phi) = C_0(\phi)\ R^{-C_1(\phi)} + \\ C_2(\phi)\ exp(-(R - C_3(\phi))^2/C_4(\phi)^2)\ ,$$

where $C_i(\phi) = P_{2i} + P_{2i+1}cos(2\phi)$, i = 0,...4. This is a 10 parameter fit and we call this method and the corresponding fit "global".
We also used a different method, inspired from photometric work on barred galaxies. We first obtained a face-on projected density of the model and then made 100 radial cuts with an angle of 36 degrees between two consecutive cuts. For each cut we make a two component fit of the radial density profile using the functional form
$I(R,\phi) = D_0\ R^{-D_1}\ +\ D_2\ exp[-((R - D_3)/D_4)^2]$,
D_0, D_1, D_2, D_3 and D_4 are constants and are determined independently for each radial cut, i.e. for each value of the azimuthal angle. When doing these fits we do not take into account the regions with $R < 1$, since these are too near the center to contain any useful information about the ring. Since this method deals with each radial cut independent of all the others we call it "local".
We thus have for each radial cut a set of D_i values, i = 0,..,4. We now discard those cuts - and the corresponding values of D_i - which are at angles less than 30 degrees from the bar major axis, as well as all other cuts where the ring contribution does not detach itself from the background. To the remaining values of (D_i, ϕ) we then fit the simple forms

$$D_i(\phi) = p_i + q_i cos(2\phi), \qquad i = 0, .., 4 \tag{6.10}$$

where p_i and q_i are constants.
In the above two methods we have parametrised all the density except for the ring by a simple power law. It could be argued that it would have been more realistic had we used an exponential disc plus a functional form to describe the bar. This, however, would have implied a very large number of free parameters and made the problem badly determined. We find that in most cases a gaussian profile gives a very good fit to the ring component, while the power law profile, is adequate for the remaining part. In this way we limit the number of free parameters. In a large number of cases we checked by eye that the results are satisfactory.As a further measure of the quality of the fits we could compare how well the estimates given independently by the two methods agree. In general we find that the radius of the ring is very well determined. This is less so for its width and mass, since they can be considerably influenced by the wings of the gaussian. This is not too serious for narrow rings, but much more so for wide ones.

Chapter 7

Summary

In this chapter I summarize the main results my thesis. I have addressed from the theoretical point of view some aspects of the morphology and dynamics of spiral galaxies.

7.1 Main results

7.1.1 Galaxy models for radiative rransfer

I have addressed the validity and the limitations of the axisymmetric smooth exponential model used for the description of spiral galaxies. I have quantified the error that is introduced in the parameters describing a galaxy when the spiral structure is neglected and I have found that errors are neither systematic nor very large. Therefore I have concluded that an axisymmetric model constitutes a valid description of real spiral galaxies. On the other hand, I have found that if the clumpy distribution of dust is not taken into account, then the amount of dust may be underestimated by at most 40%.

7.1.2 Spectral energy distribution of spiral galaxies

I have constructed a Spectral Energy Distribution (SED) model for spiral galaxies taking into account the relative spatial distributions of the stars and the dust, the locally absorbed ultraviolet (UV) radiation in star forming regions and the transiently heated dust grains. I have applied it to the edge-on spiral galaxies NGC 891, NGC 5907, NGC 4013, UGC 2048 and UGC 1082 using data from the literature. The fitting parameters of the model are the star formation rate (SFR), the dust mass and the proportion of the locally absorbed UV radiation. The SFRs obtained for these galaxies are in excellent agreement with the values of SFR found in the literature. The inferred dust masses, on the other hand, suggest that the dust masses quoted in the literature constitute an underestimation of the actual dust content in these galaxies. I also find that in normal galaxies (contrary to starburst galaxies) a large percentage of the dust heating is due to the old stellar population.

7.1.3 N-Body simulations of barred galaxies

I have investigated the morphology and kinematics of barred galaxies from the theoretical point of view analyzing N-body simulations representing barred galaxies. I have run models with different halo and bulge distributions in order to investigate the effect of the central concentration of the halo and the bulge on the morphological properties of the bar. I have found that a massive halo in the inner parts of the model galaxy results in a more elongated, more peanut-like and more strong bar. Several other morphological and kinematic properties are also investigated and a case for two types of bars is made.

7.2 Future prospects

7.2.1 Suggestions for future studies on SED of galaxies

So far, the limited data at wavelengths longer that 100 microns have allowed the application of SED models to a small sample of normal (non starburst) galaxies. In the past, statistical studies have suffered from over-simplified models leading to contradictory results about the distribution of dust in galaxies. As new data at FIR wavelengths are obtained for more galaxies, it is essential to develop a standard technique for the interpretation of these data. I think that on the basis of my study, a standard technique can be developed and tested on the very well studied cases I have presented. Then this technique can be applied to a much larger sample of observations of galaxies which will become available. Face-on spiral galaxies should be included in this study, as well as ellipticals and even irregulars.

7.2.2 Suggestions for future studies on N-body simulations of barred galaxies

While there have been a lot of studies on the subject of stellar orbits in barred galaxies, all these studies deal with analytical potentials. The analysis of the orbits in "live" potentials (i.e. potentials derived from N-body simulations) will reveal the mechanisms responsible for processes such as the formation of rings, the transfer of angular momentum from the bar to the disk and the halo, and the trapping of stars in resonances. Understanding the mechanisms that drive the evolution of galaxies from the theoretical point of view, is an indispensable step for the interpretation of observations of barred galaxies in the local as well as in the distant universe.